THESIS FOR THE DEGREE OF DOCTOR OF PHILOSOPHY

Optically pumped semiconductor disk lasers for high-power wide wavelength tuning

Carl Borgentun

CHALMERS

Photonics Laboratory
Department of Microtechnology and Nanoscience (MC2)
CHALMERS UNIVERSITY OF TECHNOLOGY
Göteborg, Sweden, 2012

Optically pumped semiconductor disk lasers for high-power wide wavelength tuning

Carl Borgentun

Göteborg, January 2012

Doktorsavhandlingar vid Chalmers tekniska högskola
Ny serie nr 3317
ISSN 0346-718X

Technical Report MC2-208
ISSN 1652-0769

ISBN 978-91-7385-636-2

Photonics Laboratory
Department of Microtechnology and Nanoscience (MC2)
Chalmers University of Technology
SE-412 96 Göteborg, Sweden
Phone: +46 (0)31 7721000

Front cover illustration: Schematic of an OP-SDL cavity with optically pumped gain element, out-coupling mirror, and birefringent filter.

Printed by Chalmers reproservice, Chalmers University of Technology
Göteborg, Sweden, January, 2012

Optically pumped semiconductor disk lasers for high-power wide wavelength tuning

Carl Borgentun

Photonics Laboratory
Department of Microtechnology and Nanoscience (MC2)
Chalmers University of Technology, SE-412 96 Göteborg, Sweden

Abstract

In this work I present and verify a strategy that makes it possible to change the wavelength, or color, of an external cavity semiconductor laser over a very large range. This is achieved by a careful design and thorough optimization of the active component — the gain element of the laser.

This thesis concerns the so-called optically pumped semiconductor disk laser (OP-SDL), which represents a relatively new class of lasers showing great promise for future applications. The advantages include the wavelength versatility that is common for most semiconductor lasers, but also adds the ability to deliver multi-Watt output powers into a nearly diffraction-limited beam, and a free-space external cavity for the easy insertion of various optical elements. These properties have generated great interest in the OP-SDL for use in life science, metrology, entertainment applications, forensics, and many other fields. Recently, efforts have also been made to extend the tuning range for use in spectroscopic applications such as intra-cavity laser absorption spectroscopy.

This thesis focuses on the design of the gain element of an OP-SDL, and how to obtain a wide tuning range while keeping the output power at a high level. The design strategy has been to balance the effects of the spectral dependencies of material gain, subcavity resonance, and spatial overlap of quantum wells with the optical field. Experimental evaluations show that the strategy has been successful and a tuning range of 43 nm, with a maximum output power of 2.6 W was obtained. With improved thermal management the peak output power was increased to more than 7.5 W with a tuning range of 32 nm.

Furthermore, two new measurement techniques were developed. One technique very accurately measures the active mirror reflectance, or the spectral reflectance of an optically pumped gain element, and is particularly useful for evaluating a fabricated gain element. The other technique is for the full characterization of a laser beam, yielding the amplitude and phase distributions, and is well suited for the high-intensity beam from an OP-SDL.

Keywords: Semiconductor laser, optically pumped semiconductor disk laser, vertical-external-cavity surface-emitting laser, design, high power, wavelength tuning, beam characterization, gain measurements

List of papers

This thesis is based on the following appended papers:

[I] **C. Borgentun**, J. Bengtsson, and A. Larsson, "Direct measurement of the spectral reflectance of OP-SDL gain elements under optical pumping," *Optics Express*, vol. 19, no. 18, pp. 16890–16897, August 2011.

[II] **C. Borgentun**, J. Bengtsson, A. Larsson, F. Demaria, A. Hein, and P. Unger, "Optimization of a broadband gain element for a widely tunable high-power semiconductor disk laser," *IEEE Photonics Technology Letters*, vol. 22, no. 13, pp. 978–980, July 2010.

[III] **C. Borgentun**, C. Hessenius, J. Bengtsson, M. Fallahi, and A. Larsson, "Widely-tunable high-power semiconductor disk laser with non-resonant AR-assisted gain element on diamond heat spreader," *IEEE Photonics Journal*, vol. 3, no. 5, pp. 946–953, 2011.

[IV] **C. Borgentun**, J. Bengtsson, and A. Larsson,"Full characterization of a high-power semiconductor disk laser beam with simultaneous capture of optimally sized focus and farfield," *Applied Optics*, vol. 50, no. 12, pp. 1640–1649, 2011.

Acknowledgement

Thank you all. Especially to those of you who have in some way or other assisted me in the work behind this thesis. I will try to mention some of you here even though I am fully aware of that the list will not be complete.

First and foremost, I am immensely indebted to my principal advisor Jörgen "Jürgli" Bengtsson who has constantly guided me through the realms of research with pedagogical prods, and to Prof. Anders Larsson for wise advice and for granting me permission to start this journey in the first place.

I could not have reached this far without the help of some giants: Frank Demaria, Peter Unger, and colleagues at Ulm Universität; Chris Hessenius and Mahmoud Fallahi at the University of Arizona; and Oliver Sieber, Valentin Wittwer, Ursula Keller, and friends at ETH Zürich.

For making the Photonics laboratory such a terrific place both during and after working hours, I must thank Göran "The Adolf" Adolfsson, Petter "Svarten" Westbergh, Martin "Rambo" Stattin, Carl "Lunkan" Lundström, Benjamin "Kaiser" Kögel, Erik "Lasso" Haglund, and the rest of the photonic bunch. Yuxin "You-spin" Song deserves special thanks for being a super officemate and for his unworldly patience with my CW drumming and pomming. David "Ace" Engström is also very special, and should at the very least be acknowledged for luring me into the photonics business in the first place. I can not forget Joakim "Deckar'n" Nyman and Anders "Gröter" Ström that made the first years of Chalmers so enjoyable. To be mentioned in a paltry acknowledgment may not seem much, but be sure that your names are forever written across my heart.

Thank you Hannah, for being always wonderful. Thank you Jesus, for being always there.

This work was financially supported by the Vetenskapsrådet, and hence, by a lot of Swedes. I would also like to acknowledge IQE Europe Ltd. in Cardiff, UK for supplying the epitaxial material.

Carl Borgentun

Göteborg
January 2012

List of acronyms

AR	Antireflectance
AMR	Active mirror reflectance
BPP	Beam parameter product
BRF	Birefringent filter
BS	Beam-splitter
CCD	Charged-coupled device
CVD	Chemical vapor deposition
CW	Continuous wave
DBR	Distributed Bragg reflector
FSR	Free spectral range
GE	Gain element
GS	Gerchberg-Saxton (algorithm)
HS	Heat spreader
ICLAS	Intra-cavity laser absorption spectroscopy
MBE	Molecular beam epitaxy
MOCVD	Metal-organic chemical vapor deposition
MOVPE	Metal-organic vapor phase epitaxy
OC	Out-coupling mirror
OP-SDL	Optically pumped semiconductor disk laser
QD	Quantum dot
QW	Quantum well
RPG	Resonant periodic gain
SESAM	Semiconductor saturable absorber mirror
TEC	Thermoelectric cooler
TMM	Transfer matrix method
VCSEL	Vertical-cavity surface-emitting laser
VECSEL	Vertical-external-cavity surface-emitting laser

Table of contents

1
Introduction

"The laser is a solution looking for a problem."

— Irnee D'Haenens, pioneer laser scientist

On May 16th 1960, the race to build the first laser was won. Theodore Maiman and his assistant Irnee D'Haenens demonstrated stimulated emission — the light-generating mechanism in the laser — for the first time by firing light from a flashlamp into a ruby crystal [1]. Within six months, the experiment had not only been reproduced and thus verified, but the laser had been realized in no fewer than five different material systems [2–6]. At this early stage little attention was paid to applications of the fascinating new light source, hence the part-joke, part-challenge statement at the top of this page. The first widely-recognized, commercial application took until the mid 1970s to reach the public: the barcode scanner. Since then, the laser has indeed become an essential

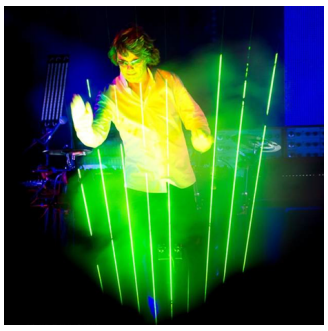

(a) Jean Michel Jarre (here playing on his laser harp) used OP-SDLs to celebrate the royal wedding in Monaco, July 2011. Image credit: Rod Maurice.

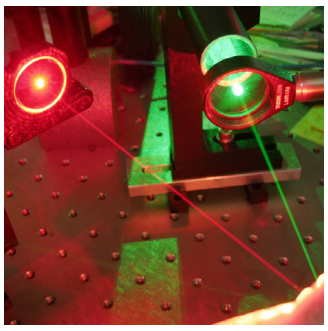

(b) A red OP-SDL pumped by a green pump laser. Image credit: Thomas Schwarzbäck[a].

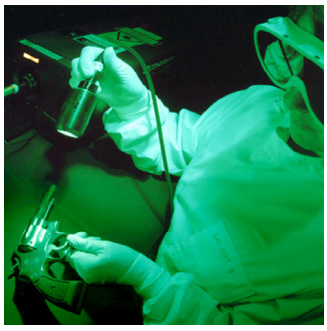

(c) In forensics, OP-SDLs can help in the detection of fingerprints, invisible with other methods. Image credit: Department of Justice, Northern Ireland.

Figure 1.1: Some application examples of the OP-SDL.

[a]Institut für Halbleiteroptik und Funktionelle Grenzflächen and Research Center SCoPE, University of Stuttgart

technology in modern society. The applications are almost too numerous to name, ranging from medicine to metrology, from displays to data storage, and of course short and long distance communication [7–13]. Even out-of-this-world applications — such as interplanetary communication or pushing up cargo in a space elevator — have been proposed and to some extent realized [14, 15]. As diverse as these applications might seem, they all make use of the unique property of laser light: its highly ordered lightwave with a very well-defined color. Thus, by now it would seem that the solution has found its fair share of problems.

In 1962, just two years after the laser first appeared, a laser based on semiconductor technology was demonstrated [16]. Today the semiconductor laser is by far the most common laser type. Most modern semiconductor lasers are either edge-emitting lasers (EELs) or vertical-cavity surface-emitting lasers (VCSELs). The EELs can emit beams of high output power but the beams are highly elliptical and require sophisticated external optics for satisfactory use in many applications [17]. A beam from a VCSEL, on the other hand, can be close to diffraction-limited, which enables easy and efficient coupling into optical fibers, but the single-mode VCSELs are limited to output powers in the milliwatt range. This thesis deals with a particular type of VCSEL — the optically pumped semiconductor disk laser (OP-SDL), or the vertical-external-cavity surface-emitting laser (VECSEL) as it is also referred to. It can combine the high output power of the edge-emitting device with the superior beam quality of the VCSEL [18–22]. Another advantage of the OP-SDL is its free-space cavity, which allows for the insertion of various optical elements, such as nonlinear crystals for frequency doubling [23], semiconductor saturable absorber mirrors (SESAMs) for mode-locking [24] or wavelength-selective elements for wavelength tuning [25], i.e. for a precise change of the wavelength, or color, of the light from the laser.

So far, the OP-SDL has found its way into a diverse set of application areas such as medicine, forensics, research, and entertainment (including the potential killer application: the *pico projector*[a]) [27–30], some of which are illustrated in figure 1.1. Although widely tunable OP-SDLs have been shown to be highly useful in applications such as intra-cavity laser absorption spectroscopy (ICLAS) [31, 32], research in extending the tuning range has not been given major attention until recently. Pioneering efforts were made by Garnache *et al.*, who applied a design principle balancing the wavelength dependent effects of subcavity resonance and material gain maximum [33]. A recently developed OP-SDL used a set of quantum wells (QWs) with different gain characteristics, resulting in a very wide tuning range but low output power [34]. There has also been research on employing a multi-chip setup, which has produced record-high output powers, though the tuning range in those experiments was less impressive [35].

[a]Forecasts predict the market for light-weight portable projectors to reach 140 million units by 2018 [26].

The work underlying this thesis has investigated whether the tuning range of an OP-SDL could be extended by a clever design of the gain element (GE), a vital component in the OP-SDL cavity. Besides a wide tuning range, the output power should be high throughout a major part of the tuning range. The balancing principle of Garnache *et al.* was used but the design was extended to include a much longer subcavity with 12 identical QWs. The long subcavity allows for most of the pump light to be absorbed and the large number of QWs enables a higher net optical gain. Also, part of the structure was parametrically optimized to even more accurately control the broadband properties. To experimentally investigate the effectiveness of these measures, a new measurement method for quantifying the active mirror reflectance (AMR) of the gain element was developed and realized. It was also investigated whether the gain element could be used for mode-locking to generate short pulses by including a SESAM in the OP-SDL cavity.

This thesis opens with a brief introduction to the theory of lasers in chapter 2. The remainder roughly follows the time line of the research efforts it describes: Chapter 3 explains the strategies used in the design of a broadband OP-SDL gain element, followed by the fabrication of such a gain element, described in chapter 4. Chapter 5 presents the performance of the gain element in an OP-SDL setup, including results from measurements of the AMR, and chapter 6 describes a new measurement technique to fully characterize a laser beam. Finally, chapter 7 explains pulse generation using the gain element and a SESAM for mode-locking, and shows results from such experiments.

2

Elements of laser theory

In this chapter I will briefly explain some concepts that are important for understanding the laser described in this thesis. Generally, a laser consists of two parts: an amplifying medium and a cavity. Section 2.1 describes how a medium can be amplifying through photon interaction with matter, followed by some fundamentals of laser cavities in section 2.2. Finally, I will focus on different methods of tuning OP-SDLs in section 2.3.

2.1 Light amplification

Amplification of light involves photon-induced transitions between energy levels in the amplifying medium. In theory only two energy levels are required: an upper and a lower laser energy level. A system, such as an atom or a molecule, is somehow excited from the lower to the upper level and can then return to the lower level while emitting a photon. The efficiency can however be radically increased by the use of one or two additional energy levels: an upper and/or a lower pump energy level, see figure 2.1. This facilitates the creation of *population inversion*, which is necessary for lasing and means that the population of the upper laser level is larger than that of the lower laser level. The transition from the upper pump level to the upper laser level as well as the transition from the lower laser level to the lower pump level should therefore have a short lifetime so that the upper laser level always is as filled as possible and the lower laser level always is as empty as possible.

In a semiconductor the distinct energy levels of the atoms are split into energy bands. The lower energy band is called the *valence band* and the higher the *conduction band*. When an electron is excited to the conduction band, a vacancy in the valence band is created. This vacancy is called a *hole* and can be seen as another species of charge carrier, just like the electrons but with different diffusion velocity, (sign of) charge, and mass.

The excited system in most semiconductor lasers is a region where there is a non-equilibrium excess of electrons and holes. There are mainly two methods to create such a non-equilibrium: by electrical or optical pumping. When

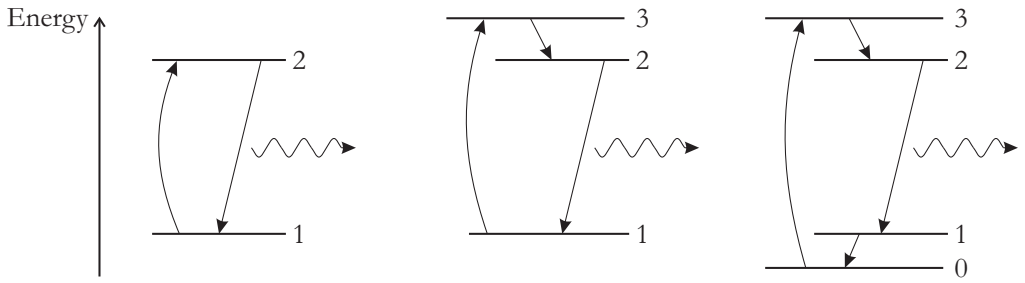

Figure 2.1: The energy levels of generic two-, three-, and four-level laser systems. The upper laser level is by convention denoted 2, and the lower laser level 1. The upper pumping level is denoted 3 and the lower pumping level 0, if they differ from the laser levels. The transitions between levels 3-2 and 1-0 are generally non-radiative, i.e. no photon is emitted in the process.

electrical pumping is used, a current is injected into the p-n junction region of the semiconductor laser creating a population of electrons in the conduction band and a population of holes in the valence band. In an optically pumped laser the non-equilibrium is created through *absorption* of incident light from a pump source, which is often another laser.

With a certain probability, an incident photon will trigger the excited system to relax to the lower laser level, releasing another photon at the same time. This process is called *stimulated emission* and the essential point is that *the emitted photon is an exact copy of the incident photon regarding phase, polarization, wavelength, and propagation direction.* Alternatively, it is possible for the excited system to relax without the help of an incident photon, but the emission is in that case *spontaneous*, i.e. the phase, polarization, and propagation direction are random. The wavelength of the emitted photon is governed mainly by the energy difference by the excited state and the lower state, which means that the wavelength of spontaneous and stimulated emission can be equal. In fact, the seed that initiates the stimulated emission in a laser is a spontaneously emitted photon, which, by chance, has a combination of wavelength, polarization, and propagation direction that is supported by the laser cavity, see section 2.2.

Most semiconductor lasers include a thin layer sandwiched between materials with a higher bandgap energy. When the width of the sandwiched layer is decreased to a few nanometers, quantum effects become important and the energy levels in it become discrete. The sandwiched layer is called a *quantum well* (QW) and the surrounding material is called barriers, see figure 2.2. By adjusting the width and the depth of the QW, the energy levels can be engineered so that photons of a precisely specified and almost arbitrary wavelength are emitted. The OP-SDLs described in this thesis use materials from the GaAs system with InGaAs QWs.

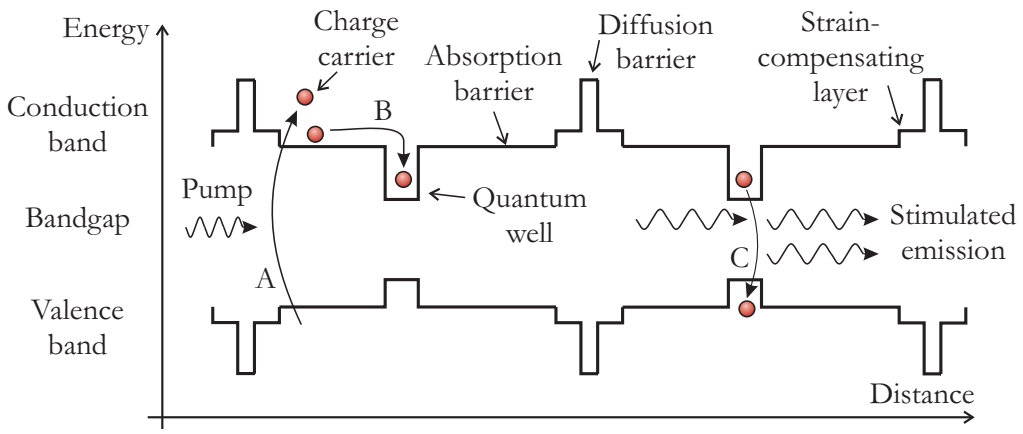

Figure 2.2: Schematic showing examples of the constituting epitaxial layers of a generic active region in an optically pumped semiconductor laser. Also shown are important charge carrier processes: excitation by pump light absorption (A), diffusion (B), and relaxation by stimulated emission (C).

2.2 Cavity

A *cavity*, or resonator, usually consists of two or more mirrors of some sort. The OP-SDL cavity often uses multilayer mirrors, so called distributed Bragg reflectors (DBRs), such as the dielectric out-coupling mirror and the semiconductor DBR in the gain element. A cavity mirror can also be a single reflective surface, as for instance in an edge-emitting laser, where the mirrors are simply the facets of the cleaved semiconductor chip; the difference in refractive index of air and semiconductor is so large that a considerable part ($\sim 32\%$) of the power of the incident field is reflected. The standard free-space cavity laser uses a linear cavity with two mirrors opposite each other, as for most of the OP-SDLs considered in this work, see figure 2.3. Other types of OP-SDL cavities can be folded one, two, or even more times, and light can be coupled out through one or many of the mirrors.

In a free-space cavity, where there is no waveguiding effect, the geometrical shapes of the cavity mirrors are important for the optical stability of the cavity. Consider, for example, a linear cavity with two planar mirrors. Since the laser field makes so many round-trips in the cavity, even the slightest misalignment of one of the mirrors, will eventually cause the field to escape the cavity by simply walking off the mirrors. The cavity is then said to be *unstable*. *Stable* cavities need at least one concave mirror, and often spherical mirrors are used. The external cavity of a linear OP-SDL is a plano-spherical cavity with one planar mirror, which is the gain element itself, and one spherical concave dielectric mirror, which also serves as the out-coupling element. As long as the length of this cavity is shorter than the radius of curvature of the spherical mirror, the cavity is stable [36], see figure 2.4.

The cavity determines many of the properties of the emitted laser light. This is because the optical field in the cavity needs to fulfil certain criteria: during

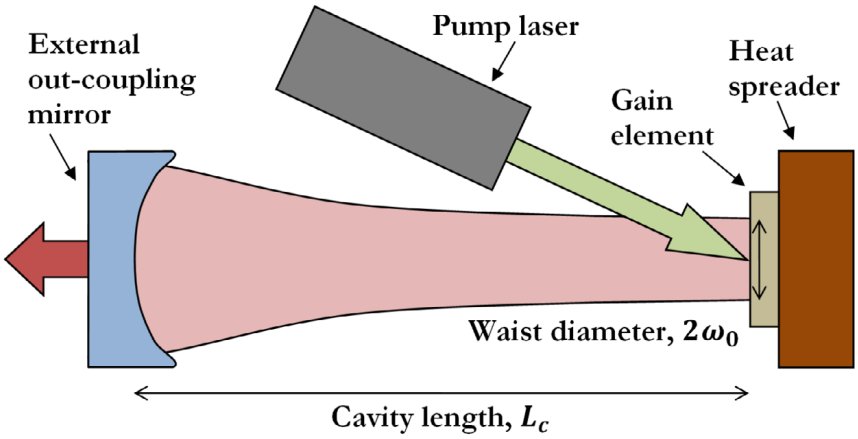

Figure 2.3: A simple, linear cavity showing the vital components of an OP-SDL. The gain element and the external out-coupling mirror constitute the cavity end mirrors, and the pump laser injects energy into the QWs in the gain element.

a round-trip in the cavity the field has to repeat itself with respect to its phase and amplitude. The amplitude (or intensity) condition is often referred to as the *lasing condition* and implies that during one round-trip in the cavity the gain should precisely compensate for the losses from the cavity. The lasing condition for a standard, CW-operating OP-SDL with one out-coupling mirror with reflectance R_{OC}, a gain element with a reflectance $R_{GE} > 1$, distributed scattering losses α_s, and cavity length L_c is written in equation 2.1.

$$1 = \exp\left(-\alpha_s \, 2 \, L_c\right) \, R_{OC} \, R_{GE} \tag{2.1}$$

The *phase condition* simply states that the phase of the optical field after one round-trip should be the same, ensuring that the field is not interfering destructively with itself. This means that the accumulated phase change of one round-trip, $\Delta\phi$, must be an integer multiple of 2π, see equation 2.2, where $k_0 = \frac{2\pi}{\lambda_0}$ is the vacuum wavenumber, λ_0 is the vacuum wavelength, and n is the refractive index of the material filling the cavity. In words, the cavity supports only those wavelengths for which the cavity length is an integer number of half wavelengths in the material. These wavelengths are called the *longitudinal modes* of the cavity and are separated in frequency by the free spectral range (FSR), $\nu_F = \frac{c_0}{2\,n\,L_c}$. Depending on the properties of the gain medium and of the cavity, a laser can lase in one single mode or in many longitudinal modes simultaneously. The mode(s) that will lase is/are determined by the gain spectrum and the possible modes permitted by the cavity. As a final remark on longitudinal modes, equation 2.2 is strictly valid only for plane waves. For the Gaussian beam in an OP-SDL some expressions are slightly modified, but

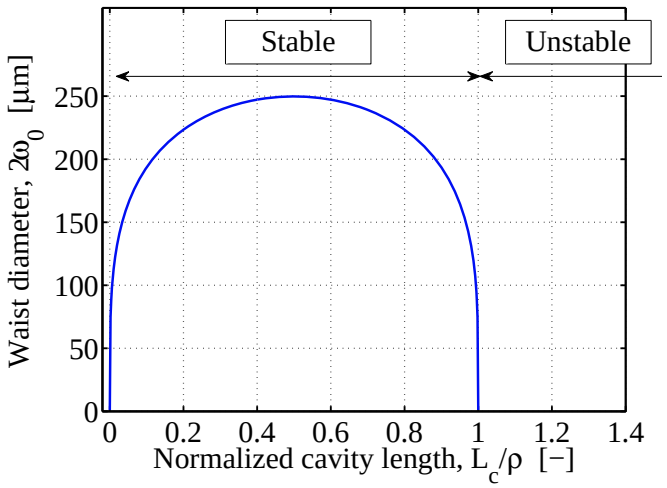

Figure 2.4: Plot of equation 2.3 illustrating the stable and unstable regions of a linear OP-SDL cavity, such as the one depicted in figure 2.3. Here, the free-space wavelength is $\lambda_0 = 980$ nm and the radius of curvature of the external out-coupling mirror is $\varrho = 100$ mm.

the longitudinal mode separation ν_F is the same as for a plane-wave cavity.

$$\begin{aligned} \Delta\phi = k_0\, n\, 2L_c = q\, 2\pi \quad \text{where } q \in \mathbb{N} \\ \Rightarrow \; L_c = q\frac{\lambda_0}{2\, n} \end{aligned} \tag{2.2}$$

A laser cavity also supports modes with different transverse field distributions. The simplest one is called the *fundamental mode*, which often is the only desired one. Which of these *transverse modes* of an OP-SDL that will actually lase is to a great extent controlled by the overlap of the cavity field at the gain element with the pump spot, i.e. the area on the gain element illuminated by the pump laser. Therefore it is customary to match the sizes of the pump spot and the fundamental mode on the gain element, which will then likely result in a highly single-mode optical field in the fundamental mode. If the pump spot size is decreased so that it becomes significantly smaller than the fundamental mode size, the cavity no longer supports lasing. If, on the other hand, the pump spot size is increased, higher order transverse modes with larger mode sizes will compete for the existing gain and often win over the fundamental mode. This results in an output beam of lower quality but often of higher output power. The diameter, $2\omega_0$, of the fundamental mode at the gain element in a linear OP-SDL is controlled by the length of the external cavity, see figure 2.4 and equation 2.3, where ϱ is the radius of curvature of the spherical external mirror.

$$2\omega_0 = 2\sqrt{\frac{\lambda_0\, L_c}{\pi} \cdot \sqrt{\frac{\varrho}{L_c} - 1}} \tag{2.3}$$

2.3 Tuning of OP-SDLs

The ability to adjust the lasing wavelength, i.e. to *tune* the wavelength, is important in many applications [37, 38]. It is evident from equation 2.2 that a change in L_c, n, or q will also change the lasing wavelength, λ_0. For example, the length of the cavity can be changed by adjusting the position of a cavity mirror [39, 40] or by including a gradient in the waveguide [41]. The refractive index of the waveguide can be changed electrically [42]. Longitudinal mode selection can be realized through an external dispersive element such as a grating [43] or an intra-cavity etalon [44]. Since the bandgap energy and the refractive index are temperature dependent, fine-tuning of the lasing wavelength can be achieved by deliberately adjusting the temperature [45, 46]. In this work I have used another principle of tuning, a *birefringent filter* (BRF), see figure 2.5, to select a certain wavelength by increasing the losses for other wavelengths.

2.3.1 Tuning with a birefringent filter

A BRF is simply a thin plate of a birefringent material, e.g. crystalline quartz. In birefringent media the refractive index is anisotropic such that it depends on the direction of the optical field vector, i.e. the field polarization. The refractive index differs ever so slightly along two perpendicular axes in the crystal: the ordinary and the extraordinary. Any incident optical field will be decomposed into two fields, each with the polarization along its respective axis, which implies that each field propagates as if the medium was isotropic. Due to the refractive index difference, a phase retardation is introduced between the two fields [47, 48]. This causes a change in polarization of the total field when the two components are recombined after the propagation, at the exit surface of the BRF, but for some certain wavelengths the retardation is a multiple of π and the polarization is unaltered. If the BRF is sufficiently thin, there is only one wavelength for which this is fulfilled within the wavelength range with positive gain in the gain element, see figure 2.6. The refractive index for the extraordinary field depends on the angle between the polarization plane of the incident field and the crystal optical axis. Thus, the wavelength for which the polarization is unaltered can be tuned by rotating the BRF.

The plot in the figure assumes that the BRF is inserted at the Brewster angle, and that the incident field is obeying the polarization condition for zero reflection (the Brewster effect). For all other polarizations there will be reflection losses. Thus, if inserted at the Brewster angle, the BRF linearly polarizes the optical field in the plane of incidence of the BRF. Further, the wavelength fulfilling the condition for preserved polarization upon propagation through the BRF, as indicated in the figure, will be favored, since this field will obey the Brewster condition for zero reflection also when exiting the BRF, and thus ideally experience zero total reflection loss.

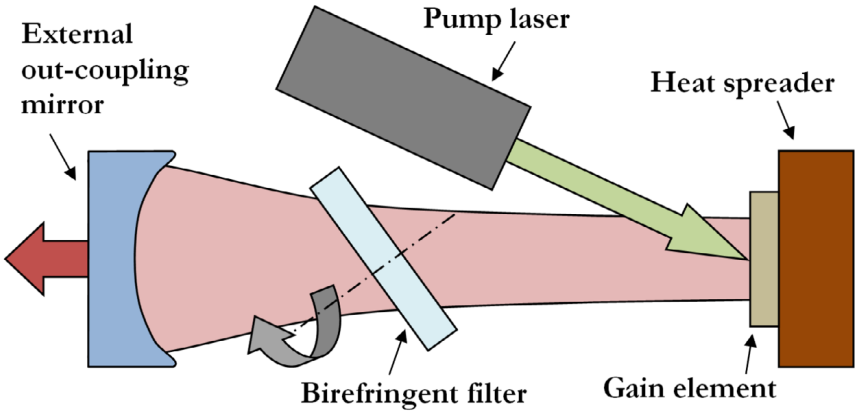

Figure 2.5: Schematic view of an OP-SDL with a wavelength-selective element (i.e. the rotatable birefringent filter) inserted in the external cavity.

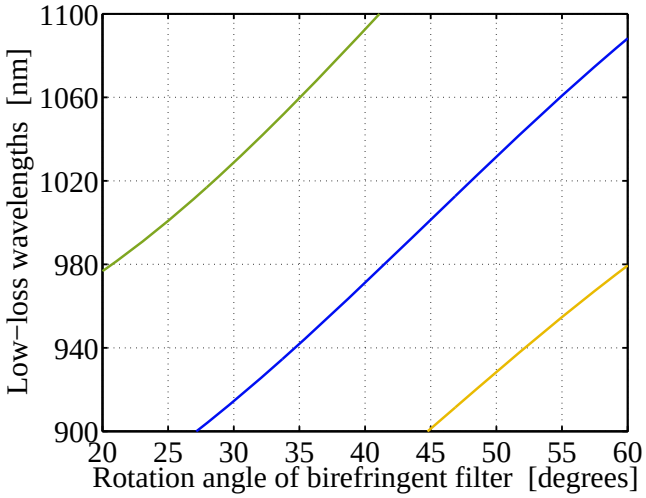

Figure 2.6: Tuning with a BRF. For each rotation angle, the wavelengths are plotted, for which the polarization after propagation through a 1 mm thick BRF is unaltered, which is the condition for negligible reflection loss at the Brewster angle.

3
Design of gain element

This chapter describes how the layer structure of a gain element (GE) can be designed to obtain certain optical properties. In section 3.1 I introduce the concept of *active mirror reflectance* (AMR) and describe the numerical models I implemented to simulate the AMR. In this work, the AMR as a function of optical wavelength is of particular importance, this I will often refer to as the spectral reflectance. In section 3.2 I show the optimization process of the gain element design, and section 3.3 explains how I simulated the lasing threshold to investigate the broadband properties of the gain element.

3.1 Active mirror reflectance

The layer structure of a gain element conventionally consists of two main parts: an active region and a DBR, see figure 3.1. The active region mainly contains layers that absorb the field of the pump laser, but also thin layers working as QWs, which can provide optical gain through stimulated emission. The DBR is one of the two cavity end mirrors — the other being the external out-coupling mirror — and is composed of $\lambda/4$-thick layers of materials with alternating high and low refractive indices. The field will partly reflect at every layer interface, and due to multiple constructive interference almost all of the energy can be reflected, provided that the wavelength of the field is close to the design wavelength of the DBR. Thus, as a component in the external cavity the optically pumped gain element is equivalent to a mirror with gain, the reflectance of which is denoted the active mirror reflectance (AMR) [49].

Naturally, for a widely tunable OP-SDL, the AMR of the gain element needs to exceed 100% in a wide wavelength interval. If the output power should vary only slowly in this interval as the wavelength is tuned at a constant pump intensity, it is further reasonable to assume that the AMR spectrum of the gain element should be flat and smooth without significant peaks or dips.

To enable the design of a gain element so that its AMR spectrum can be prescribed, I implemented a model for the optical gain of the QWs, which is presented in section 3.1.1. To simulate the propagation of the optical field

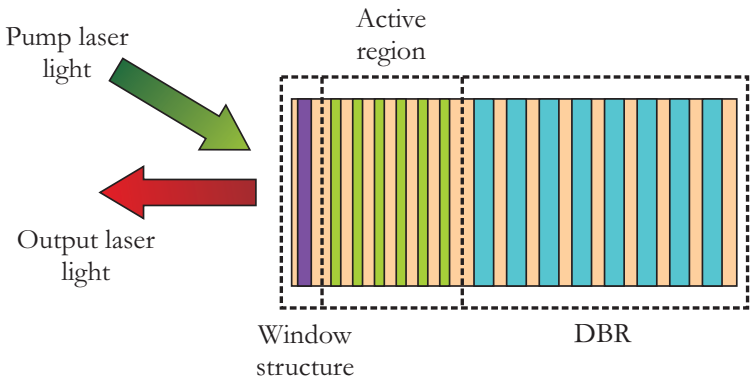

Figure 3.1: Schematic showing the many layers of a generic gain element and its two main parts: the active region and the DBR. The window structure consists of one or two layers and prevents oxidation and leakage of charge-carriers.

within the gain element I used a *transfer matrix method* (TMM) described in section 3.1.2.

3.1.1 Gain model

Optical gain, which we denote by g, is often described by the relative increase, or decay, per unit length of the intensity of a plane wave propagating in a medium. In modeling of optical fields it is customary to instead use an imaginary part, n'', of the refractive index to account for optical gain. Using $n = n' + i\,n''$ for the refractive index, the intensity of a propagating plane wave can thus be written in two ways:

$$\begin{cases} I \propto \exp\left(g\,d\right) \\ I \propto \left|\exp\left(i\,k_0\,n\,d\right)\right|^2 = \left|\exp\left(i\,\frac{2\pi}{\lambda_0}\,\left(n' + i\,n''\right)\,d\right)\right|^2 = \exp\left(-\frac{4\pi}{\lambda_0}\,n''\,d\right) \end{cases} \tag{3.1}$$

where $k_0 = \frac{2\pi}{\lambda_0}$ is the vacuum wavenumber and d is the propagated distance. Thus, by identification, $n'' = -\frac{\lambda_0}{4\pi}\,g$, so that a negative imaginary part of the refractive index signifies positive gain, i.e. amplification or an increase in amplitude. Gain can also be negative, which means an absorption of the field, or a decrease in amplitude, and this is signified by a positive imaginary part of the refractive index.

To calculate the amount of gain from the stimulated emission of a QW, I developed an algorithm, numerically realized in `MATLAB`, in which a value for g is obtained. This value would later be converted into n'' in the optical model, see section 3.1.2.

Even for high gain values, the real part of the refractive index is much larger than the magnitude of the imaginary part of the refractive index, and is supposed not to be significantly affected by the changes in gain. The real part of the refractive index has been modeled using the model by Afromowitz

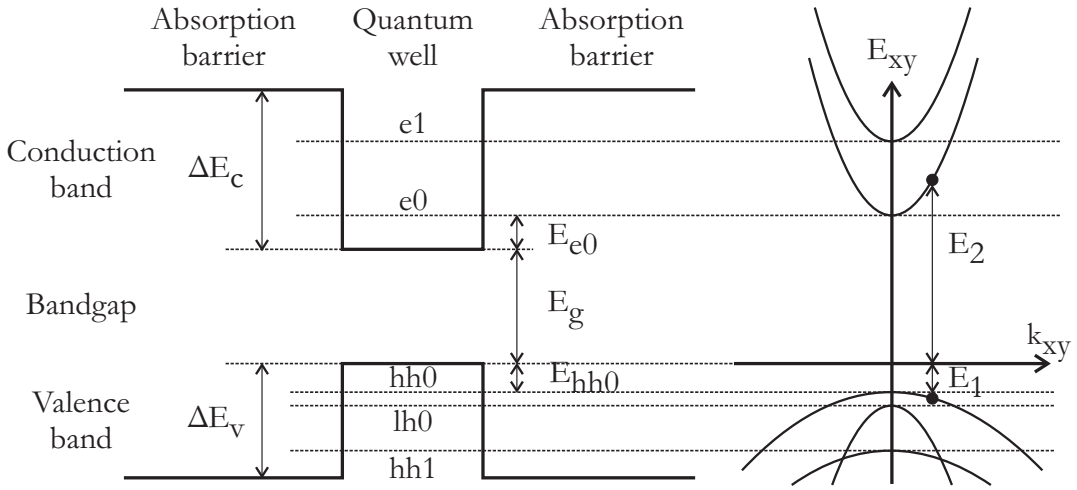

Figure 3.2: Left: Energy diagram of a typical quantum well and its surrounding barriers. The QW energy levels in the conduction band that are accounted for in the gain model are denoted by e_0 and e_1. The valence band energy levels are hh_0 and hh_1 for the heavy holes and lh_0 for the light holes. Right: The energies of electrons and holes in the plane of the QW have an approximately parabolic dependence on the momentum.

[50] for Al(x)Ga(1-x)As and GaAs(x)P(1-x), and the model by Adachi [51] for In(x)Ga(1-x)As.

First, we want to calculate the bandgap energy, E_g, (see figure 3.2) in the QW. We need this to determine the energy levels in the conduction and valence energy bands. The energy of the bandgap of a ternary material, such as In(x)Ga(1-x)As, is modeled by a first or second degree polynomial with the composition parameter, x, as the variable. The polynomial is fitted to experimental values, especially to those of the binary extremes, in this example InAs and GaAs. The fitted polynomial coefficients can be found in table 3.1 along with other material parameters used in this section.

However, the crystalline patterns of the atoms, i.e. the *lattices*, in the GaAs absorption barriers and the InGaAs QWs do not match exactly, since the volume of the unit cell of InGaAs is slightly larger than that of the GaAs unit cell. The atoms of the QW still adapt to the crystal lattice of the barriers but the InGaAs atoms are compressed in the plane of the substrate, a condition known as *strain*. Strain is not always compressive but can also be tensile, if the atoms of the thinner layer are more closely spaced, i.e. has a smaller lattice constant, than the surrounding layers. The strain is accumulated for every strained atomic layer and a strain energy is built up. When the strain energy reaches a critical value, the lattice bonds can no longer keep the lattice together and the lattice relaxes to its natural lattice constant by introducing defects in the lattice, see figure 3.3. The defects reduce performance for most optical devices since they provide the charge carriers with an additional way to recombine nonradiatively, but as long as the critical thickness is not reached, the defect density can be kept low. Under such circumstances strain can even

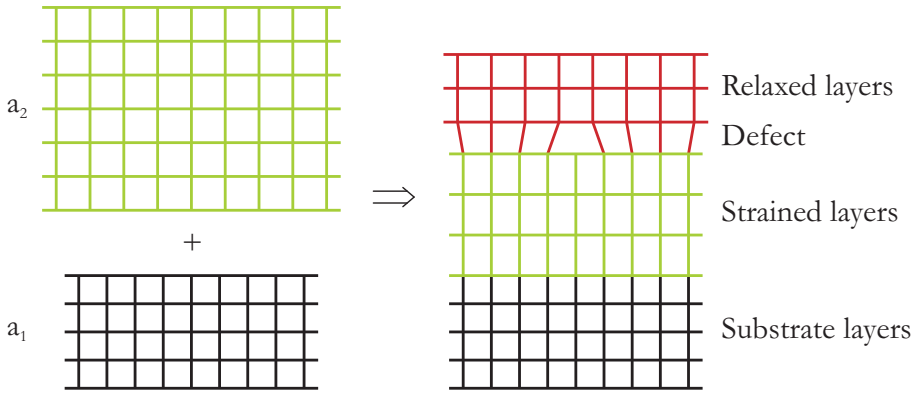

Figure 3.3: A generic crystal lattice illustrating strain; each grid node represents an atom and each grid line an atomic bond. On a substrate with lattice constant a_1, layers with a larger lattice constant, a_2, are placed and thus become strained. The strained layers are compressed in two dimensions (of which only one is shown in this two-dimensional representation) and elongated in the third. A defect is introduced when the accumulated strain reaches the critical value.

be beneficial for the performance of some lasers, since the strain changes the in-plane effective masses of the valence band and hence, the curvature of the valence band. This can make the curvatures of the conduction and valence bands more equal, which lowers the charge carrier density needed to achieve lasing threshold [52, 53].

The accumulation of strain energy can be partly compensated for by introducing layers with opposite strain. In this work we used ∼30 nm thick tensilely strained GaAs(x)P(1-x) layers with about 7% P to compensate for the 6 nm thick compressively strained In(20%)Ga(80%)As QWs.

Strain also changes the bandgap energy, E_g, and thus we have to take this into account in our calculations. This is done as indicated in equation 3.2, which can be found in Coldren [54], as is also the case for all other equations in this chapter unless otherwise stated. The meaning of the variable names, and typical values for our materials, can be found in table 3.1.

$$\begin{aligned} E_g &= E_g^{strained} = \\ &= E_g^{unstrained} + \left(\frac{2}{3} \cdot \frac{\mathrm{d}E_g}{\mathrm{d}P} \left(C_{11} + 2\,C_{12}\right) \left(1 - \frac{C_{12}}{C_{11}}\right) + Sb \left(1 + 2\,\frac{C_{12}}{C_{11}}\right) \right) \cdot \varepsilon \end{aligned} \tag{3.2}$$

Further, to calculate the barrier height for the electrons and holes, respectively, a model for how the total difference in bandgap between the QW and the barrier is distributed on the conduction and valence bands is needed. We assumed that the fraction of the difference in bandgap energy between the QWs and the barriers that is in the conduction band is $\Delta E_c = 0.7$ and in the valence band, consequently, $\Delta E_v = 0.3$ [55].

The next step is to determine the energies of the electrons and the holes. Since a QW is very thin in the longitudinal z-dimension, the motion perpendicular to the QW plane is constrained and the corresponding energy levels are discrete and quantized with quantum number n. They are denoted E_{en} for electrons and E_{hn} for holes, and are computed by numerically solving equations 3.3, in which the energy levels are relative to the respective band edge, see figure 3.2. Selection rules dictate which transitions are possible; in general only transitions between energy levels with the same quantum number n are allowed.

$$0 = \tan\left(\sqrt{\frac{m_{e,h}^{zIn} L_z^2}{2\hbar^2} E_{en,hn}}\right) - \sqrt{\frac{m_{e,h}^{zAl}}{m_{e,h}^{zIn}} \cdot \frac{\Delta E_{c,v} - E_{en,hn}}{E_{en,hn}}} \quad \text{for even } n \tag{3.3a}$$

$$0 = \cot\left(\sqrt{\frac{m_{e,h}^{zIn} L_z^2}{2\hbar^2} E_{en,hn}}\right) + \sqrt{\frac{m_{e,h}^{zAl}}{m_{e,h}^{zIn}} \cdot \frac{\Delta E_{c,v} - E_{en,hn}}{E_{en,hn}}} \quad \text{for odd } n \tag{3.3b}$$

In the transverse dimensions, the QW is infinitely extended and the electrons and holes can move freely. The energies corresponding to this motion are in addition to the quantized energy levels in the longitudinal direction, and can be described by the equations for bulk material, equation 3.4. Here, $E_{1,2}$ are the energies of state 1 in the valence band and state 2 in the conduction band, respectively, relative to the top of the valence band. They are here given as a function of E_{21}, the transition energy between the two states. $E_{v,c}$ are the energies relative to the top of the valence band of the perpendicular energy level in the valence and conduction band, respectively, and m_r^{xy} is the reduced effective mass in the plane of the QW.

$$E_1 = E_v - (E_{21} - (E_c - E_v)) \cdot \frac{m_r^{xy}}{m_h^{xy}} \tag{3.4a}$$

$$E_2 = E_c + (E_{21} - (E_c - E_v)) \cdot \frac{m_r^{xy}}{m_e^{xy}} \tag{3.4b}$$

$$m_r^{xy} = \frac{m_e^{xy}\, m_h^{xy}}{m_e^{xy} + m_h^{xy}}$$

In this model, conservation of momentum and energy is assumed as well as the concept of effective mass. Further, a parabolic dependence of the in-plane energy on the momentum is assumed. For more intricate and microscopic models, often based on the $k \cdot p$ theory, see for instance Hader *et al.* [56] or Bückers *et al.* [57].

There are in fact two types of holes: light and heavy. They have different masses, hence their names, and thus have different energy levels in the valence band. This lifting of the valence band degeneracy is not always included in gain calculations, but it was so in this work. Some of the following and previous equations therefore have to be calculated separately for the heavy and the light holes, and the contributions to the gain are finally summed in equation 3.12.

The probability of an optical transition between two energy levels is proportional to the *transition matrix element*, M_T, see equation 3.5 [58]. M_T is different for heavy and light holes because the perpendicular energy levels, E_{hn}, and the in-plane energies, E_1, are different.

$$M_T^2 = 1.33\, m_0\, E_g\, \frac{3}{4} \cdot \left(1 + \frac{E_g + E_{en} + E_{hn}}{E_g + E_1 + E_2}\right) \tag{3.5}$$

The *density of states* is a function describing how the availability of electron or hole states varies with transition energy. The *reduced density of states*, ρ, is a function that combines the separate density of states functions of the electrons and the holes into a function describing the availability of electron-hole pairs. The expression can be found in equation 3.6, which gives different results for heavy and light holes because of different reduced effective masses and valence band energy levels. The function H is the *heaviside* function, which is a step function with a value of zero for negative arguments and of one for positive.

$$\rho = \frac{m_r^{xy}}{\pi\hbar^2 L_z} \sum_n H\big[E_{21} - (E_g + E_{en} + E_{hn})\big] \tag{3.6}$$

The energy level where an electron state is equally probable to be filled as to be empty is called the *Fermi energy level*. When the material is not in thermal equilibrium, which occurs as soon as there are excess charge carriers, the Fermi energy level is split into two separate so called *quasi-Fermi energy levels*: one for the conduction band, E_{fc}, and one for the valence band, E_{fv}. It is thus assumed that there is a local thermal equilibrium in each band. The quasi-Fermi energy levels can be determined by numerically solving equations 3.7, where N_{QW} is the excess charge-carrier density (per volume) in the QW and L_z the QW thickness.

$$N_{QW} = \frac{k_B\, T}{\pi\, \hbar^2\, L_z}\, m_e \cdot \sum_n \ln\left(1 + \exp\left(\frac{E_{fc} - E_{en}}{k_B\, T}\right)\right) \tag{3.7a}$$

$$\begin{aligned} N_{QW} = {} & \frac{k_B\, T}{\pi\, \hbar^2\, L_z}\, m_{hh} \cdot \sum_n \ln\left(1 + \exp\left(\frac{E_{fv} - E_{hhn}}{k_B\, T}\right)\right) + \\ & + \frac{k_B\, T}{\pi\, \hbar^2\, L_z}\, m_{lh} \cdot \sum_n \ln\left(1 + \exp\left(\frac{E_{fv} - E_{lhn}}{k_B\, T}\right)\right) \end{aligned} \tag{3.7b}$$

The probability that a state is occupied by an electron is described by the *Fermi factors*, f_1 and f_2 for the valence and conduction band, respectively, see equations 3.8. Equation 3.8a has to be used for heavy and light holes separately,

since the in-plane energies, E_1, are different, as seen in equation 3.4.

$$f_1\left[E_1\right] = \frac{1}{1+\exp\left(\dfrac{E_1 - E_{fv}}{k_B T}\right)} \tag{3.8a}$$

$$f_2\left[E_2\right] = \frac{1}{1+\exp\left(\dfrac{E_2 - E_{fc}}{k_B T}\right)} \tag{3.8b}$$

We are now ready to write an expression for the gain of the transition between state 2 in the conduction band and state 1 in the valence band.

$$g_{21} = \frac{\pi\, q^2\, \hbar}{\varepsilon_0\, c\, m_0^2\, n} \cdot M_T^2\, \rho \cdot \frac{f_2 - f_1}{E_{21}} \tag{3.9}$$

However, we are still not finished. Due to energy uncertainty of short-lived states, gain for a certain transition energy receives contributions from electron-hole pairs with slightly different transition energies in a process called *lineshape broadening*. Often this lineshape is modeled with a Lorentzian lineshape function, as in equation 3.10, and the broadening as a convolution with the unbroadened gain spectrum, as stated in equation 3.11.

$$LS\left[E - E_{21}\right] = \frac{\hbar/\left(\pi\tau\right)}{\left(\hbar/\tau\right)^2 + \left(E - E_{21}\right)^2} \tag{3.10}$$

$$g^{LS}\left[E\right] = g_{21} \otimes LS = \int g_{21}\left[E_{21}\right] \cdot LS\left[E - E_{21}\right]\, \mathrm{d}E_{21} \tag{3.11}$$

The total gain is now found by summing the contributions from the heavy and the light holes.

$$g_{tot} = g_{heavy}^{LS} + g_{light}^{LS} \tag{3.12}$$

There are some refinements to this model that can have significant effects. For instance, when many charge-carriers are located close together, like in a densely populated QW, the *Coulomb interaction* between them will start to screen out the atomic potential of the lattice. This process is not fully understood but has been shown to shrink the bandgap and therefore it is sometimes referred to as *bandgap shrinkage* or *bandgap renormalization*. The magnitude of the shrinkage depends on the population in the QW and to a first approximation the effect on the gain spectrum is a rigid shift in wavelength of the entire spectrum. The population-dependent wavelength shift is approximated by equation 3.13.

$$\Delta\lambda = \frac{C_{shrink}}{h\, c}\, N_{QW}^{1/3}\, \lambda^2 \tag{3.13}$$

If instead the QW population density is very low, *excitonic effects* can be observed. An exciton is an electron and a hole that are loosely bound and

orbit around each other, in some similarity with the electron and nucleus of the simple hydrogen atom [59]. The transition energy of an exciton, $E_{exc,h}$, is slightly less than the energy separation of two quantized energy levels, see equation 3.14, where E_b is the exciton binding energy. The exciton absorption spectrum, $\alpha_h\,[E_{21}]$, can be mathematically described by equation 3.15, where N_{sat} is the saturation carrier concentration, $dE_{exc,h}$ is the width of the excitonic absorption line, and $\alpha_{0,h}$ is the unsaturated absorption strength [60].

$$E_{exc,h} = E_g + E_e + E_h - E_b \tag{3.14}$$

$$\alpha_h\,[E_{21}] = \frac{\alpha_{0,h}}{1 + N/N_{sat}} \cdot \exp\left(-\frac{1}{2}\left(\frac{E_{21} - E_{exc,h}}{dE_{exc,h}}\right)^2\right) \tag{3.15}$$

The gain spectra for some various excess charge-carrier population densities are shown in figure 3.4; the excitonic absorption is evident in the low population case. To show the obvious redshift at higher carrier concentrations due to bandgap shrinkage, figure 3.5 compares the gain spectra close to the gain peak with and without inclusion of Coulomb interaction.

3.1.2 Optical model

Having determined the real and imaginary parts of the refractive index of each layer we are ready to simulate the propagation of an incident optical field in the gain element. A right-propagating plane wave has an optical field given by equation 3.16, where A_{right} is the complex field in the starting plane, and B_{right} is the complex field after propagating a distance d in a homogeneous medium with refractive index n, see also figure 3.6(a).

$$B_{right} = A_{right} \cdot \exp\left(i\,k_0\,d\,n\right) \tag{3.16}$$

At the interface between two media of different refractive indices, the field will be partly reflected and partly transmitted. The fields propagating towards right and left in the layer structure will couple to each other through the reflections at the interfaces, according to equation 3.17, see also figure 3.6(b).

$$\begin{cases} A_{left} = T_{BA} \cdot B_{left} + R_{AB} \cdot A_{right} \\ B_{right} = T_{AB} \cdot A_{right} + R_{BA} \cdot B_{left} \end{cases} \tag{3.17}$$

The magnitudes of reflection and transmission are described by the Fresnel equations 3.18, assuming that absorption only takes place in the media and not at the interfaces.

$$R_{AB} = \frac{n_A - n_B}{n_A + n_B}, \text{ valid for reflection in medium A against medium B} \tag{3.18a}$$

$$T_{AB} = \frac{2\,n_A}{n_A + n_B}, \text{ valid for transmission from medium A to medium B} \tag{3.18b}$$

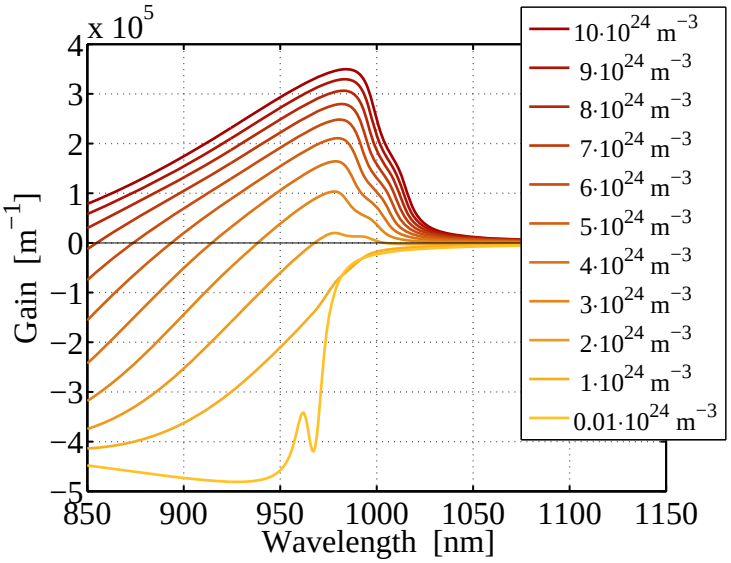

Figure 3.4: Gain spectra for a 6 nm In(20%)Ga(80%)As QW for different excess charge-carrier population densities. The excitonic absorption at the lowest population density is clearly visible as a narrow dip in the curve.

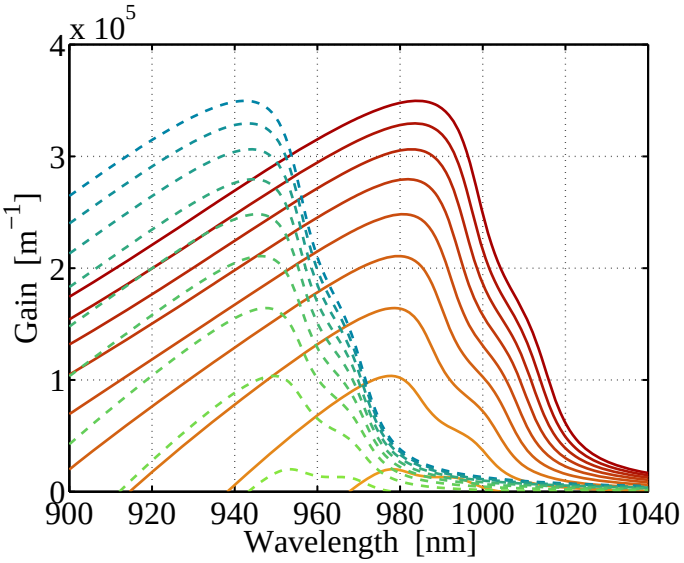

Figure 3.5: A close-up of the peak of the gain spectra in figure 3.4 to show the effect of Coulomb interaction. Solid lines and dashed lines are calculated with and without including Coulomb interaction, respectively.

Table 3.1: Material parameters used in the gain calculations.

Quantity	Expression	Ref
Unstrained lattice constant for In(x)Ga(1-x)As, [m]	$a_0^{In} = (5.6533 + 0.405\,x) \cdot 10^{10}$	[61]
Unstrained lattice constant for Al(y)Ga(1-y)As, [m]	$a_0^{Al} = (5.6533 + 0.0078\,y) \cdot 10^{10}$	[61, 62]
Lattice mismatch parameter, [-]	$\varepsilon = \frac{a_0^{In} - a_0^{Al}}{a_0^{In}}$	[54]
Unstrained bandgap in In(x)Ga(1-x)As, [J]	$E_g^{In} = (1.424 - 1.615x + 0.555\,x^2) \cdot q$	[63]
Unstrained bandgap in Al(y)Ga(1-y)As, [J]	$E_g^{Al} = (1.424 + 1.247\,y) \cdot q$	[62]
Shear deformation potential for In(x)Ga(1-x)As, [J]	$Sb = (-1.7 - 0.1\,x) \cdot q$	[54]
Pressure dependence of the band gap for In(x)Ga(1-x)As, [J m^2/N]	$\frac{\mathrm{d}E_g}{\mathrm{d}P} = (1.17 - 0.13\,x) \cdot q \cdot 10^{-10}$	[54]
Elastic stiffness coefficient for In(x)Ga(1-x)As, [N/m^2]	$C_{11} = (11.88 - 3.551\,x) \cdot 10^{10}$	[54, 61, 62]
Elastic stiffness coefficient for In(x)Ga(1-x)As, [N/m^2]	$C_{12} = (5.38 - 0.854\,x) \cdot 10^{10}$	[54, 61, 62]
Electron effective mass in the z-dim for In(x)Ga(1-x)As, [kg]	$m_e^{zIn} = (0.0665 - 0.0435\,x) \cdot m_0$	[54]
Heavy hole effective mass in the z-dim for In(x)Ga(1-x)As, [kg]	$m_{hh}^{zIn} = (0.34 + 0.06\,x) \cdot m_0$	[54]
Light hole effective mass in the z-dim for In(x)Ga(1-x)As, [kg]	$m_{lh}^{zIn} = (0.094 - 0.067\,x) \cdot m_0$	[54]
Electron effective mass in the z-dim for Al(y)Ga(1-y)As, [kg]	$m_e^{zAl} = (0.0665 + 0.0835\,y) \cdot m_0$	[62]
Heavy hole effective mass in the z-dim for Al(y)Ga(1-y)As, [kg]	$m_{hh}^{zAl} = (0.34 + 0.42\,y) \cdot m_0$	[54, 62]
Light hole effective mass in the z-dim for Al(y)Ga(1-y)As, [kg]	$m_{lh}^{zAl} = (0.094 + 0.043\,y) \cdot m_0$	[62]
Electron effective mass in the xy-plane for In(x)Ga(1-x)As, [kg]	$m_e^{xy} = 0.071\,m_0$	[64]
Luttinger band parameters for GaAs, [-]	$g_1^{Ga} = 6.98$, $g_2^{Ga} = 2.06$	[61]
Luttinger band parameters for InAs, [-]	$g_1^{In} = 20.0$, $g_2^{In} = 8.5$	[61]
Luttinger band parameters for In(x)Ga(1-x)As, [-]	$g_{1,2} = (1-x)\,g_{1,2}^{Ga} + x\,g_{1,2}^{In}$	-
Heavy hole effective mass in the xy-plane for In(x)Ga(1-x)As, [kg]	$m_{hh}^{xy} = \frac{1}{g_1+g_2}\,m_0$	[65]
Light hole effective mass in the xy-plane for In(x)Ga(1-x)As, [kg]	$m_{lh}^{xy} = \frac{1}{g_1-g_2}\,m_0$	[65]
Exciton binding energy, [meV]	10	[66]
Exciton absorption width, [meV]	4	[67]
Unsaturated exciton absorption strength, [m^{-1}]	$1.3 \cdot 10^6$	[68]
Intra-band scattering time, [s]	$\tau = 100 \cdot 10^{-15}$	[54]
Shrinkage constant, (L_z is the QW thickness), [J m]	$C_{shrink} = 32 \cdot 10^{-3} \cdot q \cdot \left(\frac{10^{16}}{L_z}\right)^{-1/3}$	[54]

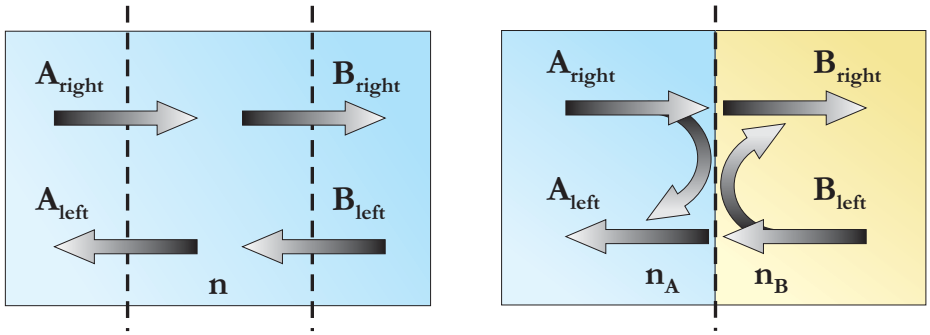

(a) Propagation of an optical field in a homogeneous medium.

(b) Reflection and transmission of an optical field at the interface between two media with different refractive indices.

Figure 3.6: Illustration of the two fundamental processes occurring for the propagation of an optical field through a multilayered structure.

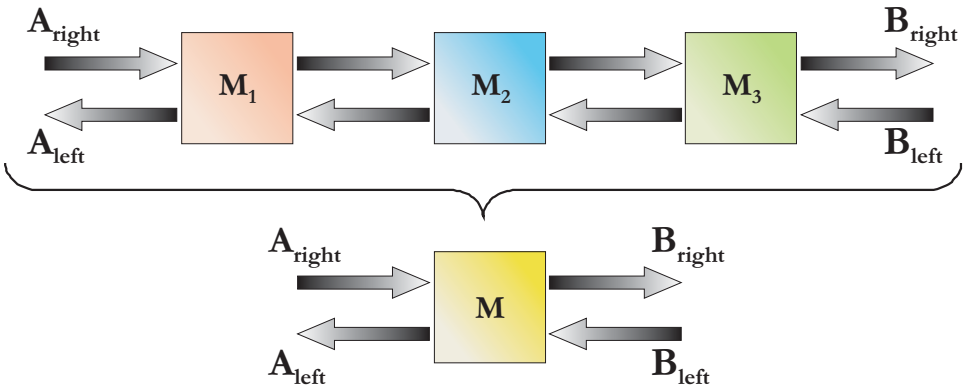

Figure 3.7: The transfer matrix method: given a one-dimensional optical system, the effect of each constituting element on an optical field can be described by an elementary 2×2 transfer matrix, and the entire system can be described by a single transfer matrix, which is the matrix product of all transfer matrices.

Because of the coupling between the right and left propagating fields, it is convenient to describe the propagation with matrices. The field amplitudes of the right and left propagating fields are then put in column vectors. For propagation in a homogeneous medium they are related by the matrix shown in equation 3.19. To describe the reflection and transmission at an interface the matrix in equation 3.20 is used.

$$\begin{bmatrix} A_{right} \\ A_{left} \end{bmatrix} = \begin{bmatrix} \exp\left(-i\,k_0\,d\,n\right) & 0 \\ 0 & \exp\left(+i\,k_0\,d\,n\right) \end{bmatrix} \begin{bmatrix} B_{right} \\ B_{left} \end{bmatrix} \tag{3.19}$$

$$\begin{bmatrix} A_{right} \\ A_{left} \end{bmatrix} = \frac{1}{2\,n_A} \begin{bmatrix} n_A + n_B & n_A - n_B \\ n_A - n_B & n_A + n_B \end{bmatrix} \begin{bmatrix} B_{right} \\ B_{left} \end{bmatrix} \tag{3.20}$$

The two types of matrices shown in equations 3.19 and 3.20 are called elementary *transfer matrices* and we find that the total transfer matrix for an optical system is simply the matrix product of the respective elementary transfer matrices of the separate parts of the system. This is called the transfer matrix method, see figure 3.7 and equation 3.21 for the system depicted in the figure.

$$\begin{bmatrix} A_{right} \\ A_{left} \end{bmatrix} = M_1 M_2 M_3 \begin{bmatrix} B_{right} \\ B_{left} \end{bmatrix} = M \begin{bmatrix} B_{right} \\ B_{left} \end{bmatrix} = \begin{bmatrix} M_{11} & M_{12} \\ M_{21} & M_{22} \end{bmatrix} \begin{bmatrix} B_{right} \\ B_{left} \end{bmatrix} \tag{3.21}$$

We are interested in the reflectance of the structure, the AMR, which is the square of the ratio between the reflected and the incident fields:

$$AMR = \left| \frac{A_{left}}{A_{right}} \right|^2 \tag{3.22}$$

An essential assumption is that no light is incident from the backside of the gain element, i.e. $B_{left} = 0$. Using this assumption together with equations 3.21 and 3.22 we find an expression for the AMR for a general multilayer system described by its total transfer matrix M as shown in equation 3.23. Since the wavenumber, k_0, and the refractive indices are wavelength dependent, the AMR has to be calculated for each wavelength separately.

$$\begin{cases} A_{right} &= M_{11} B_{right} + M_{12} B_{left} \\ A_{left} &= M_{21} B_{right} + M_{22} B_{left} \end{cases} \Rightarrow B_{right} = \frac{A_{right}}{M_{11}} = \frac{A_{left}}{M_{21}} \Leftrightarrow$$

$$\Leftrightarrow AMR = \left| \frac{A_{left}}{A_{right}} \right|^2 = \left| \frac{M_{21}}{M_{11}} \right|^2 \tag{3.23}$$

We are also interested in the field variations within the gain element, since we want to position our QWs at positions of high field intensity for the center wavelength. Due to the high refractive index step at the interface to air, the gain element will form a distinct subcavity between that interface and the DBR, and the field will form standing waves with nodes and antinodes. The subcavity

will be resonant for certain wavelengths leading to an increase in field intensity, which we will use to balance the effects of material gain and the walk-off of the antinodes from the QW positions.

Thus, we have found a way to calculate the active mirror reflectance for a certain wavelength by calculating the optical gain and including it in the imaginary part of the refractive index, and using the TMM to simulate the field propagation in the layer structure. Now it is time to put our model to use!

3.2 Optimization

I wanted to optimize the structure of the gain element parameters so that the AMR spectrum of the gain element made the best fit to a target reflectance spectrum, shown in figure 3.8. This target was a top-hat function with a lower level of 100%, which is the approximate reflectance of the DBR stopband, and an upper level of 103%, which is the reflectance required to overcome the estimated cavity losses. The width of the upper level was set to ±20 nm from the center design wavelength, i.e. between 960 and 1000 nm.

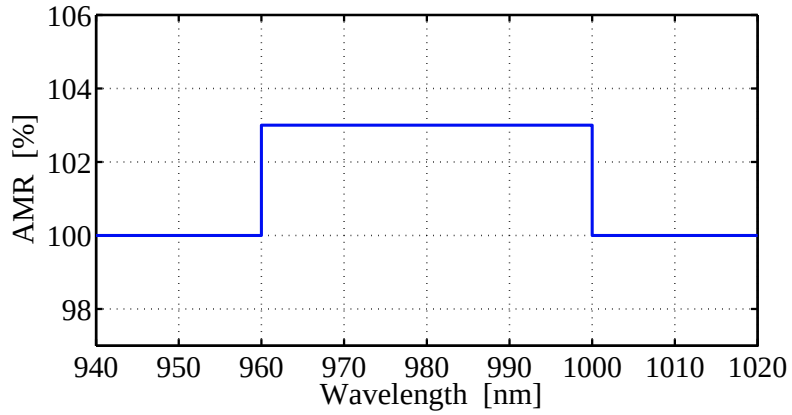

Figure 3.8: Target unsaturated reflectance spectrum for the optimization process. The lower level of the target reflectance is the approximate reflectance of the DBR stopband, and the upper level is the AMR required to overcome the estimated cavity losses.

In the following calculations, a constant incident pump intensity of $8.1 \cdot 10^7$ W/cm^2 was assumed. Since the optical model in the previous section is one-dimensional, the pump light was modeled to be incident perpendicular to the GE surface. The wavelength of the pump light was 808 nm, for which the absorption coefficient of GaAs is about $1.3 \cdot 10^6$ m^{-1} [70].

The conventional design strategy for an OP-SDL gain element not intended for tuning is to position the QWs at consecutive antinodes of the standing wave of the optical field at the design wavelength. The thickness of the window layer or the top pump-absorbing barrier is then adjusted so that the structure is

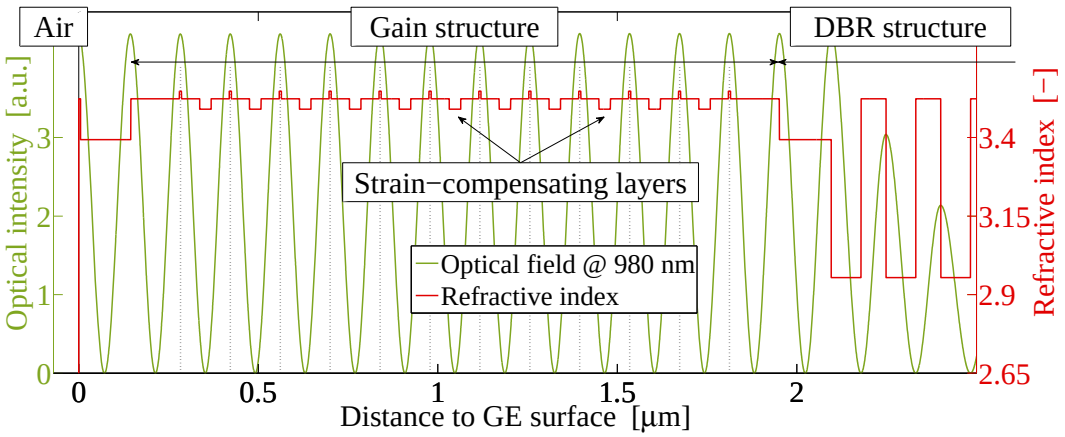

Figure 3.9: The calculated intensity of the optical field inside the subcavity for a conventional RPG design. Also shown is the refractive index profile. The QWs are marked with vertical dotted black lines.

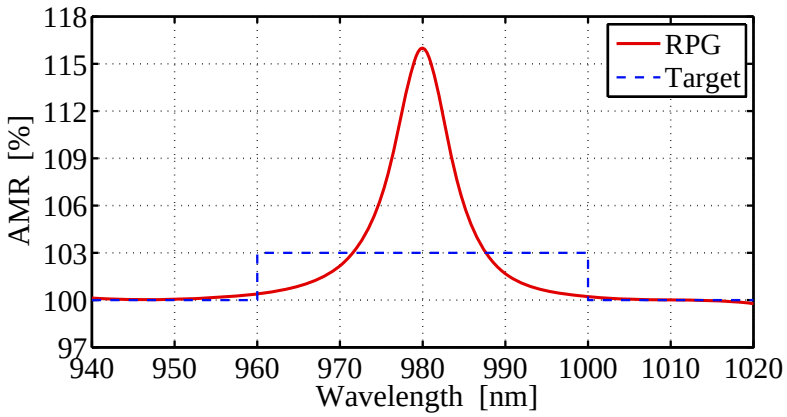

Figure 3.10: Simulated unsaturated reflectance spectrum for a conventional RPG design. Also shown is the target reflectance spectrum, as shown in figure 3.8.

resonant for the design wavelength, i.e. so that the field has an antinode at the interface to air; this also ensures that the amplitude of the standing wave is maximized. This conventional design is commonly known as a *resonant periodic gain* (RPG) design. The subcavity field at the center design wavelength and the AMR for such a design are presented in figures 3.9 and 3.10, respectively. Note that the positions of the QWs and the antinodes are aligned and that there is a field antinode at the interface to air. The AMR spectrum shows a distinct peak at the design wavelength which is expected as everything in the design of the gain element is adjusted to favor this particular wavelength.

However, this peaked spectrum is far from our top-hat shaped target reflectance spectrum so we have to do something to produce a better target fit. For instance, we could make the structure antiresonant at the center wavelength, i.e. adjusting the total structure thickness so that a field node is at the

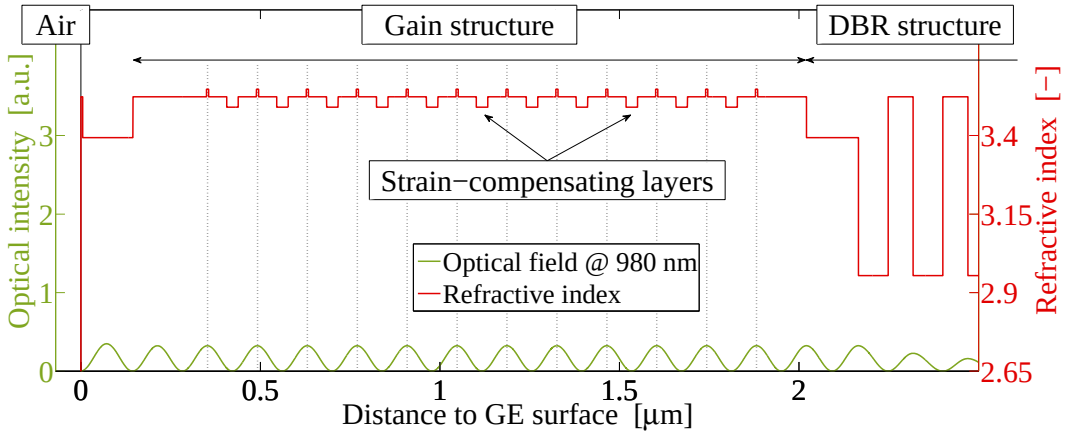

Figure 3.11: The calculated intensity of the optical field inside the subcavity for an antiresonant design. Also shown is the refractive index profile. The QWs are marked with vertical dotted black lines. Note the much lower field intensity for this structure than for the conventional, RPG design.

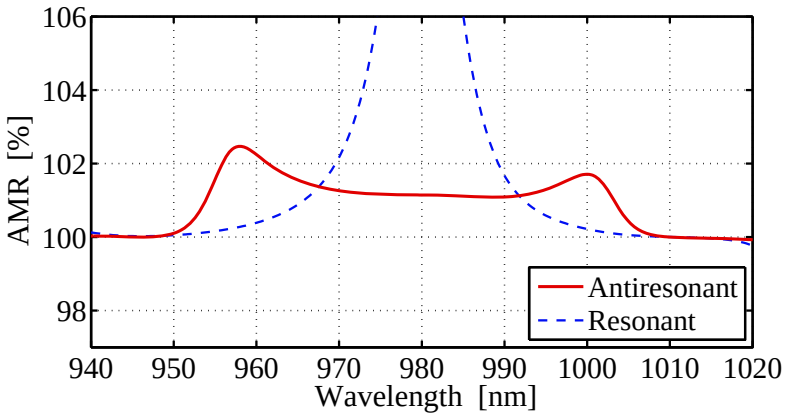

Figure 3.12: Simulated unsaturated reflectance spectrum for an antiresonant design. Also shown is the simulated reflectance spectrum for the conventional RPG design, as shown in figure 3.10.

air interface. This is easily done by increasing for example the top barrier layer thickness by $\lambda/4 \approx 69.5$ nm for GaAs at $\lambda = 980$ nm. The resulting subcavity field and AMR spectrum for this design are presented in figures 3.11 and 3.12, respectively. Note that the positions of the QWs and the antinodes still overlap but that there now is a field node at the air interface and that the standing wave now has a lower amplitude. There is no longer a single large peak in the reflectance spectrum but two small peaks at ∼960 and 1000 nm.

As can be seen from figure 3.12, the achieved AMR in the 960–1000 nm region is fairly low and does not reach the target value. One reason for the low reflectance is the large thickness of the subcavity. The pump light is absorbed exponentially which makes the carrier densities in the bottom QWs so low that they are close to transparency. For short wavelengths the gain is even negative,

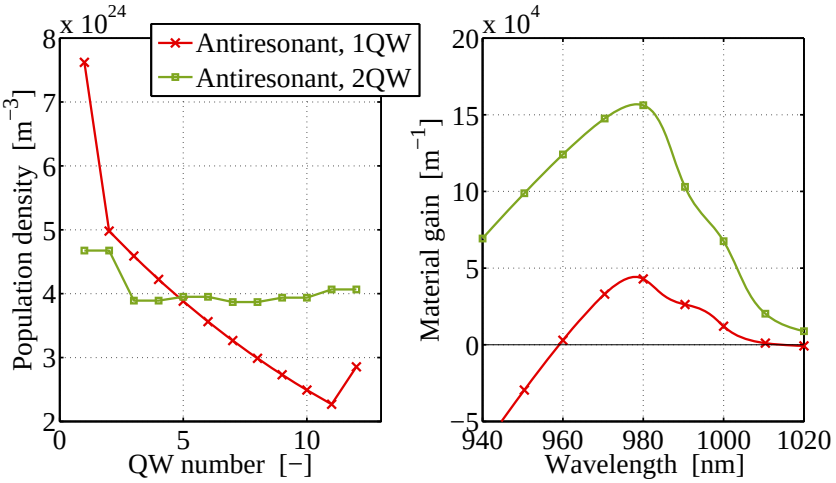

Figure 3.13: Illustration of the effect of the diffusion barriers. Left: The population densities in the QWs in the antiresonant 1QW design are drastically different, while the QWs in the antiresonant 2QW design are almost equally populated. Right: Gain spectrum for the QW with the lowest population density in both designs.

i.e. these QWs absorb light instead of amplify it, see figure 3.13. To counter this the QWs can be positioned in pairs at each antinode making the required subcavity length shorter for the same number of QWs. Further, the populations of the QWs can be equalized by introducing high-bandgap diffusion barriers [71]. These hinder diffusion of charge carriers so that separate absorption volumes can be constructed, within which all absorbed charge carriers will eventually populate the only QW pair in that volume. The thickness of the absorption volumes increases with distance to the GE surface to compensate for the exponential decay of pump light intensity, so that all QWs are roughly equally populated.

Postulating that the number of QWs should be 12 (dictated partly by material growth issues) and, as mentioned, that the QWs should be positioned in pairs at the field antinodes at the center design wavelength, that they should be equally populated, and that the structure should be antiresonant at the center wavelength, then the parameters of the layer structure are in fact to a large extent already given. The subcavity field and the reflectance for this design are presented in figures 3.14 and 3.15, respectively. As in the previous example of a likewise antiresonant subcavity, the positions of the QWs are aligned with the antinodes and there is a field node at the air interface, but the QWs are now positioned in pairs and there are low-index diffusion barriers to ensure equalized QW populations. Note how the absorption volumes grow larger towards the bottom of the structure in order to excite an equal amount of charge carriers in all volumes. However, the reflectance is still quite low. This can be remedied by means of an antireflectance (AR) structure that is included at the top of the structure, see figure 3.16.

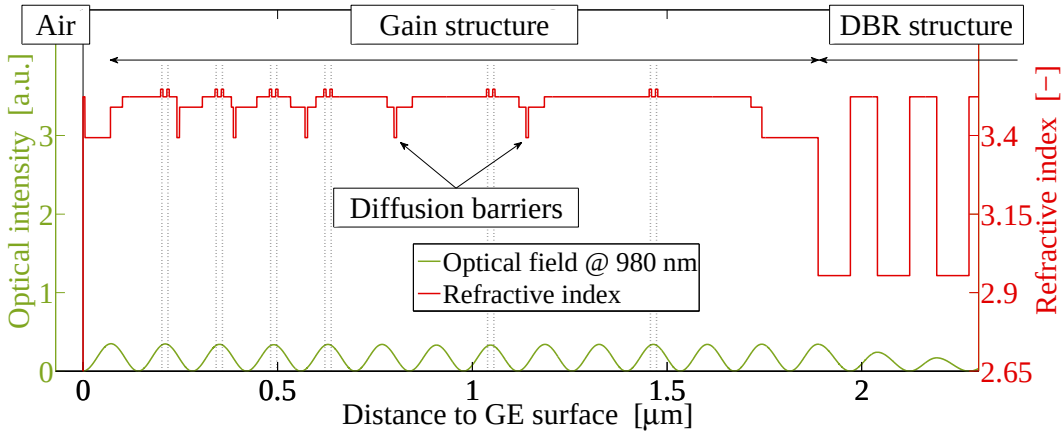

Figure 3.14: The calculated intensity of the optical field inside the subcavity for an antiresonant 2QW design. Also shown is the refractive index profile. The QWs are marked with vertical dotted black lines.

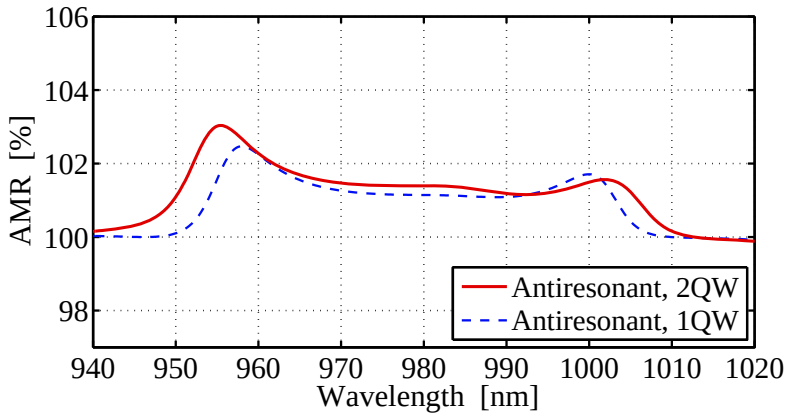

Figure 3.15: Simulated unsaturated reflectance spectrum for an antiresonant 2QW design. Also shown is the simulated reflectance spectrum for the antiresonant 1QW design, taken from figure 3.12.

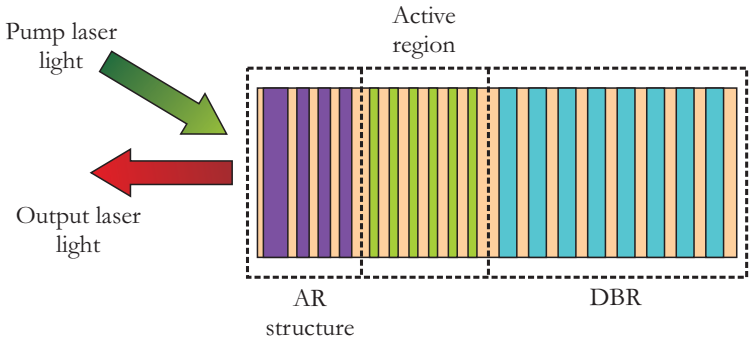

Figure 3.16: Schematic showing the many layers of a gain element extended with an AR structure at the top.

An AR structure is similar to a DBR in that it is a stack of $\lambda/4$ thick layers with alternating high and low refractive indices. The difference is that the AR structure also includes a $\lambda/2$ thick layer, which makes the partially reflected fields interfere destructively lowering the total reflectance. The AR structure has three free parameters: the number of layer pairs, the difference in refractive index, and the center wavelength.

The number of layer pairs in the AR structure controls both the width and the height of the reflectance spectrum, but as is evident from figure 3.17 they can not be controlled separately. Either the width is large but the height low or the height is large and the width is small. The optimum should be somewhere in between.

The difference in refractive index is in this case controlled by the aluminum content of the high-index layers, since these are Al(x)Ga(1-x)As layers and the low-index layers are pure AlAs layers. Therefore, a decrease in aluminum content leads to an increase in refractive index difference which leads to a more pronounced effect of the AR structure. This is illustrated in figure 3.18.

The center wavelength of the AR structure controls the thicknesses of the layers, since they should be exactly $\lambda/4$ thick for this wavelength. The center wavelength adjusts the spectral position of the reflectance minimum of the AR structure and is important for the symmetry of the reflectance spectrum, which is shown in figure 3.19.

As a first step in the optimization of the AR structure parameters I investigated the three effects of the parameters as described above. I constrained the parameter space to the following limits:

Number of layer pairs was between 0 and 4.5, i.e. up to nine layers were considered.

Aluminum content was varied between 0% and 80%.

Center wavelength was varied between 960 and 1000 nm.

For each combination of parameters a multitude of reflectance spectra were simulated with different total structure thicknesses — realized by varying the thickness of a spacing layer between the AR structure and the active region — to find the correct thickness that provided antiresonance for 980 nm, the center design wavelength. The reflectance spectra for different combinations of the three AR parameters were compared using a combination of two quality measures: the width of the wavelength range for which the reflectance was larger than the high target level, i.e. 103%, and the variance of the reflectance in that wavelength range. The wavelength range should be as large as possible to maximize the tunability and the variance as low as possible to ensure low power variations during tuning. I considered the width of the wavelength range to be more important than a very low variance, since variations in output power are unavoidable and the tuning range is more important for many potential applications. During the entire optimization I made sure that the QWs were

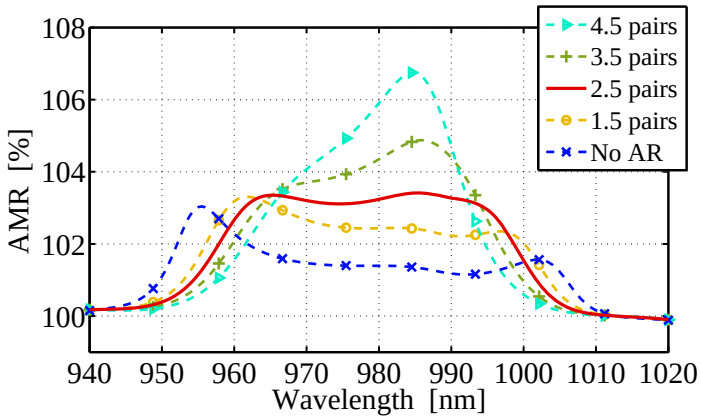

Figure 3.17: Simulated reflectance spectra from the AR structure optimization process when varying the number of layer pairs. The high-index layers contain 20% aluminum and the center wavelength is 961 nm for all cases. The optimized device included 2.5 pairs.

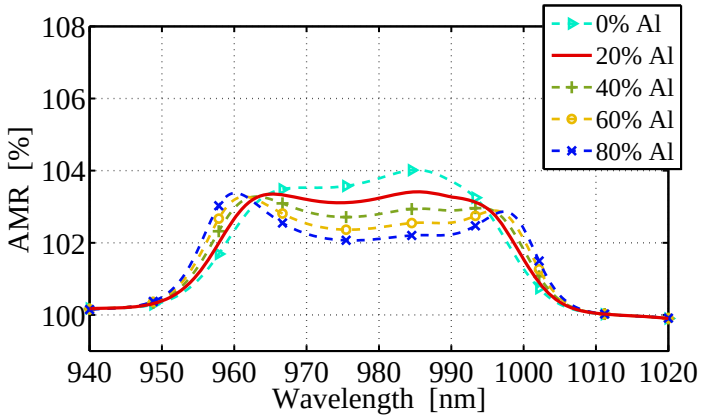

Figure 3.18: Simulated reflectance spectra from the AR structure optimization process when varying the aluminum composition of the high-index layers. The number of layer pairs is 2.5 and the center wavelength is 961 nm for all cases. 20% aluminum was later chosen for the optimized device.

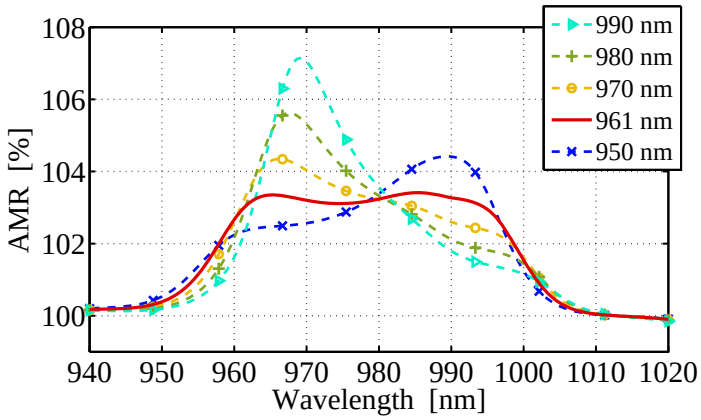

Figure 3.19: Simulated reflectance spectra from the AR structure optimization process when varying the center wavelength of the AR structure. The high-index layers contain 20% aluminum and the number of layer pairs is 2.5 for all cases. For the optimized device, a center wavelength of 961 nm was selected.

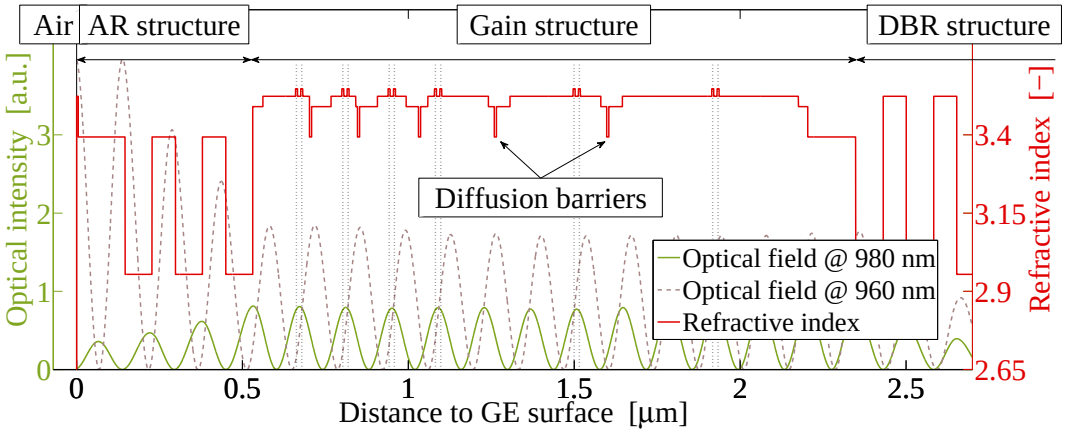

Figure 3.20: The calculated intensity of the optical field inside the subcavity for the optimized broadband design for the antiresonant wavelength and for a resonant wavelength. Also shown is the refractive index profile. The QWs are marked with vertical dotted black lines.

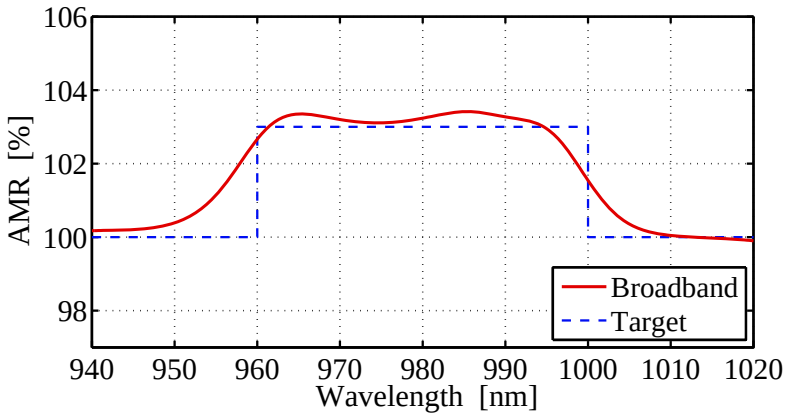

Figure 3.21: Simulated reflectance spectrum for the optimized device, and the target reflectance spectrum.

equally or close to equally populated, assuming a certain pump intensity and negligible saturation.

I also made simulations for a different type of AR structure with the $\lambda/2$ layer embedded with $\lambda/4$ layers on both sides, but this had only detrimental effects on the reflectance spectrum and this idea was abandoned.

Finally, I could draw the conclusion that 2.5 pairs of Al(20%)Ga(80%)As/AlAs layers with thicknesses corresponding to a center wavelength of $\lambda = 961$ nm was a near optimal combination that provided a sufficiently high AMR for the widest possible wavelength range while still keeping the variance low. This AR structure was calculated to have an AMR larger than 103% for a 33 nm wavelength range for an incident pump intensity of $8.1 \cdot 10^7$ W/m^2. The intensity of the subcavity field is shown in figure 3.20 for two wavelengths: the antiresonant wavelength (980 nm) and one

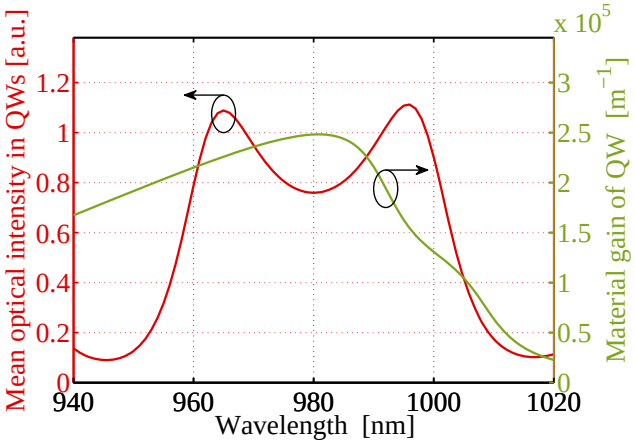

Figure 3.22: The average optical intensity in the QWs in the optimized GE and the material gain of one QW. The larger optical intensity at the resonant wavelengths compensates for the lower material gain.

of the resonant wavelengths (960 nm). The resulting AMR spectrum, shown in figure 3.21, is in good agreement with the target reflectance spectrum. Figure 3.22 illustrates how the resonance at 960 and 1000 nm balances the walk-off of the antinodes of the standing wave, such that the QW field is actually higher at these wavelengths, which in turn compensates for the material gain being lower there than in the middle of the tuning range.

3.3 Threshold simulations

As a complement to directly measuring the AMR of the gain element to validate the optimized design, I also simulated and measured the spectral behavior of the threshold pump intensity. The simulation results were achieved by simulating many AMR spectra for various incident pump intensities and interpolating for each wavelength to find the pump intensity needed to overcome the losses of the cavity. The cavity losses were assumed to come only from the out-coupling mirror and from reflections from the surfaces of the BRF. The loss from the out-coupling mirror is known from the data sheet and the losses from the BRF were estimated by measuring the power reflected out of the cavity from the two surfaces of the BRF, see figure 3.23 and equation 3.24, where P_{out} is the output power from the OP-SDL, P_{cav} is the unidirectional power of the intra-cavity field, P_{BRF} is the power of the reflections of each of the BRF surfaces, and R_{BRF} is the reflectance of the BRF. In this way, I obtained $R_{BRF} \approx 0.1\%$.

$$\begin{cases} P_{out} &= (1 - R_{OC})\ P_{cav} \\ P_{BRF} &= R_{BRF}\, P_{cav} \end{cases} \Rightarrow R_{BRF} = \frac{P_{BRF}}{P_{cav}} = \frac{P_{BRF}}{P_{out}}\,(1 - R_{OC}) \qquad (3.24)$$

In the threshold simulations the reflectance of the out-coupling mirror was

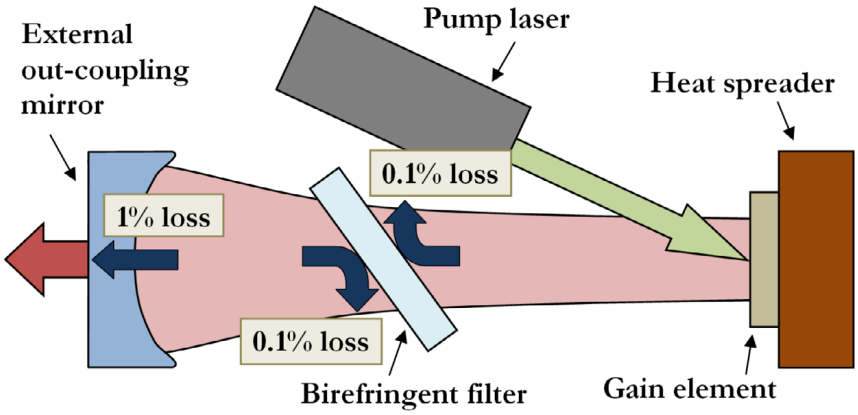

Figure 3.23: Schematic view of the setup with the cavity losses marked, for $R_{OC} = 99\%$.

set to either $R_{OC} = 97\%$ or $R_{OC} = 99\%$. In similarity with equation 2.1 the lasing condition for this cavity can be written, as in equation 3.25. Using this expression the calculated value for the required AMR of the gain element was $AMR = 101.2\%$ and $AMR = 103.3\%$ for 99% and 97% out-coupling reflectance, respectively, assuming that there were no scattering losses, $\alpha = 0$ m^{-1}. From these threshold AMR values the simulated threshold pump intensities were calculated at different wavelengths and compared with measurements.

$$1 = AMR\, e^{-\alpha\, 2L_c}\, R_{OC}\, (1 - R_{BRF})^2 \;\Leftrightarrow\; AMR = \frac{e^{+\alpha\, 2L_c}}{R_{OC}\, (1 - R_{BRF})^2} \qquad (3.25)$$

4

Fabrication of gain element

The gain element of an OP-SDL is a highly complex structure of more than 100 very thin layers. Since the thickness as well as the elemental composition of each layer can be chosen freely (within the limitations of strain), the degrees of freedom are numerous and the possibilities vast.

The thickness of a layer usually lies within 5 to 250 nm, or about 20 to 1000 atomic layers, and the technique for building these microstructures is called *epitaxy*[a]. This chapter describes the fabrication of a gain element from the epitaxial growth to the attachment of the processed gain chip onto the heat spreader.

4.1 Epitaxial growth of wafer

It is important to have accurate control not only of the thicknesses of the layers, but also of the compositions of the constituent elements of each layer, and a reliable method for this is epitaxial growth. There are nowadays mainly two variants of epitaxial growth: molecular beam epitaxy (MBE) and metal-organic chemical vapor deposition (MOCVD)[b]. The structures used for the work in this thesis were grown by MOCVD. The working principle is to let a controlled flux of molecules or a molecular gas be incident on a heated crystalline substrate, which is a flat disk typically ∼5–8 cm (2 or 3 inches) in diameter but only 0.3–0.5 mm thin. The molecules will decompose on the substrate and the individual atoms will merge into the crystalline pattern of the substrate, i.e. the *lattice*.

4.2 From wafer to gain element

The result of the epitaxial growth, a substrate covered with the thin multilayer structure, is called a *wafer*, which has to be further processed before it can be

[a] from Greek: *epi taxis* meaning "order upon"

[b] this variant is also referred to as metal-organic vapor phase epitaxy (MOVPE)

used. The processing takes place in a clean-room, where the environment is controlled regarding particle density, temperature, and humidity.

The standard way of epitaxial growth of OP-SDL gain elements is to start with the DBR on the substrate, continue with the active region, and end with the window layer at the top. In such a case the wafer can be directly used in a laboratory setup after cleaving and mounting.

However, it is sometimes preferred to epitaxially grow the structure in reverse order. The reason for this is that the substrate is a poor thermal conductor and the heat extraction efficiency can be greatly improved by removing the substrate. To do this, the structure is grown starting with the window layer on the substrate and ending with the DBR. The wafer is then turned upside down and the DBR is soldered directly to a heat spreader (HS) and the substrate is subsequently removed. This technique is called *flip-chip mounting* and has been used to produce the gain elements described in this thesis.

The remainder of this section will explain the process steps involved in producing a ready-to-use gain element from an unprocessed flip-chip wafer.

4.2.1 Wafer cleaving

Because the diameter of the wafer is so large compared to the thickness, it breaks easily. Therefore the wafer is separated into smaller, more manageable pieces by *cleaving*. Due to the crystalline structure, the wafer tends to break along one of the crystal directions in a perfectly straight line. It is therefore convenient to split the wafer by simply scratching its surface along a crystal direction and apply a slight downwards pressure. The ∼2 mm scratch is preferably made with a diamond needle at one of the wafer edges. The wafer is then sandwiched between two clean-room tissues with the scratch down before applying the slight pressure with some blunt object, e.g. a metal cylinder.

Cleaving the wafer to the final chip, a piece of about 3 mm × 3 mm, is done stepwise producing successively smaller pieces. As an example, the first cleaving step can produce pieces with dimensions about 18 mm × 15 mm, which is a suitable size for the following metallization process.

4.2.2 Metallization of DBR side

For efficient heat extraction — and to decrease the risk of breaking or losing the processed gain element — the chip is soldered onto a heat spreader. A surface that is to be soldered needs to be wet to provide good bonding with the solder, but semiconductor surfaces do not wet well. Therefore the surface needs to be coated with wettable metals, i.e. *metallized*.

Unfortunately, no single metal can be found that is both wettable and easily fastened to semiconductor surfaces. For instance, gold wets well, but is not easily attached to semiconductors. Titanium, on the other hand, readily adheres to semiconductor surfaces but neither wets well nor produces a mechanically

strong interface with gold. The solution is to use both of these metals but also to include an intermediate layer of platinum, which provides strong mechanical connections with both gold and titanium.

The metallization process in fact resembles the epitaxial growth of the MBE in some ways. High-purity lumps of metal are heated by high-energy electrons and the flux of metallic gas is guided onto the samples. In the Lesker Spector apparatus used in the work of this thesis, the samples are mounted with clamps. These effectively hinder the gaseous metal from reaching the shadowed parts of the samples, which thus remain unmetallized. As metallization is performed after the first cleaving step, a square of 15 mm $\times$ 15 mm on the surface of the sample is metallized.

Recommended metallization thicknesses are:

- 100 nm Ti, as the first layer on the semiconductor,
- 200 nm Pt, as the intermediate layer, and
- 4000 nm Au, as the wetting layer.

The evaporation rates are about 2 Å/s for Ti, 1 Å/s for Pt, and 4 Å/s for Au. Allowing time for cooling and preparing the vacuum chamber, the metallization of a sample requires in total about one hour with the Lesker Spector.

The process steps following the metallization require that the chip has its final size, so the 15 mm $\times$ 15 mm metallized piece is cleaved into 3 mm $\times$ 3 mm chips.

4.2.3 Soldering

Heat extraction is important for the laser performance, so the material of the heat spreader should have good thermal properties, such as copper or even better diamond. It is also essential to ensure that the connection between the metallized semiconductor chip and the heat spreader has a low thermal resistance. A polished heat spreader and a soft solder will reduce the amount of trapped, thermally insulating air. The softness of the solder will also reduce the mechanical strain due to the possible difference in thermal expansion coefficients of the heat spreader and the gain element. A good solder combination is In(80%)Pb(15%)Ag(5%). If the heat spreader is made of copper or diamond, the surface needs to be wetted and can be metallized or gold-plated, or alternatively a flux agent can be used. Preferably the solder is applied onto the heat spreader by evaporation in order to provide a thin and flat layer.

It is vital to stop the surfaces from oxidizing in the soldering process. Therefore it is recommended that it takes place in a controlled atmosphere, e.g. in a flow of inert gases. The heat spreader is heated to the melting point of the solder (circa 149 °C for the InPbAg solder) and the chip is mechanically pressed

onto the melted surface, after which the temperature can be lowered and the pressure released.

4.2.4 Mechanical substrate removal

After the chip has been fastened to a heat spreader, it is time to remove the substrate part of the chip. To shorten the process time, most of the substrate can be removed mechanically in a process called *lapping* or *abrasive machining*. The idea is to grind down the substrate surface with a slurry of a very fine powder, for instance consisting of silicon carbide or boron carbide.

In the MC2 clean-room at Chalmers, the grain size of the used powder is about 22 μm and the powder concentration of the slurry is about 25–50 volume-%. The powder is mixed with water on a glass plate, on which a large metal cylinder has been placed. The heat spreader is temporarily glued to a smaller metal cylinder using a low temperature wax, which melts already at ∼70 °C. The small cylinder is very tenderly placed with the chip down in a hole in the larger cylinder. Using gentle hands and tiny vertical forces both cylinders are moved across the glass plate in figures-of-eight and the substrate is ground at a rate of about 5-10 μm/figure-of-eight. Much care must be taken in order to not crack the chip, and it is recommended to not lap the substrate to less than ∼150 μm thickness.

Note that it is also possible to skip this process step altogether and just perform wet etching, if high yield is more important than short process time, since it is not unusual to crack the chip during lapping.

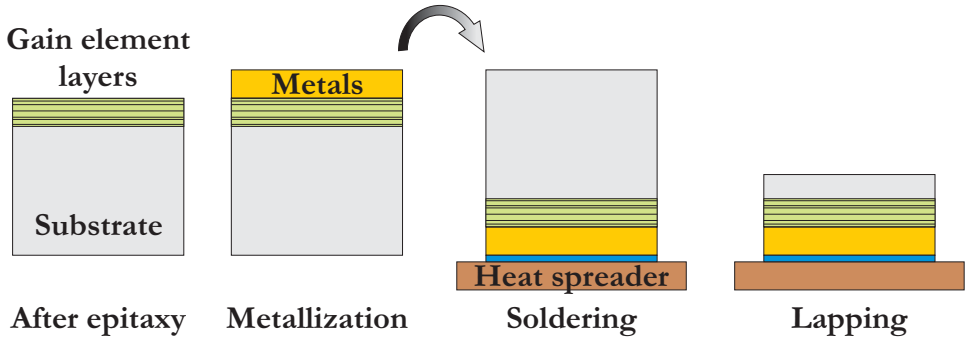

Figure 4.1: The chip in the first fabrication steps: Epitaxial growth, metallization, soldering, and lapping.

4.2.5 Wet etching

The remaining part of the substrate has to be removed by means of wet chemical etching in order to ensure an optimally flat surface. In this process step, the chip is completely submerged in various solutions of acids. The solutions contain one oxidizing component that oxidizes surfaces and one component that removes oxide-rich surface layers. These two chemical agents will thus in effect dissolve

the substrate layer by layer. To protect the chip structure from lateral etching, the sides of the chip should be protected e.g. with photoresist. A durable photoresist is AZ1512, which can be applied by means of a clean-room cotton tip. After application, the photoresist should be hardened on a hotplate at 120 °C for 2 minutes. For more accurate control of the thickness, photoresist can be applied using a resist spinner, in which case AZ4562 is a good choice as resist. This photoresist will be spread to a 6.2 μm thick coating when spun at 4000 revolutions/min. After spinning, the photoresist should be hardened on a hotplate at 110 °C for 4 minutes.

Fortunately, different wet etching agents etch different materials at different rates, which enables the etching process to be selective [72]. For instance, a solution of 1:19 NH_4OH:H_2O_2 etches GaAs surfaces at about 3.5 μm/min but etches Al(x)Ga(1-x)As surfaces very lightly, as long as the aluminum content is larger than $x \geq 30\%$ [73, 74]. Thus, the chip structure can be protected by including carefully chosen etch stop layers next to the substrate in the epitaxial growth.

Häring *et al.* [24] recommends the use of three etch stop layers: 300 nm Al(85%)Ga(15%)As next to the substrate, an intermediate layer of 20 nm GaAs, and 70 nm AlAs as the final layer to be removed. A good combination of solutions to use for the removal of the substrate and these etch stop layers is:

- **Coarse substrate removal:** If the mechanical removal process step was not performed, most of the substrate can be wet etched by a 1:10 (20:200 ml) NH_4OH:H_2O_2 solution, which will etch the GaAs substrate at a rate of about 5 μm/min or 600 μm/120 min [73,74]. The thickness of the remaining chip should occasionally be monitored e.g. by removing the chip from the etch solution and measuring with a microscope or a surface profiler. The etching should stop when the thickness of the remaining layers is about 50–100 μm.

- **Fine substrate removal:** 1:19 (15:285 ml) NH_4OH:H_2O_2 to remove the remaining GaAs substrate at a rate of about 3.5 μm/min [73, 74], and leave a flat surface. This solution will only lightly etch the AlGaAs etch stop layer. The surface appearance will change from the dull or darkly reflecting substrate to the reddish surface of the AlGaAs layer.

- **AlGaAs removal:** 5% (50 ml) HF for ∼15 s[c] to etch the AlGaAs layer at a rate of about 2 μm/min. This solution will not etch the GaAs etch stop layer. During etching, the color of the surface will quickly alternate through the colors of the rainbow and finally end up at the light gray and mirror-like surface of the GaAs layer [75, 76].

[c]NB: This etch time is longer than theoretically necessary, but a slight over-etch will allow for the whole surface to be fully etched.

- **GaAs removal:** 1:19 (15:285 ml) NH_4OH:H_2O_2 for just a few seconds[d] to etch the GaAs layer at a rate of about 3.5 μm/min [73, 74]. This solution will not etch the AlAs etch stop layer, which will appear reddish.
- **AlAs removal:** 2.5% (100 ml) HF for ∼15 s[e] to etch the AlAs layer at a rate of about 1 μm/min [75, 76]. This solution will not etch the GaAs window layer, which is the first layer of the gain element structure and which will look light gray and mirror-like.

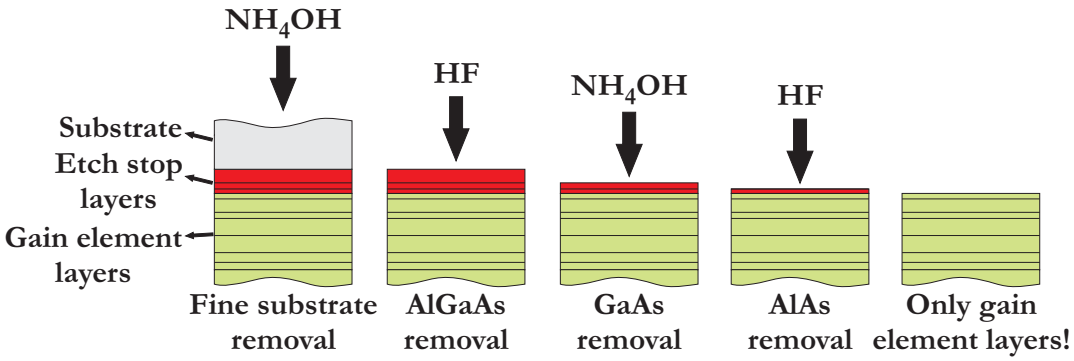

Figure 4.2: The four steps of the wet etching process resulting in a chip with only the layers left that are needed for the chip to serve as a gain element in an OP-SDL setup.

When etching, it is important to ensure that the chip is always surrounded by fresh etch solution, which can be accomplished by stirring the solution lightly with a magnetic stirrer and having a large solution volume. This is particularly important if the mechanical etching process step was not performed since the amount of material to remove is so large. The chip should be generously sprayed with deionized water when switching between the etch solutions, to not contaminate the solutions with residual agents from other solutions.

4.2.6 Cleaning of the chip and heat spreader

Lastly, the photoresist is removed and the chip surface cleaned, for instance using this combination of solvents:

- **acetone** at 50 °C for ∼5 minutes, to dissolve the photoresist,
- **methanol** for ∼30 seconds, followed by
- **isopropanol** for ∼2 minutes, to remove any residual contamination from the chip surface.

The heat spreader is now ready to be attached to the heatsink, and then the chip is ready to be optically pumped and serve as the gain element in the external cavity of an OP-SDL.

[d] NB: slight over-etch, see footnote c
[e] NB: slight over-etch, see footnote c

5
Experimental evaluation

To see how well the designed broadband gain element performs in practice, I conducted a line of experiments, of which the most important are presented in this chapter. First, I will in some detail describe the different parts of the experimental setup in the laboratory in section 5.1. Then I will present experimental results in section 5.2. Particularly important are the measurements in sections 5.2.1 and 5.2.2, in which the design is experimentally validated through measurements of the active mirror reflectance and the threshold pump intensity for different wavelengths. I also performed high-power tuning experiments, which are shown in section 5.2.3, and measurements of the output power of the OP-SDL under different driving conditions in section 5.2.4.

5.1 Lab setup

A schematic of the laboratory setup can be seen in figure 5.1. It consists of the OP-SDL with the pump laser and the laser cavity, including the gain element (GE) and out-coupling mirror (OC) and possibly also a birefringent filter (BRF) as an intra-cavity component. The other components shown are used for monitoring the output power and spectral characteristics. When aligning the out-coupling mirror and pump laser, the lens and the CCD are inserted in the beam but are removed as soon as lasing is initiated.

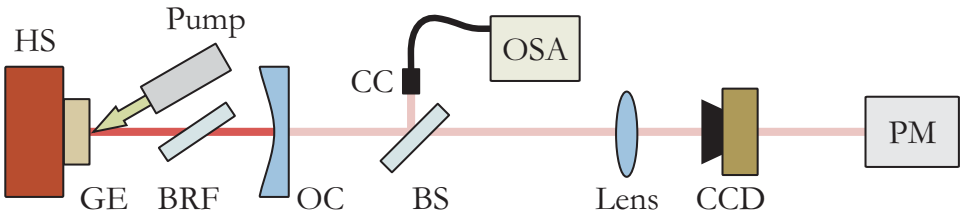

Figure 5.1: Schematic view of the laboratory setup during measurements. HS: heat spreader, GE: gain element, BRF: birefringent filter, OC: out-coupling mirror, BS: beam-splitter, CC: cosine-corrector lens, OSA: optical spectrum analyzer, PM: power meter.

5.1.1 OP-SDL cavity

Before the experimental evaluation the gain element is mounted on a heat spreader (HS), according to the procedures described in chapter 4. When used in an OP-SDL setup, the HS should in turn be mounted on a heatsink for efficient cooling. While the small size of the HS allows for it to be made of almost any material with a good heat conductivity, such as copper or diamond, the heatsink is too big to be made of anything more expensive than copper; in most measurements in this work the size of the heatsink was 40 mm×40 mm×10 mm. Since it is vital to have an unobstructed heat flow from the gain element, a thin and thermally conducting layer between the HS and the heatsink is required to fill any insulating pockets of trapped air. For the material in this layer, a soft foil of indium[a] or a thin film of thermal paste can be used.

At the other end of the linear OP-SDL cavity, an out-coupling mirror mounted on a translator was used to extract the laser beam. I used plano-concave mirrors[b] with transmittance values of 0.5–3.0% and a transverse diameter of 10 mm. The radius of curvature of the concave side was between 50 and 300 mm.

5.1.2 Cooling

The temperature of the active region in an OP-SDL gain element can increase by 50–200 °C during high-power operation [77]. Since many material and structural properties, with bandgap energy (for the QW layers) and refractive index (for all layers) being the most important, are temperature dependent, a large increase in temperature obviously has an impact on the performance. Therefore, in laser development much effort is devoted to extracting the heat from the active region in an efficient way, and many different techniques are used. Since the gain element is much thinner in the longitudinal dimension than the pump spot is in the two transverse dimensions, the heat transfer inside the gain element is essentially one-dimensional, perpendicular to the surface. The function of the HS is to make the heat flow more three-dimensional, which is more efficient, while the heatsink should provide an efficient transport of the heat to the cooling medium.

In some cases, an intra-cavity HS is used, which is a thin (∼300 μm) sheet of a transparent material with a very high thermal conductivity, often diamond or SiC, that is bonded to the gain element surface most commonly through liquid capillary bonding. This convenient and non-permanent bond method uses the capillary force of a thin film of a liquid (e.g. methanol) that is sandwiched between two smooth surfaces with a slight pressure. As the liquid evaporates, the surfaces are pulled closer until they reach atomic contact, and the gap between the surfaces can be as small as 15 Å [78]. For a successful capillary

[a] Ellsworth Adhesives, model: SMA-TIM Heat-spring
[b] wzw optic AG, model: S-SET-980NM

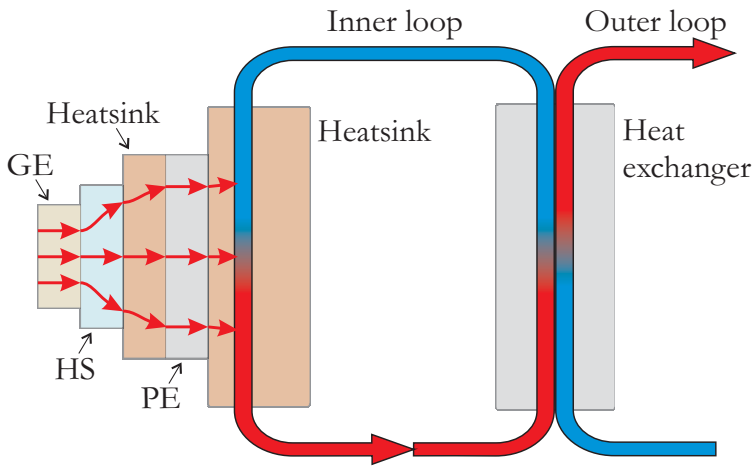

Figure 5.2: A schematic of the transfer of heat from the gain element. PE: Peltier element.

bonding, it is important to remove all foreign particles between the smooth surfaces to ensure that the trapped pockets of air are as small and as few as possible. Though simple and efficient, the intra-cavity HS is not optimal for continuously tunable OP-SDLs since the HS introduces an etalon effect and the lasing wavelength will thus hop between the resonance wavelengths of the etalon. A wedged HS with non-parallel surfaces and AR coating can however decrease this detrimental effect [79].

Another method for heat extraction is the flip-chip method, which was used in this work (see section 4.2 for fabrication details), and relies on removing the substrate and extracting the heat through the relatively thin DBR. To extract heat through the layers of the DBR, a heatsink at the far end of the DBR is needed, with a temperature that is considerably lower than that of the active region. Since the heat extraction is more efficient the larger the temperature difference, I cooled the heatsink using a thermoelectric cooler (TEC)[c], which is a device that uses the Peltier effect to transfer heat from one side of it to the other. The cool side of the TEC was permanently bonded to the heatsink using heat-conductive epoxy glue[d] and to increase the heat extraction capacity further, an even larger copper heatsink was bonded in the same way on the hot side of the TEC. The heat was thus transferred from the heatsink with the gain element to the larger heatsink, which was in its turn cooled with a double-loop liquid system. The inner loop of the system was closed and used coolant fluid that was cooled via a heat exchanger by the open outer loop using running cold water from the tap. A sketch of the cooling system can be seen in figure 5.2.

The TEC between the copper heatsinks was controlled by a commercial temperature controller[e]. The entire cooling system allowed me to control the

[c]Elfa, model: Supercool, 75-661-77
[d]Microjoining, model: Epotek H20E
[e]Thorlabs, model: TED350

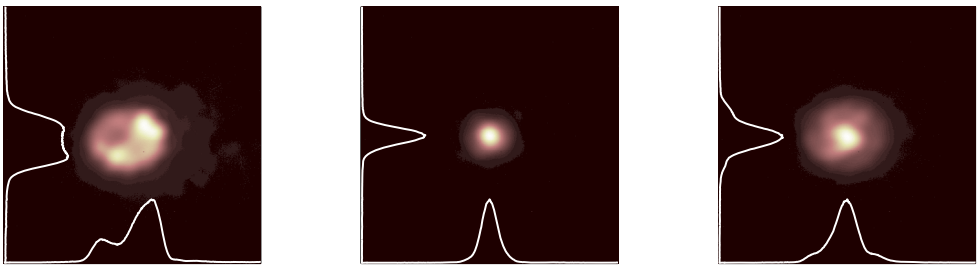

(a) Pump spot before focus. (b) Pump spot at focus. (c) Pump spot beyond focus.

Figure 5.3: The intensity distribution of the pump spot in three planes near the focus of the pump beam.

temperature of the smaller heatsink from −20 °C to +30 °C almost regardless of incident pump power and OP-SDL output power.

5.1.3 Pump laser

The pump laser was a diode laser[f] with a wavelength of 808 nm, which is the most common wavelength for pumping GaAs absorption barriers. The output light from the laser diode was fed into a high-power multi-mode optical fiber[g] with core and cladding diameters of 100 and 140 μm, respectively. The other end of the fiber was connected to a lens package[h], consisting of a collimating and a focusing lens with focal lengths of 150 mm and 120 mm, respectively. The incidence angle was $\sim 30°$ with respect to the GE surface normal. The maximum output power of the pump laser was 16.7 W, as measured after the pump lens package.

The lens package produces a focus of the pump light in free space after ∼10 cm propagation. The shape of the pump spot before, at, and beyond focus are shown in figure 5.3. It is clear that the pump spot is near Gaussian only at the focus because of the multimode nature of the pump light. Mostly the pump spot was operated slightly out of focus to obtain a desired size of the pump beam on the gain element.

In the collaborations with Ulm Universität in Ulm, Germany, College of Optical Sciences in Tucson, USA, and ETH in Zürich, Switzerland, more powerful pump lasers were used, and separate, cylindrical lenses were used instead of a fixed lens package.

[f] LIMO GmbH, model: LIMO35-F100-DL808
[g] LIMO GmbH, model: LIMO-SMA905-F100-1.5
[h] US Laser Corp., model: N3303-6 and N3304-5

5.1.4 CCD cameras

A CCD camera[i] was used in combination with a camera objective to image the gain element. The detector size of this CCD camera was 510 ×492 pixels with a pixel size of 17 μm (13 μm) in the horizontal (vertical) direction. With this imaging system I could measure the diameter of the pump spot on the chip by means of a video analyzer system[j].

For the capture of beam intensity profiles a CCD detector array[k] was used, with a pixel size of 4.4 μm and a detector surface size of 1600 ×1200 pixels. This CCD was connected via FireWire to a standard computer with an image capturing software from *Spiricon*. The camera was equipped with various neutral density optical filters to attenuate the laser intensity.

5.1.5 Spectrometer

For general wavelength measurements I used a fiber spectrometer[l] with a cosine-correcting lens, which made it possible to collect light from many incidence angles. A reflecting filter with 79% transmittance was used as a beam-splitter to extract part of the output laser light and guide it into the cosine-corrector through a variable attenuating filter plate. The resolution of this spectrometer was 0.3 nm.

5.1.6 Power measurement

The output power was measured with a thermal surface absorber measurement head[m] connected to a power meter[n]. This equipment had a ±3% measurement error according to the data sheets.

5.1.7 Birefringent filter

As a wavelength-selective element I used a birefringent filter (BRF)[o] made of a 1.0 mm thick crystalline quartz plate, with a free spectral range of ∼80 nm. It was mounted on a goniometer providing a way to rotate the BRF around an axis normal to its surface. More details on the tuning process can be found in section 2.3.1.

[i] Hamamatsu, model: C3057
[j] Colorado Video Inc., model: Video Analyzer 321
[k] Spiricon, model: Scorpion
[l] Avantes, model: AvaSpec3648-UA-25-AF
[m] Thorlabs, model: S314A
[n] Thorlabs, model: PM300E
[o] VLOC Inc., model: BF25.4-2T

5.2 Measurements

In this section I will first describe how the setup was aligned and then describe the performed measurements.

To begin, the optical axis of the external cavity should be aligned. This was done by guiding the output light from a standard 633 nm He-Ne laser onto the gain element so that the laser light was reflected back to the He-Ne laser output aperture, i.e. so that the light retraces its path. I did this by adjusting the angle of the gain element using tuning screws on the heatsink, and by adjusting the angle of the incident laser light. The out-coupling mirror was then moved into the beam and its angle adjusted so that the reflected laser light from the planar side also hit the He-Ne laser output aperture. The surfaces of the gain element and the out-coupling mirror were thus parallel to each other and perpendicular to the optical axis.

Next, I adjusted the pump spot to the size I wanted to use for the experiment by changing the distance between the gain element and the lens package of the pump laser. The size of the pump spot was measured using the image on the CCD. With the video analyzer system I could determine the horizontal and vertical distance between the points where the intensity had dropped to e^{-2} of its peak value, the average of which I used as an approximate measure for the pump beam diameter. Since the image was magnified by the camera objective, the imaged beam diameter had to be converted to the physical beam diameter by moving the gain element a certain distance using a well-calibrated translator and measuring the distance moved on the CCD image. By adjusting the distance between the lens package and the gain element, I could continuously change the size of pump spot until it reached the desired value. I commonly used pump spots with diameters between 180 μm and 350 μm. The precision of the measurement of the pump spot diameter was about 10% as determined by comparing repeated measurements.

The CCD image was also used to align the out-coupling mirror in the transverse directions. In this case, low power light from the pump laser generated spontaneous emission from the QWs in the gain element. The emission produced two images on the CCD: one direct image and one that was twice reflected, first on the out-coupling mirror and then on the gain element. The out-coupling mirror could thus be aligned by moving the out-coupling mirror so that the twice reflected image was overlayed with the direct image. The pump power was then increased to slightly above the expected threshold of the OP-SDL. Due to the out-coupling mirror and the gain element not being exactly parallel, lasing still did not always commence. Nevertheless, the position of the out-coupling mirror provided a good enough starting point for a quickly performed systematic translation of the out-coupling mirror until lasing was initiated.

As mentioned in section 2.2, good overlap between pump spot and cavity field is important to suppress higher order transverse modes of the output

beam. Therefore the cavity length should be adjusted so that the size of the fundamental mode, as determined by equation 2.3, is approximately equal to the size of the pump spot. In practice it turns out that to obtain a high-power beam of good quality, the size of the pump spot should be somewhat larger than the fundamental mode, by a factor of 1.2–1.4.

In the tuning experiments, the BRF was inserted into the cavity and aligned in the Brewster angle to the cavity optical axis by means of the He-Ne laser mentioned previously. A polarizer was used to linearly polarize the He-Ne laser beam in the same plane as the lasing field of the OP-SDL, i.e. in the horizontal plane, and the angle between the BRF surface normal and the cavity optical axis was adjusted until the reflections from the BRF surfaces were minimized.

During some experiments I experienced problems with catastrophic optical damage of the GE surface at the position of the pump spot, which occurred for high pump intensities and, for reasons not entirely understood, more often for short wavelengths. Probably it partly had to do with excessive heat in the active region due to insufficient *photon cooling*. Photon cooling means that the optical emission from the OP-SDL helps to remove energy from the charge-carriers without converting it to heat in the GE. Thus, as the OP-SDL output power, P_{out}, decreases, the power that has to be dissipated from the gain element, P_{diss}, increases, see figure 5.4(a), if the incident pump power, P_{pump}, is constant. If the cooling system is not sufficiently powerful, the temperature of the active region will then increase. The photon cooling effect is clearly illustrated in the plot of the temperature of the heatsink in figure 5.4(b), in which the temperature increases at the edges of the power spectrum, where the output power of the OP-SDL is decreasing. This particular measurement was performed using an old cooling system, which could only partially compensate for this effect.

5.2.1 Active mirror reflectance

To validate the design concepts used in chapter 3, I measured the *active mirror reflectance* (AMR), i.e. the spectral reflectance of the gain element under pump excitation. The AMR is also the quantity that is optimized in the design, so the measurement allows for a direct comparison between actual and theoretical performance. The setup for this measurement, schematically shown in figure 5.5 and described in detail in paper I, probes the reflectance of the gain element with a tunable laser source, in this case a Ti-sapphire laser. The gain element is simultaneously being optically pumped by a pump laser, thus allowing for the gain element to function as an active mirror with a reflectance that can exceed 100%.

To compensate for possible power fluctuations of the probe beam, two photo-detectors are used. The probe beam is split by a beam-splitter (wedged to avoid interference), from which the first reflection is measured by the first photo-detector yielding a reference of the power that is incident on the gain ele-

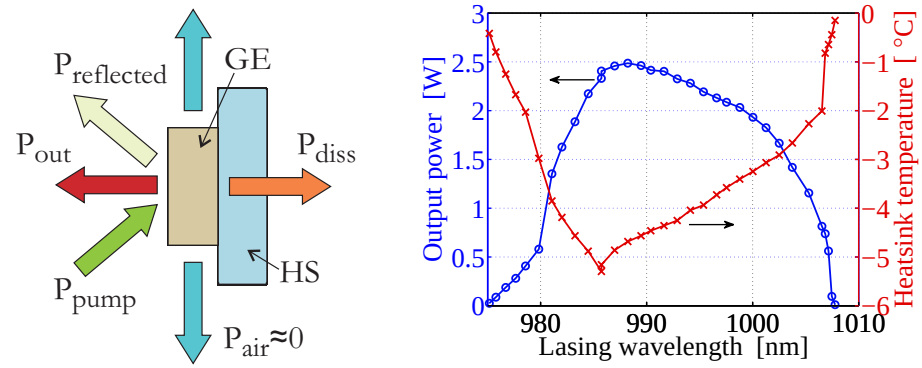

(a) Schematic of the heat transfer of the gain element.

(b) Power spectrum and heatsink temperature for an OP-SDL with a broadband gain element under high pump power.

Figure 5.4: The effect of photon cooling. The power flux to and from the gain element are shown in (a). Note how the temperature of the heatsink increases as the output power decreases in (b). This is because the power dissipated as heat increases as the optical output power decreases.

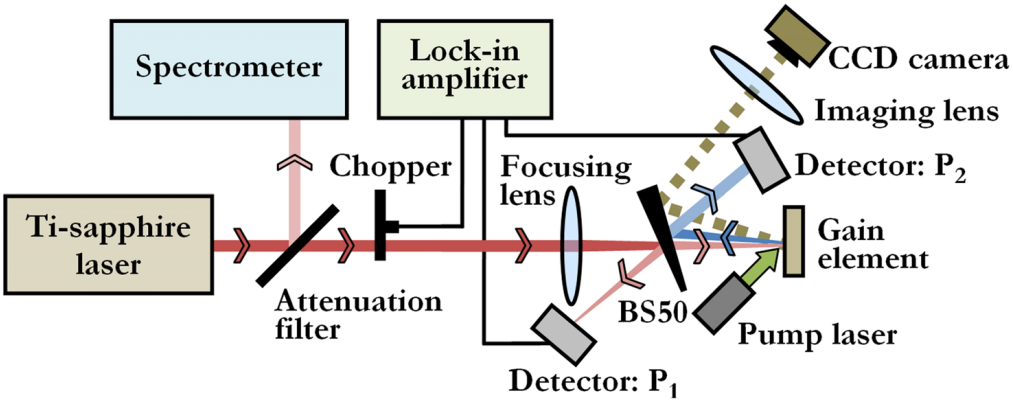

Figure 5.5: Schematic overview of the measurement setup (BS50: Wedged 50–50 beam-splitter). The two photo-detectors are intentionally oblique to the incident light, to prevent interference from reflections. The dashed line indicates the imaging of the gain element onto the CCD camera.

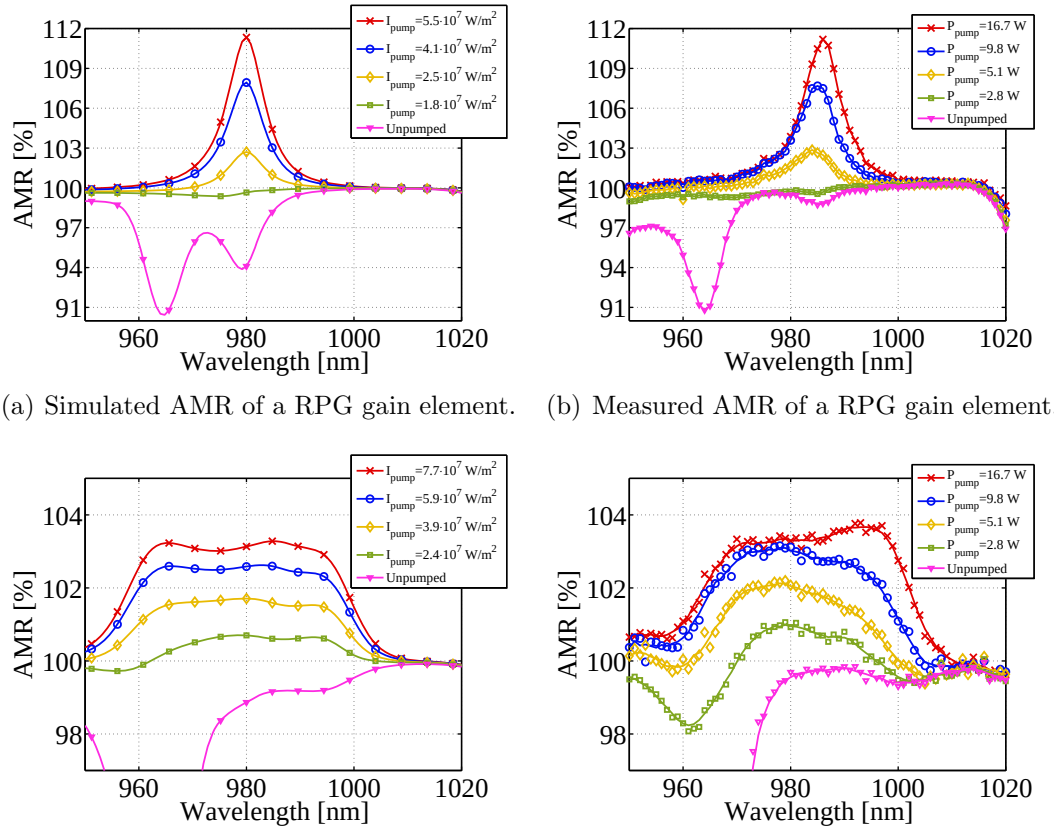

(a) Simulated AMR of a RPG gain element.

(b) Measured AMR of a RPG gain element.

(c) Simulated AMR of a broadband gain element.

(d) Measured AMR of a broadband gain element.

Figure 5.6: Simulated and measured AMR of a RPG and a broadband gain element for various incident pump powers.

ment (P_1). The transmitted beam is reflected on the gain element and incident on the second photo-detector, which thus measures the reflected power from the gain element (P_2). To account for uncertainties in the optical properties of the setup elements, a measurement on a sample with a known reflectance — such as a high-reflectance mirror — is required. The AMR of the gain element at a certain wavelength can then be calculated using equation 5.1. Here, R_{cal} is the known reflectance from the reference sample, and P_1^{cal} and P_2^{cal} are the detector readings when this sample is measured.

$$AMR\left[\lambda\right] = R_{cal}\left[\lambda\right] \frac{P_1^{cal}\left[\lambda\right]}{P_2^{cal}\left[\lambda\right]} \cdot \frac{P_2\left[\lambda\right]}{P_1\left[\lambda\right]} \tag{5.1}$$

In the measurements, the alignment of the probe and pump laser spots is crucial, but is simply performed by imaging the gain element surface with, for instance, a camera objective and a CCD camera. In the setup realized in paper I, the P_2 detector was removed to allow free line-of-sight via reflection on the beam-splitter. The focusing lens is inserted to obtain sufficient pump

intensity. The attenuation filter prevents saturation of the photo-detectors and also doubles as a beam-splitter, picking off a weak reflection for spectral control.

The results from the measurements are shown in figure 5.6, where figures 5.6(a) and 5.6(b) are the simulated and measured AMR of a conventional RPG gain element, respectively. Figures 5.6(c) and 5.6(d) show the simulated and measured AMR of a broadband gain element, respectively, and the striking agreement between simulations and measurements gives credibility to the measurement method as well as to the simulations. Furthermore, the measured AMR of the broadband gain element is indeed more broadband than the measured AMR of the RPG gain element, proving that the design strategies for wide tunability employed in this work are successful.

5.2.2 Threshold

For further validation of the fabricated gain elements, I also performed measurements of the threshold pump intensity versus wavelength. This kind of measurement is not commonly performed, or at least not reported, but is in fact quite informative and simpler to implement than the AMR measurement in the previous section. In this case the gain element is inserted in the laser cavity, and the output from the laser is studied. The measurements were performed by tuning the BRF to a certain wavelength and increasing the pump power until the OP-SDL began to lase. The corresponding simulation results were achieved by the method described in section 3.3.

Results from the threshold measurements with comparisons between measurements and simulations for a conventional and a broadband design can be seen in figure 5.7. It is clear from the much wider low-threshold regime of the broadband design that it indeed shows promise of a wider tuning range, and the good agreement with the simulation results shows that the physical models used are adequate. Since the precision in the diameter measurement is quite poor, and this error is squared in the conversion from pump power to pump intensity, comparisons between absolute values of pump intensities are difficult to make.

Results from these measurements are also presented in paper II.

5.2.3 High-power CW tuning

Since the AMR and threshold measurements strongly indicated broadband properties of the gain element, high-power CW tuning experiments were performed to investigate the tuning range of an OP-SDL employing a broadband gain element. A wide tuning range is evidently of great practical interest, and some of the most prominent published results for OP-SDLs are summarized in table 5.1. The comparison between different tuning experiment results is not entirely straight-forward, since both high power and wide tuning range is usually of importance, and there is a trade-off between these two parameters.

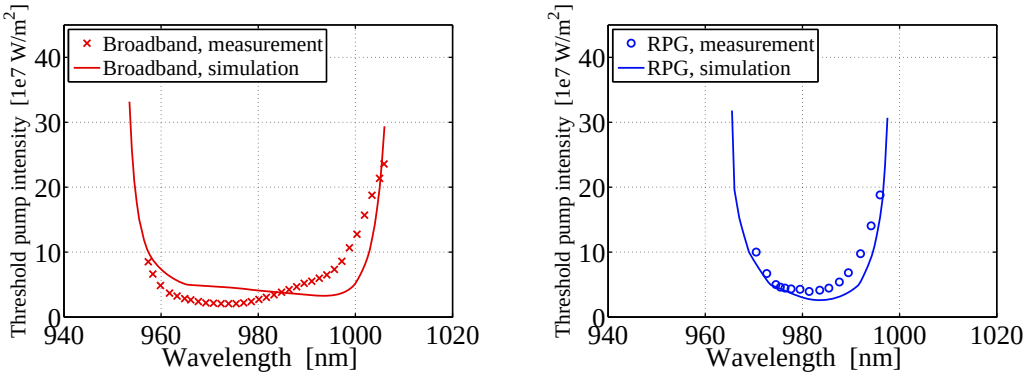

(a) Measured and simulated threshold pump intensity for an OP-SDL with the broadband gain element.

(b) Measured and simulated threshold pump intensity for an OP-SDL with a conventional RPG gain element.

Figure 5.7: Measurements and simulations of threshold pump intensity for an OP-SDL with the optimized broadband gain element and with a conventionally designed gain element. The reflectance of the out-coupling mirror was 99% in both measurements.

Table 5.1: Prominent published results for high-power tuning of OP-SDLs. P_{max} is the maximum output power while tuning, λ_{center} is the center wavelength of the tuning range, and $\Delta\lambda$ is the full width of the tuning range. "Strategy" refers to the method used to obtain broadband operation.

P_{max} [W]	λ_{center} [nm]	$\Delta\lambda$ [nm]	Strategy	Reference
0.4	2000	156	a	[34]
2.2	1040	60	b	[80]
0.08	1180	69	b	[80]
2.6	990	43	c	Paper II
8.0	975	33	d	[35]
7.5	995	32	c	Paper III
11.0	972	21	d	[35]

a) Non-identical QWs with maximum gain at different wavelengths
b) Anti-resonant gain element with QD active region
c) Anti-resonant gain element with AR structure
d) Multi-chip cavity

Two power spectra for the broadband design are shown in figure 5.8, and are also presented in papers II and III. The power spectrum with the diamond HS shows a full tuning range of 32 nm with a peak power of 7.5 W for an incident pump power of 52 W, whereas the spectrum with the copper HS shows a tuning range of 43 nm with a peak power of 2.6 W for an incident pump power of 17 W. Figure 5.9 compares the conventional and the broadband design for two different reflectances of the out-coupling mirror. Figure 5.9(a) shows the results with an OP-SDL using the broadband gain element, with tuning ranges of 28 (43) nm and maximum output powers of 2.8 (2.6) W for $R_{OC} = 97\%\,(99\%)$. The tuning ranges for the conventional design was 17 (27) nm with maximum output powers of 3.1 (1.9) W.

That the broadband properties prevail under high pumping is obvious but the output power from the widely tunable gain element does not have the desired top-hat shape that was used for the target reflectance spectrum in the design, see figure 3.8. The reason for this is most likely that I have designed the AMR only for threshold conditions, and do not consider effects that become dominant at high powers, such as gain saturation and changes of material properties caused by the temperature increase.

The twin-peak appearance of the spectra for the conventionally designed gain element, which is especially notable for the higher out-coupling reflectance, seems to be somehow associated with a change in the polarization of the cavity field, since the reflection loss from the BRF is increasing in the central wavelength region, see figure 5.10(b). For comparison, the reflection loss from the BRF for the broadband design is shown in figure 5.10(a), and it is apparent that this design does not suffer from the same effect.

5.2.4 Power characteristics

A commonly measured quantity of a laser is its power characteristics, i.e. the relation between the incident pump power and the output power of the laser. Figure 5.11(a) shows a selection of plots of output power versus incident pump power for an OP-SDL with a broadband GE on a copper HS. The figure shows a plot for the free-running OP-SDL, i.e. with the BRF removed from the cavity, as well as three plots when the OP-SDL was tuned to three different wavelengths: $\lambda_1 = 979$ nm, $\lambda_2 = 996$ nm, and $\lambda_3 = 1005$ nm, respectively. These wavelengths were chosen since they represent the wavelength for maximum output power in the power spectrum in figure 5.8 (λ_2) and the wavelengths for an output power of 1.5 W ($\lambda_{1,3}$). As is quite evident, the threshold pump power increased for increasing wavelength, from 2.4 W for λ_1 to 9.8 W for λ_3. This can also be seen in figure 5.7(a), where λ_1 can be found in the regime of low threshold whereas λ_2 and λ_3 are found at the edge or outside of this regime.

There is a difference in slope efficiency of the power-power plots for the three wavelengths, which can be explained by figure 5.10(a). The slope efficiency can be defined as in equation 5.2, in which the reflection loss from the BRF is

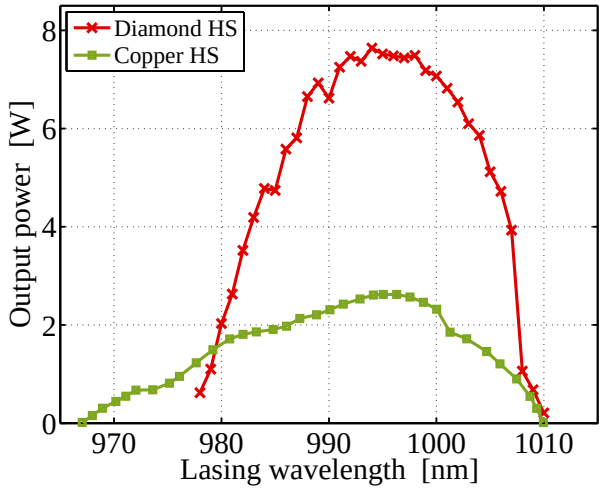

Figure 5.8: Measured power spectra of OP-SDLs with broadband gain elements mounted on different heat spreaders. The tuning range for the OP-SDL with the diamond-mounted gain element was 32 nm for an incident pump power of 51 W, and for the copper-mounted gain element the tuning range was 43 nm for an incident pump power of 17 W.

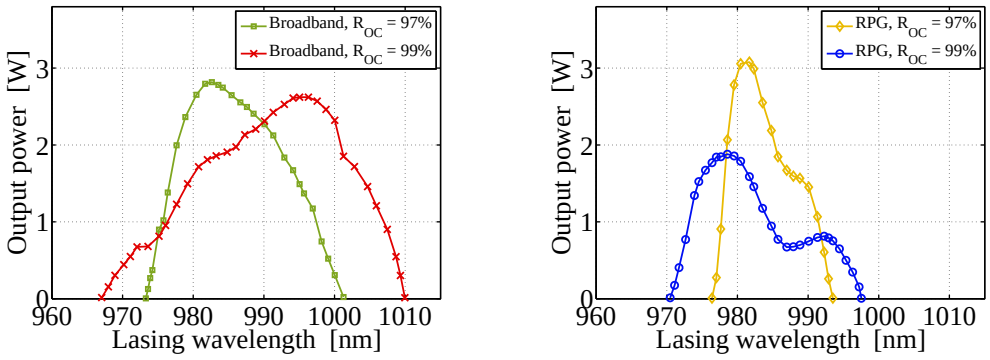

(a) Power spectrum for an OP-SDL with the broadband gain element for two different out-coupling reflectances.

(b) Power spectrum for an OP-SDL with a conventional RPG gain element for two different out-coupling reflectances.

Figure 5.9: A comparison between the power spectrum for an OP-SDL with the optimized broadband gain element and a conventionally (RPG) designed gain element. When the broadband gain element is used in the OP-SDL cavity, the tuning range increases significantly. The tuning range is also wider for a higher out-coupling reflectance.

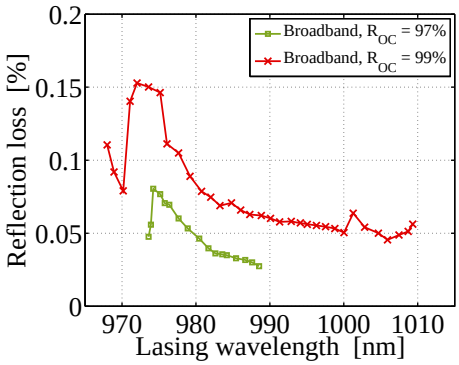

(a) Reflection loss for an OP-SDL with the broadband gain element for two different out-coupling reflectances.

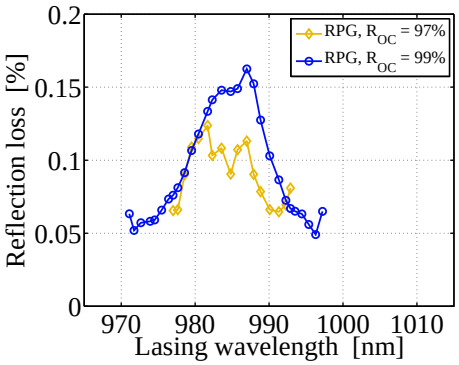

(b) Reflection loss for an OP-SDL with a conventional RPG gain element for two different out-coupling reflectances.

Figure 5.10: A comparison between the reflection losses from the BRF for an OP-SDL using the optimized broadband gain element and using a conventionally (RPG) designed gain element. The reflection loss was calculated using equation 3.24.

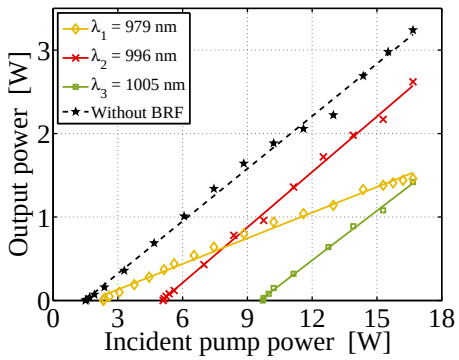

(a) Power-power plot for an OP-SDL employing a copper-mounted gain element. The plot shows the power characteristics when the OP-SDL was tuned to three different wavelengths, and also for the free-running OP-SDL, i.e. without the BRF in the cavity. The markers represent data points and the lines are linear fits.

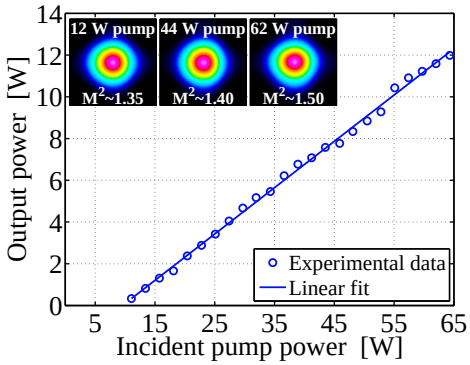

(b) Power-power plot for an OP-SDL employing a diamond-mounted gain element, but without a BRF. Insets show intensity distributions at three pump powers with the corresponding M^2 values.

Figure 5.11: OP-SDL output power versus incident pump power for OP-SDLs using optimized broadband gain elements mounted on (a) a copper HS and on (b) a diamond HS.

included in the total optical losses, α_{total}. Since the reflection loss is lower for longer wavelengths, so are the total optical losses. Thus, as the mirror loss, α_{mirror} and the internal quantum efficiency, η_i, are constant, the slope efficiency is increased with increasing wavelength, from ∼10% for λ_1 to ∼20% for λ_3.

$$SE \propto \eta_i \cdot \frac{\alpha_{mirror}}{\alpha_{total}} \tag{5.2}$$

Measurements were also performed on a free-running OP-SDL with a broadband gain element mounted on a diamond HS, see figure 5.11(b). An output power of the OP-SDL of 12 W was measured, at an incident pump power of 53 W, with no sign of thermal roll-over. Also shown in the figure are the intensity distributions at three pump powers, suggesting a very good beam quality even at high pump and output powers.

6

Full characterization of the laser beam

Because of its high coherence and brightness, the emitted radiation from high-power lasers such as the OP-SDL has numerous applications in visualization, laser machining, and detection. These applications generally require that the laser beam is of high quality, i.e. that the intensity is contained within a well defined beam lobe and that the wavefronts are nearly spherical so that the beam can be precisely focused and expanded by regular (spherical) lenses. However, high-power lasers generally have larger dimensions than low-power lasers, and therefore the beam quality is more sensitive to thermal and mechanical effects as well as to the unavoidable lateral non-uniformity of the gain element in the OP-SDL. It is therefore of utmost importance to be able to measure the beam quality, both to assess whether the particular laser device can be used for the intended application, and as a diagnostics tool to indicate possible non-ideal processes in the intra-cavity light generation. The most common measure of the beam quality is the M^2 value, which is an indication of how close the beam is to an ideal Gaussian beam. More specifically, the M^2 value is the ratio of the beam parameter product (BPP) of the measured beam to that of a Gaussian beam at the same wavelength, as given by equation 6.1. The BPP is the beam waist diameter, $2\omega_0$, multiplied with the far-field divergence full-angle, 2θ, which for an ideal Gaussian beam equals $4\lambda/\pi$ [81].

$$M^2 = \frac{BPP_{measured}}{BPP_{Gaussian}} = \frac{2\omega_0\, 2\theta}{4\,\lambda/\pi} \tag{6.1}$$

Common techniques for measuring $2\omega_0$ and 2θ are either to monitor the power drop as a knife-edge or circular aperture cuts into the beam, or to capture cross-section intensity profiles by a scanning detector. Both techniques involve measurements at two or more positions along the optical axis, since determining the beam parameter product requires accurate measurements of the near-field, for obtaining $2\omega_0$, as well as of the far-field, for obtaining 2θ [82]. Thus measurements are in general made at different instants in time, which for pulsed or spontaneously fluctuating laser output fails to produce a reliable measure of the M^2 value.

In this chapter I describe a new technique for fully characterizing a laser beam and, based on this, determining its M^2 value. The full characterization means that rather than extracting a single figure of merit, such as the M^2 value, we determine the entire optical field distribution — amplitude and phase — in a beam cross-section. This technique relies on a single, instantaneous measurement and thus removes the uncertainty inherent in having to relate measurements spread out in time. The instantaneous measurement results in two cross-section intensity distributions, from which the optical phase distribution of the beam is numerically retrieved by the *Gerchberg-Saxton* (GS) algorithm. Knowing both the amplitude and phase distributions in a plane means that the beam is fully characterized, and the M^2 value is then easily calculated by numerically simulating the insertion of a thin lens into the beam and making virtual beam cuts to find the beam waist and divergence.

An overview of beam characterization techniques is given in section 6.1, followed in section 6.2 by a description of the general GS algorithm, which is essential in the phase retrieval, or equivalently, in the wavefront reconstruction. The measurement principle of the new method is presented in section 6.3 and an application example is shown in section 6.4. Lastly, I briefly discuss imaging a coherent and extended object in section 6.5, for reasons that will become obvious. More details are also given in paper IV.

6.1 Characterization methods

For a beam to be fully characterized, knowledge of both the amplitude and phase distributions of the beam cross-section in an arbitrarily located plane is required. Since the amplitude is simply the square root of the intensity, which can be directly measured with e.g. a CCD camera, the problem of full characterization lies mainly in determining the optical phase distribution.

For instance, the phase distribution can be obtained by an interferometric method, e.g. *wavefront shearing interferometry* [83], see figure 6.1(a). In this case, a modified Mach-Zehnder interferometer setup is used, in which the beam is split into two or more parts, which are recombined after separate propagation. If the propagation distances are not equal, for instance by introducing a slight angular difference (a so called *shear*), an interference pattern will be created, from which the phase information can be extracted. However, exact alignment is crucial and in many realizations a large number of measurements is necessary, which makes it difficult to obtain an accurate measurement for beams that are pulsed or otherwise fluctuate.

Perhaps the most common method to fully characterize the beam is to use a *Shack-Hartmann wavefront sensor* [84], see figure 6.1(b). It is an array of microlenses at a set distance from an array of sensors, the latter is usually realized with a CCD sensor. Any deviation from a flat wavefront will be apparent by a translational shift of the focal points on the sensor array. The partition of the

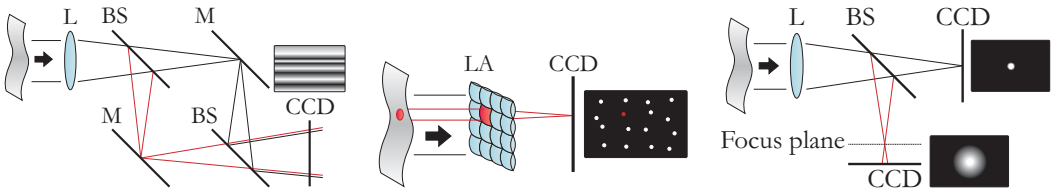

(a) Wavefront shearing interferometry (b) Shack-Hartmann wavefront sensing (c) Phase diversity

Figure 6.1: Sketches of working principles for three different methods for determining the optical phase distribution. L: lens, BS: beam-splitter, M: mirror, LA: lens array.

beam brought on by the microlens array reduces the spatial resolution. Further, the wavefront sensor needs to be calibrated using a reference beam with a known wavefront and is sensitive to alignment and vibrations. A variation of this principle is used in the recently developed *light field photography*, in which the phase information is (indirectly) recorded using a microlens array [85].

Another method is called the *phase-diversity* method and uses two images of the intensity distribution with a known phase difference to numerically reconstruct the wavefront [86], see figure 6.1(c). Often one image is the focus of the beam, while the other image is intentionally defocused by a high-quality lens with a precisely known focal length at the lasing wavelength. The measurement can be done simultaneously, for instance by introducing a beam-splitter and positioning the imaging equipment at carefully selected positions. Major drawbacks with this method are the need for at least two sensor arrays and the need for very accurate positioning of them.

6.2 Numerical phase retrieval

In all of the methods mentioned in the previous section, a numerical reconstruction is necessary to retrieve the actual optical phase distribution. This can, in the case of wavefront shearing interferograms, be made with a phase closure method [87], and in the case of the Shack-Hartmann sensor, with a reconstructor algorithm [88]. When two intensity distributions captured in two significantly different planes are available, as in the phase diversity method, the phase retrieval method of choice is commonly the Gerchberg-Saxton algorithm [89], which has also been used in this work and will therefore be described in some detail here.

The GS algorithm is an iterative process that reconstructs the phase distribution by exploiting a Fourier transform relation between two image planes. In essence, the optical field is numerically propagated from one plane to the other, easily performed with a Fourier transform. This is true to within a multiplicative factor if the approximate Fraunhofer condition is fulfilled, see equation 6.2,

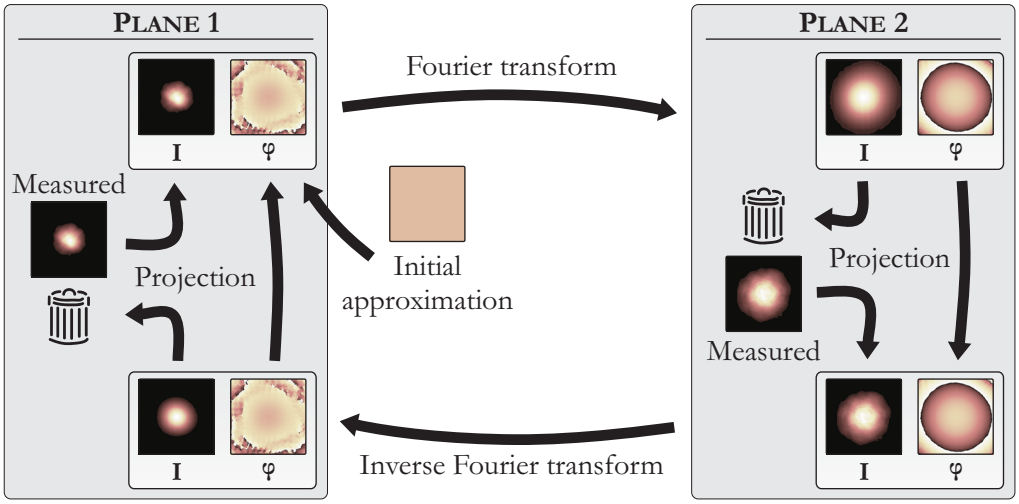

Figure 6.2: Flow chart of the general Gerchberg-Saxton algorithm. The images to the left, marked I, are the intensity distributions and the images to the right, marked φ, are the phase distributions with the initial spherical phase removed.

in which z is the propagation distance and z_R is the Rayleigh range.

$$z \gg z_R = \frac{\pi\,\omega_0^2}{\lambda} \tag{6.2}$$

A flow diagram of the general algorithm is shown in figure 6.2. The process begins with a measured intensity distribution, the square root of which is the amplitude distribution, and an initial phase distribution, which can be entirely random or somehow cleverly estimated. The amplitude and phase distributions are then combined to form an optical field, which is Fourier transformed to simulate the numerical propagation to the other plane. In the next step the simulated amplitude is discarded and replaced by the (square root of the) measured intensity distribution, whereas the simulated phase distribution is retained. This is called a *projection step*, since the measured amplitude is projected onto the simulated result, and is performed to iteratively force the numerical intensity results to be closer to the measured intensity distribution. The optical field is then numerically propagated back to the first plane with an inverse Fourier transform, where another projection step is made, i.e. the propagated amplitude is rejected and replaced by the measured distribution. These process steps are then iterated until the method has converged, so that there is no significant change in the retrieved phase distributions from one iteration to the next. The convergence of the GS algorithm has been proven, in the sense that the error of the algorithm, defined as the sum of the differences in amplitude between the simulated and measured distributions, always decreases or at least remains constant for every iteration [89].

Occasionally, a modification of the amplitude is helpful for obtaining a better match between simulated and measured amplitude distributions, or for

faster convergence of the solution. Usually this is in the form of attenuation at the borders and/or of low amplitude values. For instance, in the original work by Gerchberg and Saxton they found that suppressing the amplitude values that were less than ∼3% of the peak value, resulted in much faster convergence [89].

6.3 Measurement principle of the new method

The idea of this method, which is also presented in paper IV, is to simultaneously image the near- and far-field on a single CCD detector array[a] using the weak reflections from both surfaces of a plano-convex lens, see figure 6.3(a). When the lens is inserted into the laser beam with a minor tilt, it is possible for the two reflections to be captured at two different positions on the CCD detector surface. The reflection from the curved surface of the lens will create an image of the near-field on the CCD, if the distances between the beam waist, the lens, and the CCD are accurately chosen. The field reflected from the flat surface will continue to propagate with the only change being the direction of propagation. Under certain conditions the propagation distance to the CCD camera is such that the far-field is produced, with a size roughly equal to that of the image of the near-field.

In the experiment used to examine this technique, the beam from an OP-SDL was used. The beam waist of this type of laser is not directly accessible, since it is located inside the laser cavity, at the planar gain element. Therefore a spherical double-convex lens was used to create an auxiliary beam waist ($2\omega_0$) outside the cavity, see figure 6.3. The two branches of the setup marked in the figure are the reflections from the planar and curved surfaces of the lens, respectively.

The small detector surface of many CCD cameras sets a boundary condition for the distances between the beam waist, the lens, and the camera, since both the near- and the far-field images must fit within the surface without overlap, and should preferably be roughly equally large ($D_1 \approx D_2$ in figure 6.3(b)) to provide the phase retrieval with as many points of the sampled fields as possible. A further requirement is that the flat surface reflection should propagate a distance considerably longer than the Rayleigh range to ensure that the intensity profile truly is the far-field. It can be shown numerically that all these requirements can be fulfilled simultaneously.

The intensity distributions of the near- and far-field are then used as input to a modified version of the GS phase-retrieval algorithm. Compared to the original GS algorithm, the projection operation used here has been modified to improve convergence by preserving also parts of the simulated amplitude distribution. Further, the simple Fourier transform has been replaced by a numerical simulation of the actual propagation, made possible by the recently

[a]The objective lens of the CCD camera was removed so that the light was incident directly on the CCD detector array

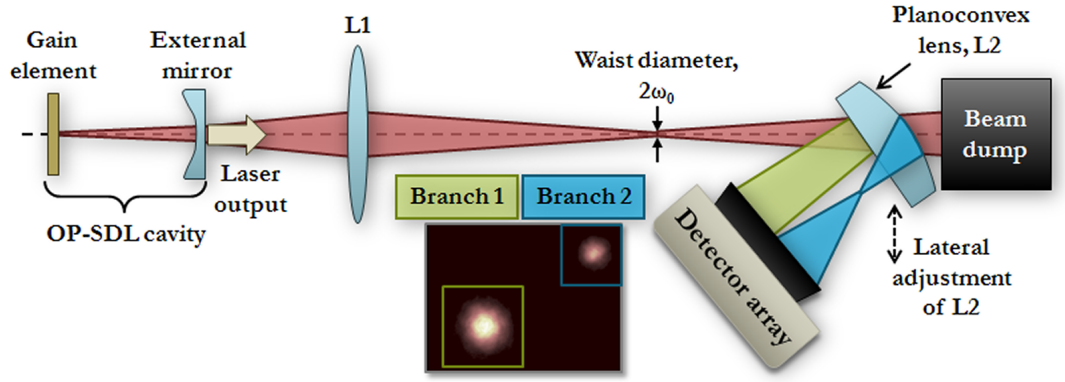

(a) Schematic view of the setup. In this realization, laser light from an OP-SDL was used and a double-convex lens (L1) was used to create an auxiliary beam waist. The essential component, the plano-convex lens (L2), is greatly oversized for clarification. Also shown is an example of the intensity distribution on the camera detector array, with Branch 1 to the lower left and Branch 2 to the upper right.

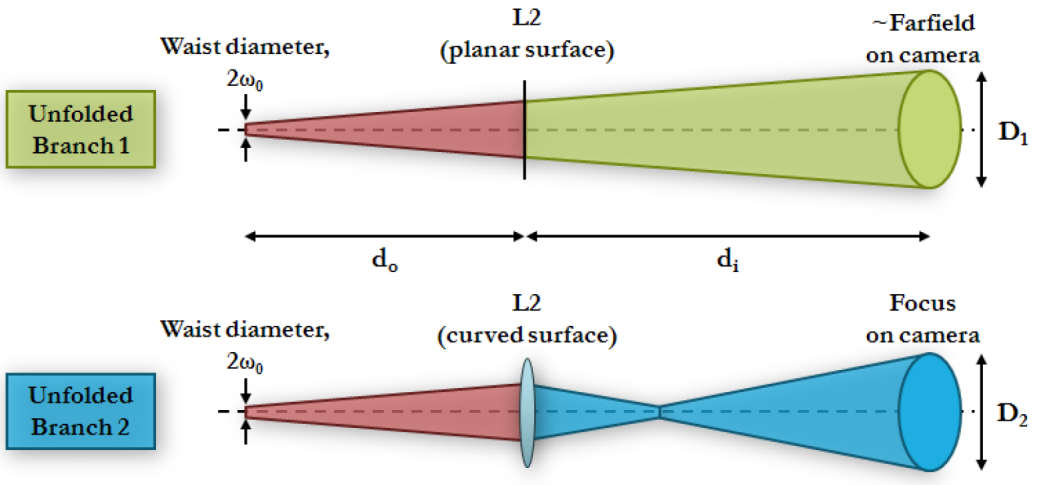

(b) Close-up of the unfolded setup for the reflections from the flat (Branch 1) and curved (Branch 2) surfaces of the plano-convex lens (L2), respectively. Note the formation of an intermediate waist in Branch 2 that is not located in the plane of the camera; this is a consequence of using coherent light for the imaging, see section 6.5.

Figure 6.3: Two views of the setup for the new measurement technique for full beam characterization.

developed two-step method, which does not strictly require that the two fields are a near-far-field pair [90].

6.4 Example application

An advantage of a fully characterized beam is that it is simple to accurately extract any type of beam quality measure. Of particular interest is the M^2 value, which was defined in equation 6.1. Conventionally, the M^2 value is calculated by making measurements of the beam diameter at several positions along the optical axis and from them determining the beam waist and the beam divergence. Unfortunately, it is quite possible for the beam to fluctuate between separate measurements and it can also be difficult to find the exact position of the beam waist. In contrast, the described method fully characterizes a beam in just one momentary measurement, without the need for a precise knowledge of the waist position, after which the beam quality measurements can be performed numerically and more precise, since they are based on a more complete description of the beam.

The numerical beam cuts are performed by simulating the propagation of the characterized optical field through a thin double-convex lens, see figure 6.4(a). At each propagation step the beam diameter is calculated, allowing a precise determination of the beam waist diameter as well as the divergence full-angle, see figure 6.4(b). From this the M^2 value can be calculated, although, stating the M^2 value is of little use without also stating the definition of the width of the beam that was used [91]. Unfortunately, this is seldom done in literature rendering most reported values of beam quality rather irrelevant. In this work I have used the $D_{4\sigma}$ definition of beam width. With this definition, the radius of a beam in the x direction, ω_x, is given by equation 6.3, and likewise in the y direction. The coordinate-pair $(\bar{x}, \bar{y})$ represents the optical axis, and is determined through the center-of-gravity method, as defined by equation 6.4 [92]. With these definitions ω equals the e^{-2} radius for a Gaussian beam.

$$\omega_x^2[z] = 2\,\frac{\int_{-\infty}^{+\infty}\int_{-\infty}^{+\infty} I[x,y,z]\cdot(x-\bar{x})^2\,\mathrm{d}x\mathrm{d}y}{\int_{-\infty}^{+\infty}\int_{-\infty}^{+\infty} I[x,y,z]\,\mathrm{d}x\mathrm{d}y} \tag{6.3}$$

$$\bar{x} = \frac{\int_{-\infty}^{+\infty}\int_{-\infty}^{+\infty} I[x,y,z]\cdot x\,\mathrm{d}x\mathrm{d}y}{\int_{-\infty}^{+\infty}\int_{-\infty}^{+\infty} I[x,y,z]\,\mathrm{d}x\mathrm{d}y} \tag{6.4}$$

Assuming that the captured intensity profiles on the CCD camera are exactly the beam waist image and the far-field, the beam parameters can be estimated directly as a sanity check of the simulated M^2 value. The size of

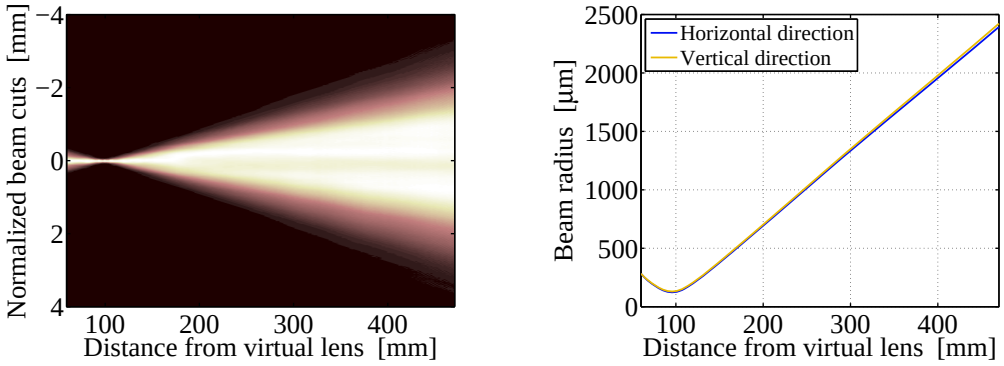

(a) The simulated propagation of the field after insertion of a thin virtual lens.

(b) Calculations of the beam radius in the propagation to the left.

Figure 6.4: An example of a M^2 simulation, where a virtual lens with focal length of 69 mm has been inserted. From the subsequent propagation, shown in (a), several beam cuts are made, shown in (b), to precisely determine the beam waist and divergence.

the beam waist can easily be calculated if the magnification of the imaging system is known. In a similar manner, the beam divergence can be calculated from the image of the far-field, by calculating the size and using trigonometrical relations with the propagated distance from the waist. Thus the M^2 value can be determined in the same way as in the common beam-cut method. In general, though, the image on the CCD camera is not exactly the image of the near-field, so that the M^2 value will be overestimated with this simple method.

6.5 Coherent imaging of an extended source

As a side note, it is interesting to discuss the intermediate waist in Branch 2, visible in figure 6.3(b). According to the Gaussian Lens equation, equation 6.5, the focal length of the curved mirror, f, and the distances between the auxiliary waist and the lens, d_o, and between the lens and the CCD camera, d_i, produces a magnified image of the plane of the auxiliary waist at the image of the CCD camera. Physical intuition would have it that an image of a waist is a waist itself. This is however not always the case, which is evident in figure 6.3(b), which depicts the actual situation during the experiments.

$$\frac{1}{f} = \frac{1}{d_o} + \frac{1}{d_i} \tag{6.5}$$

The reason for this is the combination of an extended source and coherent light. Conventional optics involves either coherent light from a point source or incoherent light from an extended source, and both these cases result in a waist also in the image plane. In figure 6.5 I have compared beam propagation of an extended source (i.e. the beam used in the experiment with a radius of

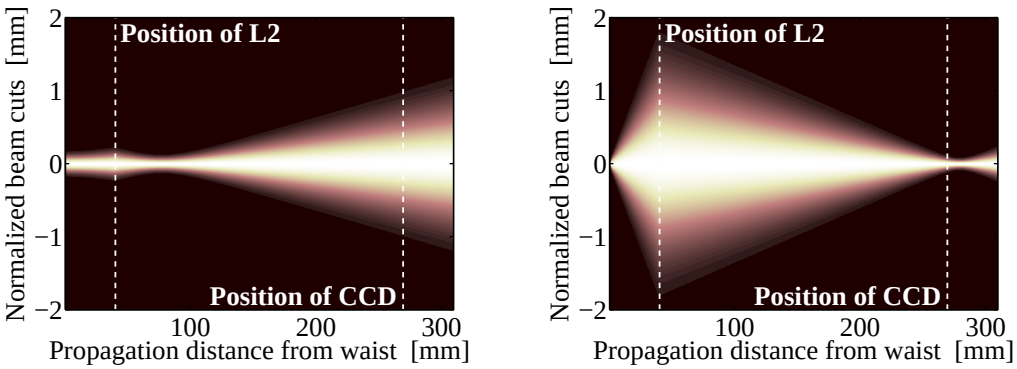

(a) Propagation of a source field with waist radius $\omega_0 = 120$ μm, approximating the experiment beam.

(b) Propagation of a source field with waist radius $\omega_0 = 10$ μm, approximating a point source.

Figure 6.5: Numerical propagation through Branch 2 of an extended source (a) and a point source (b). The case of the point source is consistent with common intuition, but due to the coherence of laser light, an intermediate waist is created in the case of the extended source.

$\omega = 120$ μm) with that of a point source, here realized by a beam of much smaller radius ($\omega = 10$ μm). In the latter case, the waist is located in the image plane, whereas in the former case, the waist is located somewhere in between.

7
Mode-locking

Short light pulses from lasers are useful in communication applications [93], frequency metrology [8], and in high-speed laser machining [94]. Pulsed laser sources today include excimer lasers and solid-state disk lasers, which produce ultra-short pulses with durations measured in femtoseconds (10^{-15} s) [95, 96]. The shortest pulses generated by OP-SDLs have also reached the fs-region and an average power above 1 W has recently been obtained [97]. In this chapter I will briefly describe the theory of generating short pulses with an OP-SDL in section 7.1, which is followed by experimental results in section 7.2.

7.1 Mode-locking theory

The generation of pulses using OP-SDLs is through a process called *passive mode-locking*. In this process, lasing occurs on several longitudinal modes, see section 2.2. Every mode produces its own standing-wave pattern in the cavity, but with nodes and antinodes at slightly different positions due to the small difference in mode frequency, typically a few GHz. If the modes have a certain phase relation, destructive interference between the modes will cancel the fields everywhere except where the wavefronts coincide, where the interference is instead constructive, see figure 7.1. In this case, the laser is said to be mode-locked and the result will be a very intense and narrow pulse propagating back and forth in the laser cavity, see figure 7.2. Obviously, if the modes are not in phase, there will still be constructive and destructive interference, but there will be a random intensity distribution and any number of minor pulses will propagate in the cavity, as in figure 7.3. A commonly used intra-cavity element that makes reliable mode-locking possible is the *semiconductor saturable absorber mirror* (SESAM).

The SESAM is similar to a GE in that it is a semiconductor layer structure with QWs, but the SESAM is much simpler, often just a single QW on top of a DBR. The function of the SESAM is to absorb light that is incident upon it, but only up to a point. When the intensity of the incident pulse exceeds a certain limit — the *saturation fluence*, F_{sat} — the SESAM saturates and

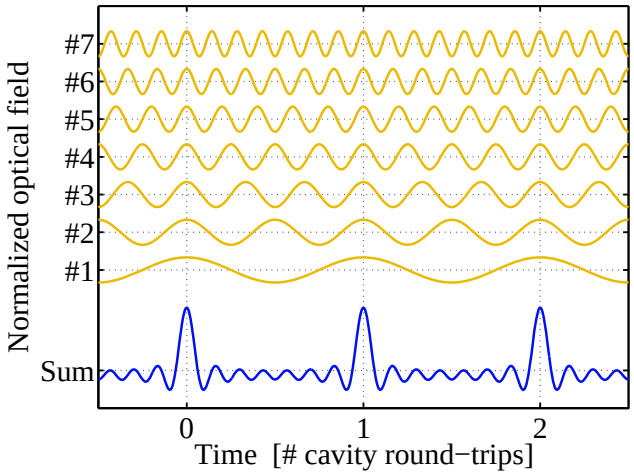

Figure 7.1: The sum of many waves (#1–#7) with slightly different frequencies sum up to a pulse.

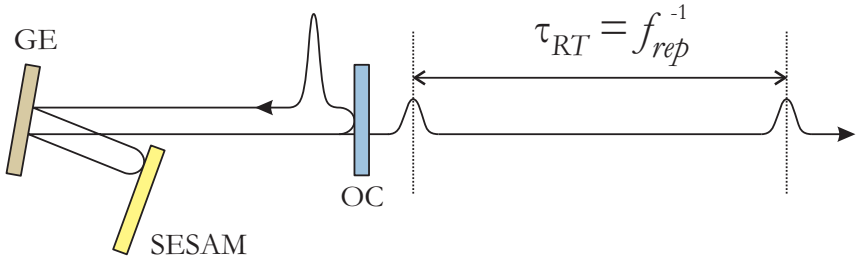

Figure 7.2: The repetition frequency of a passively mode-locked OP-SDL is determined by the cavity round-trip time.

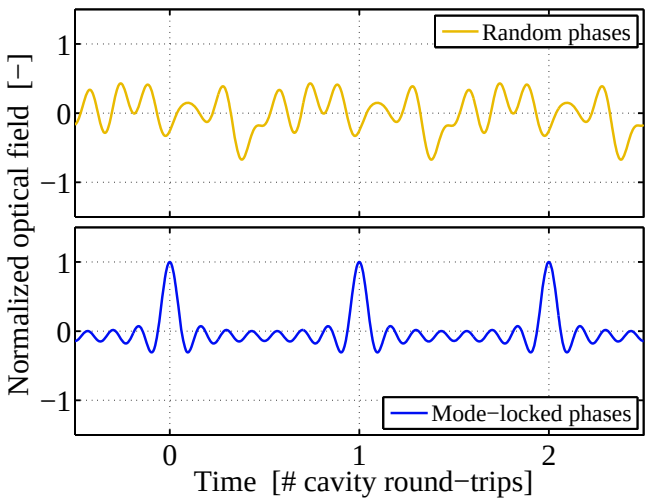

Figure 7.3: Even when many modes are present there will not be a pulse if the modes are not locked in phase. This is shown in the upper figure, while the lower shows the case when the modes are locked in phase.

its absorption drastically decreases until the intensity of the intra-cavity field again drops below F_{sat}. For an incident pulse with a peak intensity that is below F_{sat}, the SESAM absorption is sufficiently large to absorb the entire pulse. The SESAM thus functions as an optical switch that only lets high-intensity pulses pass. Since the modes originate in a random fashion, they are in most cases not in phase and will consequently be absorbed by the SESAM. Only when the modes — by utter chance — happen to be in phase, can the intensity of the resulting pulse reach above F_{sat} and pass the SESAM. Once the mode-locked pulse is set in motion, the modes will continue to be locked and the pulse will continue to propagate in the cavity. Since each time the intra-cavity pulse impinges on the output coupler a fraction of the pulse will be output, the repetition frequency of the pulse train, f_{rep}, is determined by the cavity round trip time, τ_{RT}, see figure 7.2 and equation 7.1, where L_c is the (free-space) cavity length.

$$f_{rep} = \frac{1}{\tau_{RT}} = \frac{c}{2L_c} \tag{7.1}$$

One important property when generating short mode-locked pulses is broadband AMR of the gain element that allows for many modes to overcome the optical losses. Broadband AMR can be achieved using the strategy described in this work, see section 3.2 and paper II, so therefore the type of gain element I developed for wide tunability may also be particularly useful for generating short pulses by mode-locking. Using mode-locking theory, the pulse duration, τ_p, can be approximated by the number of lasing longitudinal modes, M, which in turn is theoretically determined by the wavelength (or frequency) range over which the AMR can exceed the optical losses, B_λ (or B_ν), and the frequency spacing between the modes, ν_F, see equations 7.2.

$$\nu_F = \frac{c}{2L_c} \tag{7.2a}$$

$$M = \frac{B_\nu}{\nu_F} = \frac{B_\lambda\, c/\lambda^2}{\nu_F} \tag{7.2b}$$

$$\tau_p = \frac{1}{B_\nu} \tag{7.2c}$$

As an example, if the bandwidth of net optical gain is $B_\lambda = 45$ nm and the cavity is $L_c = 85$ mm long, the frequency spacing is $\nu_F = 1.8$ GHz, the number of possible modes is $M = 8000$, and the minimum pulse duration is $\tau_p = 70$ fs. This pulse duration is in general much shorter than what is achieved in practice, which means that there is something else limiting the performance.

This other property, which is critically important for the formation of very short pulses, is the *group delay dispersion* (GDD). As its name implies, the GDD describes the dependence of the *group delay* on (angular) frequency. The group delay, T_g, is related to the *group velocity*, v_g, which is the speed of the envelope of a pulse. This is not to be confused with the *phase velocity*, which

is the velocity of a wavefront of a single frequency component. The GDD for a reflective optical component is defined in equation 7.3, where φ is the phase of the reflected wave relative to the incident wave, and ω is the angular oscillation frequency of the optical field.

$$GDD = \frac{\partial^2 \varphi}{\partial \omega^2} \tag{7.3}$$

Since the curvature of the phase reflectivity function φ is in general strongly wavelength dependent for a multilayer semiconductor component, the GDD can vary greatly over the range of operation wavelengths for the gain element and the SESAM.

A non-zero GDD will introduce a phase delay, that will alter the shape of the pulse envelope rendering the mode-locking unstable. Nonetheless, a positive GDD is in fact necessary for a stable mode-locking pulse due to a process called *self-phase modulation* (SPM). SPM is a non-linear phase change that is introduced by the GE and the SESAM due to saturation effects of the gain/absorption. It arises because of a temporal change of the refractive index and is similar to the self-focusing effect, which is a spatial change of the refractive index. The phase change of the GE is positive, but the phase change of the SESAM is negative and has a larger absolute value, resulting in a net negative total phase change. If the intra-cavity components have a positive GDD, this also results in a phase change, which can compensate for the SPM phase change, leading to a stable and soliton-like pulse [98].

However, the interplay between GDD and SPM is sensitive, and too large GDD can severely limit the performance of the OP-SDL. Hoffmann *et al.* showed that a total intra-cavity GDD of 2000–6000 fs^2 produced the shortest pulse durations for their cavity configuration [99]. Since the SESAM alone had a GDD of about 2000 fs^2 (at the operating wavelength), the GDD of the GE should be slightly positive. As shown in figure 7.4, the GDD of the broadband GE described in section 3.2 is negative and varies rapidly near the lasing wavelength (990 nm), where a positive and flat appearance would instead be preferred [100]. A quite simple way to obtain a more desired shape of the GDD curve is to deposit a thin layer of SiO_2 on the top of the GE. The dramatic effect this single layer has on the GDD (and AMR) of the GE can also be seen in the figure.

Looking at figure 7.4 it seems that there is a trade-off between optimizing the AMR spectrum for broadband operation and optimizing the GDD spectrum for short pulse generation. We therefore investigated whether it would be possible to optimize both AMR and GDD spectra simultaneously by modifying the top structure of the gain element, i.e. by keeping the active region and the DBR. In this *layer optimization method* (LOM) the layers were individually optimized and we allowed for up to twenty layers of either pure AlAs or Al(20%)Ga(80%)As, with almost arbitrary thickness, in the top structure and possibly a dielectric coating on top. To determine which of the two tested

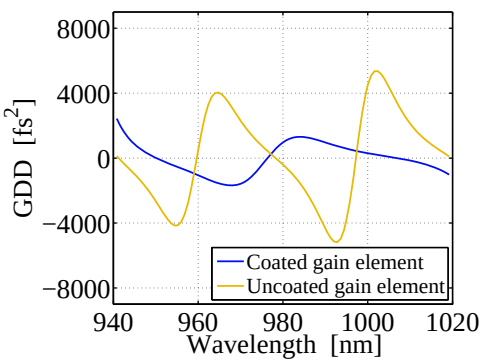

(a) The GDD of the broadband GE from section 3.2 with and without a dielectric coating.

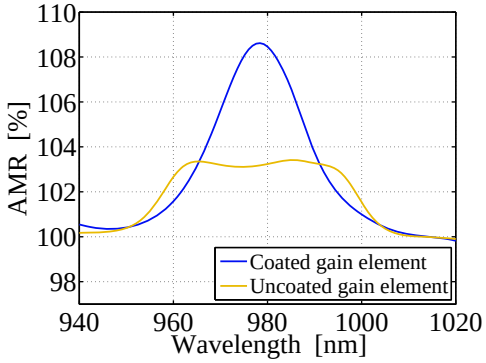

(b) The AMR of the broadband GE with and without a dielectric coating.

Figure 7.4: Illustrations of the dramatic effect of a single dielectric coating on a gain element. The GDD of the coated GE is considerably closer to the desired shape, i.e. flat and slightly positive for lasing wavelengths in the vicinity of 990 nm.

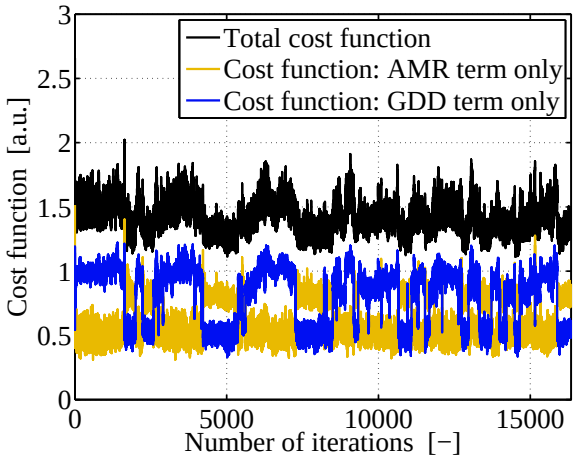

Figure 7.5: Evolution of the cost function of the LOM algorithm when optimizing both AMR and GDD spectra. The total cost function remains fairly constant, while the individual AMR and GDD terms alternate between good and bad values.

material compositions and thicknesses for a certain layer are optimal, a cost function was defined. The generic cost function, C, we used was a mean-square deviation from the desired, prescribed, reflectance and GDD spectra, see equation 7.4, where m and n numbers the wavelength values for which the target values for the reflectance, AMR_t, and GDD, GDD_t, respectively, are specified. The prefactor W was used to determine the importance of the GDD targets compared to the reflectivity targets; if only the AMR is of interest W was set to zero, if only the GDD should be optimized W was set to a very large number.

$$C = \sum_n \Big(AMR\left[\lambda_n\right] - AMR_t\left[\lambda_n\right] \Big)^2 + W \cdot \sum_m \Big(GDD\left[\lambda_m\right] - GDD_t\left[\lambda_m\right] \Big)^2 \tag{7.4}$$

For the simultaneous optimization of both the AMR and GDD spectra, the weight W was chosen by some quick tests to ensure that both terms in the cost function were of roughly the same magnitude. Then extensive design runs were performed, including slight changes in the value for W as well as tests of alternative cost functions. However, all these tests pointed to the same result, since the evolution of the LOM algorithm always had the qualitative appearance as depicted in figure 7.5: a distinct "anti-correlation" between the AMR term and the GDD term in the cost function. Almost invariably, as a top structure design with a better AMR performance is found, its GDD performance gets worse, and vice versa. Thus we may draw the conclusion, that although LOM proved to be very good at finding good top structures for either a desired AMR or GDD spectrum, it seems that prescribing both spectra is not possible, maybe because the design freedom is too limited when only considering the top structure. It would of course be theoretically possible to design the entire OP-SDL structure with LOM, but it would be a much more demanding computational task, not only in terms of the number of layers, but also to get a good number and positioning of the QWs, barriers, and strain compensating layers.

7.2 Experimental results

To verify the emission of mode-locked pulses, three measurements should be performed:

1) An auto-correlation (AC) trace. This is the pulse in the time domain and can be visualized with an auto-correlator and an oscilloscope. The pulse duration, τ_p, is the FWHM of the pulse trace, which should be sech^2- or Gaussian-shaped and have a lower level of (almost) zero. If the pulse trace shows up on a plateau, there is most probably mode beating in the cavity, i.e. several longitudinal modes interfering without being locked in phase.

2) An optical spectrum. The width of the optical spectrum, $\Delta\lambda$, is measured with an optical spectrum analyzer and gives information on how many resonator modes that contribute to the pulse generation.

3) A radio-frequency (RF) spectrum. Using a high-speed detector and a microwave signal analyzer, the RF spectrum shows the repetition rate of the pulse train, f_{rep}. The side-mode suppression should be at least 30 dB.

Together with collaborators at ETH Zürich in Switzerland, mode-locking experiments were performed on uncoated broadband GEs, the results of which can be seen in figure 7.6. The cavity was V-shaped with the GE in the folding point, see figure 7.7. An etalon was inserted in the cavity to tune the lasing wavelength to 987 nm, to better match the design wavelength of the SESAM, 960 nm. The pulse duration was $\tau_p = 3.8$ ps and the width of the optical spectrum was $\Delta\lambda = 0.36$ nm. The average power of the pulses was $P_{avg} = 100$ mW and the repetition frequency was $f_{rep} = 0.93$ GHz, corresponding to a peak power of $P_{peak} = 25$ W according to equation 7.5, in which a sech^2-shape was assumed.

$$P_{peak} = 0.88\frac{P_{avg}}{f_{rep}\tau_p} \tag{7.5}$$

As a measure of the quality of a pulse, the *time-bandwidth product* ($TBP = \tau_p\Delta\nu$) is often used, which is the product of the pulse widths in the time and frequency domains. The importance of the TBP stems from the fact that for a certain width of the optical spectrum, there is a minimum pulse duration. Basically, the shape in the time domain of the perfect chirp-free pulse should be the Fourier transform of its optical spectrum, and the pulse is then said to be *transform-limited*. If the pulse is not perfect, the duration of the pulse will be longer and the TBP larger. Due to the nature of the Fourier transform, there is a minimum TBP that is constant for all spectral widths, but varies with pulse shape. For instance, the transform-limited TBP for sech^2-shaped pulses is $\sim$0.315 and for Gaussian-shaped pulses $\sim$0.440. Because of this absolute value, all pulses of the same shape can be compared to each other using the TBP. Usually, the absolute TBP is stated along with the TBP relative to the minimum TBP for the assumed pulse shape. For the pulse shown in figure 7.6, the TBP was 0.428, which is 1.36 times the minimum TBP for sech^2-shaped pulses.

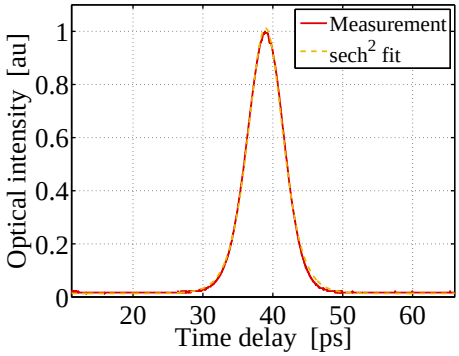

(a) Auto-correlation trace showing the pulse duration, $\tau_p = 3.8$ ps.

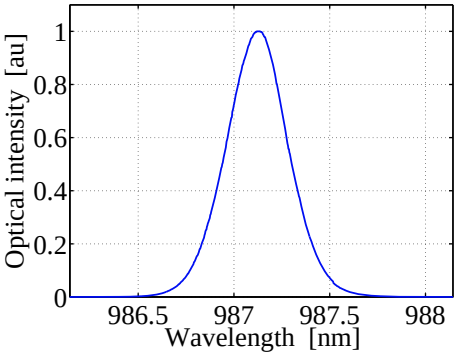

(b) Optical spectrum of pulse with a FWHM bandwidth of $\Delta\lambda = 0.363$ nm.

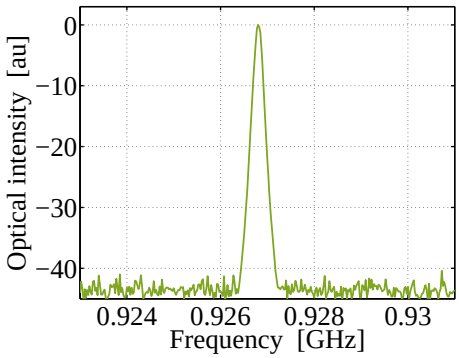

(c) Radio-frequency spectrum showing the repetition frequency, $f_{rep} = 927$ MHz, and a side-mode suppression of 40 dB.

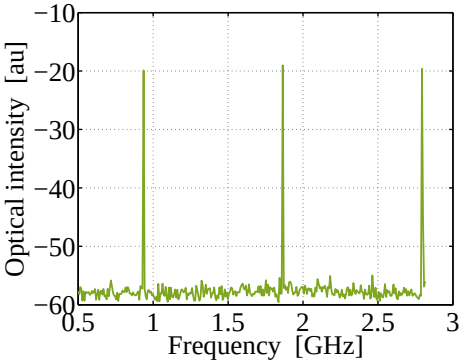

(d) A zoom-out of the RF spectrum, showing the overtones of f_{rep}.

Figure 7.6: Results from mode-locking experiments with an average output power $P_{avg} = 100$ mW, corresponding to a peak power $P_{peak} = 25$ W assuming a sech^2-shaped pulse.

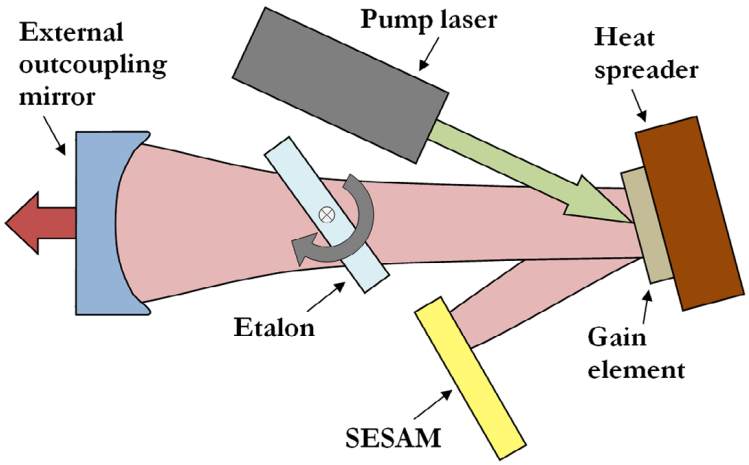

Figure 7.7: Schematic view of the cavity configuration during the mode-locking experiments. The unfolded cavity length was 16 cm with an out-coupling mirror radius of curvature of 200 mm.

8

Summary of papers

To this thesis four papers published in scientific journals have been appended.

Paper I

C. Borgentun, J. Bengtsson, and A. Larsson, "Direct measurement of the spectral reflectance of OP-SDL gain elements under optical pumping," *Optics Express*, vol. 19, no. 18, pp. 16890–16897, August 2011

This paper presents a new method for directly measuring the *active mirror reflectance* (AMR), i.e. the reflectance of an optically pumped gain element. The method can be viewed as an extension of the commonly-used reflectance spectrum measurement, but provides significantly more information on the complete design of the gain element. The principle of the method is to let the spot from a tunable laser source, acting as a probe, overlap on the gain element surface with the spot from a pump laser. The incident and reflected powers of the tunable probe beam are measured as the wavelength is swept over the wavelength range of interest. By comparing the incident and reflected powers, and calibrating for dispersion with a known reflectance standard, the AMR can be calculated.

The method was evaluated using two differently designed gain elements, the AMR spectra of which were also calculated using numerical simulations. The agreement between measurements and simulations were striking, proving the high accuracy of the measurement method as well as the validity of the physical models used in the numerical work.

My contributions: In this work I developed the measurement technique, implemented the setup, performed all measurements, evaluated the data, and wrote the article.

Paper II

C. Borgentun, J. Bengtsson, A. Larsson, F. Demaria, A. Hein, and P. Unger, "Optimization of a broadband gain element for a widely tunable high-power semiconductor disk laser," *IEEE Photonics Technology Letters*, vol. 22, no. 13, pp. 978–980, July 2010

In this paper we present the design strategy for wide tunability of OP-SDLs described in section 3.2, and how this is successfully implemented for the epitaxial structure of a gain element working in the 960–1000 nm wavelength range. The simulated AMR of a gain element optimized for this wide tunability is shown as well as results from threshold measurements. These strongly imply that the gain element is suitable for wide tuning, which is subsequently proved by showing results from CW tuning experiments. A tuning range of 43 nm was achieved with a maximum output power of 2.6 W.

My contributions: I developed the computer models for designing and optimizing the gain element, fabricated the gain elements, performed all measurements, and wrote the paper.

Paper III

C. Borgentun, C. Hessenius, J. Bengtsson, M. Fallahi, and A. Larsson, "Widely-tunable high-power semiconductor disk laser with non-resonant AR-assisted gain element on diamond heat spreader," *IEEE Photonics Journal*, vol. 3, no. 5, pp. 946–953, 2011

This paper presents results regarding improved heat management of the OP-SDL gain element. A study involving comparisons between using copper or diamond as heat spreader material was performed numerically and experimentally. The thermal impedance was reduced by a factor 2–3 when using CVD diamond as the heat spreader. This lead to a large increase in output power of the OP-SDL, and the CW tuning experiments resulted in a 32 nm tuning range with 7.5 W peak output power.

My contributions: I performed all measurements regarding heat management and wrote the paper.

Paper IV

C. Borgentun, J. Bengtsson, and A. Larsson, "Full characterization of a high-power semiconductor disk laser beam with simultaneous capture of optimally sized focus and farfield," *Applied Optics*, vol. 50, no. 12, pp. 1640–1649, 2011

Paper IV describes a new and simple measurement technique for determining both the phase distribution and the intensity distribution of a laser beam in a plane normal to the optical axis. With this, the laser beam is fully characterized and all parameters necessary to determine the propagation of the beam are known. Thus, after the measurement a numerical simulation can be performed to investigate e.g. whether the wavefront astigmatism is sufficiently small for the intended application, or to calculate the M^2 value, which is a common measure of the beam quality.

The principle of the characterization method is to capture the intensity distributions of the near- and far-field of the beam and subsequently retrieve the phase distribution using a numerical algorithm. The capture is made using reflections from both sides of a plano-convex lens, making the capture simultaneous, thus suitable also for fluctuating beams, and possible to perform with a single CCD device. Several examples are shown in the article together with results from M^2 calculations.

My contributions: I co-developed the measurement technique, implemented the setup, performed all measurements, took part in the numerical simulations, and co-wrote the paper.

References

[1] T. H. Maiman, "Stimulated optical radiation in ruby," *Nature*, vol. 187, pp. 493–494, Aug. 1960.

[2] R. J. Collins, D. F. Nelson, A. L. Schawlow, W. Bond, C. G. B. Garrett, and W. Kaiser, "Coherence, narrowing, directionality, and relaxation oscillations in the light emission from ruby," *Physical Review Letters*, vol. 5, pp. 303–305, Oct. 1960.

[3] P. P. Sorokin and M. J. Stevenson, "Stimulated infrared emission from trivalent uranium," *Physical Review Letters*, vol. 5, pp. 557–559, Dec. 1960.

[4] I. Wieder and L. R. Sarles, "Stimulated optical emission from exchange-coupled ions of Cr^{+++} in Al_2O_3," *Physical Review Letters*, vol. 6, pp. 95–96, Feb. 1961.

[5] A. Javan, J. Bennett, W. R., and D. R. Herriott, "Population inversion and continuous optical maser oscillation in a gas discharge containing a He–Ne mixture," *Physical Review Letters*, vol. 6, pp. 106–110, Feb. 1961.

[6] P. P. Sorokin and M. J. Stevenson, "Solid-state optical maser using divalent samarium in calcium fluoride," *IBM Journal of Research and Development*, vol. 5, no. 1, pp. 56–58, 1961.

[7] F. Fankhauser, U. Dürr, H. Giger, P. Rol, and S. Kwasniewska, "Lasers, optical systems and safety in ophthalmology: a review," *Graefe's Archive for Clinical and Experimental Ophthalmology*, vol. 234, pp. 473–487, Aug. 1996.

[8] T. Udem, R. Holzwarth, and T. W. Hänsch, "Optical frequency metrology," *Nature*, vol. 416, pp. 233–237, Mar. 2002.

[9] K. V. Chellappan, E. Erden, and H. Urey, "Laser-based displays: a review," *Applied Optics*, vol. 49, pp. F79–F98, Sept. 2010.

[10] E. S. Rothchild, "Optical memory: Data storage by laser," *Byte Magazine*, vol. 9, pp. 215–224, Oct. 1984.

[11] Z. Tong, C. Lundström, P. A. Andrekson, C. J. McKinstrie, M. Karlsson, D. J. Blessing, E. Tipsuwannakul, B. J. Puttnam, H. Toda, and L. Grüner-Nielsen, "Towards ultrasensitive optical links enabled by low-noise phase-sensitive amplifiers," *Nature Photonics*, vol. 5, pp. 430–436, July 2011.

[12] A. Larsson, "Advances in VCSELs for communication and sensing," *IEEE Journal of Selected Topics in Quantum Electronics*, vol. 17, pp. 1552–1567, Nov. 2011.

[13] E. Hällstig, J. Öhgren, L. Allard, L. Sjöqvist, D. Engström, S. Hård, D. Ågren, S. Junique, Q. Wang, and B. Noharet, "Retrocommunication utilizing electroabsorption modulators and nonmechanical beam steering," *Optical Engineering*, vol. 44, pp. 045001–8, Apr. 2005.

[14] R. N. Schwartz and C. H. Townes, "Interstellar and interplanetary communication by optical masers," *Nature*, vol. 190, pp. 205–208, Apr. 1961.

[15] B. Turner and M. Lades, "KC space pirates and NASA's power beaming challenge," in *Proc. SPIE*, vol. 7581, (San Francisco, CA, USA), pp. 75810P–11, SPIE, Feb. 2010.

[16] R. N. Hall, G. E. Fenner, J. D. Kingsley, T. J. Soltys, and R. O. Carlson, "Coherent light emission from GaAs junctions," *Physical Review Letters*, vol. 9, pp. 366–368, Nov. 1962.

[17] A. von Pfeil and T. von Freyhold, "Beam shaping of broad-area diode lasers: principles and benefits," in *Proc. SPIE*, vol. 4648, (San Jose, CA, USA), pp. 82–90, SPIE, Apr. 2002.

[18] J. Sandusky and S. Brueck, "A CW external-cavity surface-emitting laser," *IEEE Photonics Technology Letters*, vol. 8, pp. 313–315, Mar. 1996.

[19] M. Kuznetsov, F. Hakimi, R. Sprague, and A. Mooradian, "High-power (>0.5-W CW) diode-pumped vertical-external-cavity surface-emitting semiconductor lasers with circular TEM_{00} beams," *IEEE Photonics Technology Letters*, vol. 9, no. 8, pp. 1063–1065, 1997.

[20] T.-L. Wang, Y. Kaneda, J. M. Yarborough, J. Hader, J. V. Moloney, A. Chernikov, S. Chatterjee, S. W. Koch, B. Kunert, and W. Stolz, "High-power optically pumped semiconductor laser at 1040 nm," *IEEE Photonics Technology Letters*, vol. 22, pp. 661–663, May 2010.

[21] B. Rudin, A. Rutz, M. Hoffmann, D. J. H. C. Maas, A.-R. Bellancourt, E. Gini, T. Südmeyer, and U. Keller, "Highly efficient optically pumped

vertical-emitting semiconductor laser with more than 20 W average output power in a fundamental transverse mode," *Optics Letters*, vol. 33, pp. 2719–2721, Nov. 2008.

[22] F. Demaria, S. Lorch, S. Menzel, M. Riedl, F. Rinaldi, R. Rösch, and P. Unger, "Design of highly efficient high-power optically pumped semiconductor disk lasers," *IEEE Journal of Selected Topics in Quantum Electronics*, vol. 15, no. 3, pp. 973–977, 2009.

[23] T. D. Raymond, W. J. Alford, M. H. Crawford, and A. A. Allerman, "Intracavity frequency doubling of a diode-pumped external-cavity surface-emitting semiconductor laser," *Optics Letters*, vol. 24, pp. 1127–1129, Aug. 1999.

[24] R. Häring, R. Paschotta, A. Aschwanden, E. Gini, F. Morier-Genoud, and U. Keller, "High-power passively mode-locked semiconductor lasers," *IEEE Journal of Quantum Electronics*, vol. 38, pp. 1268–1275, Sept. 2002.

[25] M. Holm, D. Burns, A. Ferguson, and M. Dawson, "Actively stabilized single-frequency vertical-external-cavity AlGaAs laser," *IEEE Photonics Technology Letters*, vol. 11, no. 12, pp. 1551–1553, 1999.

[26] J. Colegrove, "Pocket projector technology and market forecast report." Display Search, January 2012.

[27] R. Köhler, A. Tredicucci, F. Beltram, H. E. Beere, E. H. Linfield, A. G. Davies, D. A. Ritchie, R. C. Iotti, and F. Rossi, "Terahertz semiconductor-heterostructure laser," *Nature*, vol. 417, pp. 156–159, May 2002.

[28] C. Kannengiesser, V. Ostroumov, V. Pfeufer, W. Seelert, C. Simon, R. von Elm, and A. Zuck, "Ten years optically pumped semiconductor lasers: review, state-of-the-art, and future developments," in *Proc. SPIE*, vol. 7578, (San Francisco, CA, USA), pp. 75780W–11, SPIE, Feb. 2010.

[29] H. Bunk, A. Lepert, and P. Vogt, "Something OPSL, something new." Photonics Spectra, Oct. 2011.

[30] J. Chilla, E. Rea, M. Gitin, and D. Nash, "High-power 980-nm pumps for high-power amplifiers," *Lightwave*, vol. 19, pp. 78–85, Mar. 2002.

[31] V. Baev, T. Latz, and P. Toschek, "Laser intracavity absorption spectroscopy," *Applied Physics B: Lasers and Optics*, vol. 69, pp. 171–202, Sept. 1999.

[32] A. Garnache, A. A. Kachanov, F. Stoeckel, and R. Planel, "High-sensitivity intracavity laser absorption spectroscopy with vertical-external-cavity surface-emitting semiconductor lasers," *Optics Letters*, vol. 24, pp. 826–828, June 1999.

[33] A. Garnache, A. A. Kachanov, F. Stoeckel, and R. Houdré, "Diode-pumped broadband vertical-external-cavity surface-emitting semiconductor laser applied to high-sensitivity intracavity absorption spectroscopy," *Journal of the Optical Society of America B: Optical Physics*, vol. 17, pp. 1589–1598, Sept. 2000.

[34] J. Paajaste, S. Suomalainen, R. Koskinen, A. Härkönen, M. Guina, and M. Pessa, "High-power and broadly tunable GaSb-based optically pumped VECSELs emitting near 2 μm," *Journal of Crystal Growth*, vol. 311, pp. 1917–1919, Mar. 2009.

[35] L. Fan, M. Fallahi, A. Zakharian, J. Hader, J. Moloney, R. Bedford, J. Murray, W. Stolz, and S. Koch, "Extended tunability in a two-chip VECSEL," *IEEE Photonics Technology Letters*, vol. 19, pp. 544–546, Apr. 2007.

[36] H. Kogelnik and T. Li, "Laser beams and resonators," *Applied Optics*, vol. 5, pp. 1550–1567, Oct. 1966.

[37] L. Coldren, G. Fish, Y. Akulova, J. Barton, L. Johansson, and C. Coldren, "Tunable semiconductor lasers: A tutorial," *Journal of Lightwave Technology*, vol. 22, no. 1, pp. 193–202, 2004.

[38] K. Kobayashi and I. Mito, "Single frequency and tunable laser diodes," *Journal of Lightwave Technology*, vol. 6, no. 11, pp. 1623–1633, 1988.

[39] N. Yokouchi, T. Miyamoto, T. Uchida, Y. Inaba, F. Koyama, and K. Iga, "40 Å continuous tuning of a GaInAsP/InP vertical-cavity surface-emitting laser using an external mirror," *IEEE Photonics Technology Letters*, vol. 4, no. 7, pp. 701–703, 1992.

[40] B. Kögel, M. Maute, H. Halbritter, F. Riemenschneider, G. Böhm, M.-C. Amann, and P. Meissner, "Long-wavelength MEMS tunable vertical-cavity surface-emitting lasers with high sidemode suppression," *Journal of Optics A: Pure and Applied Optics*, vol. 8, no. 7, pp. S370–S376, 2006.

[41] C. Chang-Hasnain, J. Harbison, C.-E. Zah, M. Maeda, L. Florez, N. Stoffel, and T.-P. Lee, "Multiple wavelength tunable surface-emitting laser arrays," *IEEE Journal of Quantum Electronics*, vol. 27, no. 6, pp. 1368–1376, 1991.

[42] Y. Tohmori, Y. Suematsu, H. Tsushima, and S. Arai, "Wavelength tuning of GaInAsP/InP integrated laser with butt-jointed built-in distributed Bragg reflector," *Electronics Letters*, vol. 19, no. 17, pp. 656–657, 1983.

[43] R. Ludeke and E. P. Harris, "Tunable GaAs laser in an external dispersive cavity," *Applied Physics Letters*, vol. 20, pp. 499–500, June 1972.

[44] D. J. Bradley, G. M. Gale, M. Moore, and P. D. Smith, "Longitudinally pumped, narrow-band continuously tunable dye laser," *Physics Letters A*, vol. 26, pp. 378–379, Mar. 1968.

[45] E. D. Hinkley, T. C. Harman, and C. Freed, "Optical heterodyne detection at 10.6 μm of the beat frequency between a tunable $Pb_{0.88}Sn_{0.12}Te$ diode laser and a CO_2 gas laser," *Applied Physics Letters*, vol. 13, pp. 49–51, July 1968.

[46] G. T. Schappert, K. W. Billman, and D. C. Burnham, "Temperature tuning of an organic dye laser," *Applied Physics Letters*, vol. 13, pp. 124–126, Aug. 1968.

[47] A. L. Bloom, "Modes of a laser resonator containing tilted birefringent plates," *Journal of Optical Society of America*, vol. 64, pp. 447–452, Apr. 1974.

[48] F. Ortwein, J. Mentel, and E. Schmidt, "A birefringent filter as a tuning element for a multiline He–Se^+ laser," *Journal of Physics D: Applied Physics*, vol. 22, no. 4, pp. 488–491, 1989.

[49] C. Borgentun, J. Bengtsson, and A. Larsson, "Direct measurement of the spectral reflectance of OP-SDL gain elements under optical pumping," *Optics Express*, vol. 19, pp. 16890–16897, Aug. 2011.

[50] M. A. Afromowitz, "Refractive index of $Ga_{1-x}Al_xAs$," *Solid State Communications*, vol. 15, pp. 59–63, July 1974.

[51] S. Adachi, "Refractive indices of III–V compounds: Key properties of InGaAsP relevant to device design," *Journal of Applied Physics*, vol. 53, pp. 5863–5869, Aug. 1982.

[52] E. Yablonovitch and E. Kane, "Reduction of lasing threshold current density by the lowering of valence band effective mass," *Journal of Lightwave Technology*, vol. 4, no. 5, pp. 504–506, 1986.

[53] A. Adams, "Band-structure engineering for low-threshold high-efficiency semiconductor lasers," *Electronics Letters*, vol. 22, no. 5, pp. 249–250, 1986.

[54] L. Coldren and S. Corzine, *Diode lasers and photonic integrated circuits*. Wiley, New York, 1995.

[55] J. Leymarie, P. Disseix, M. Rezki, C. Monier, A. Vasson, and A. M. Vasson, "Conduction band offset ratio of the (In,Ga)As/GaAs system and (In,Ga)As alloy properties," *Materials Science and Engineering B*, vol. 44, pp. 147–150, Feb. 1997.

[56] J. Hader, J. Moloney, and S. Koch, "Microscopic theory of gain, absorption, and refractive index in semiconductor laser materials — Influence of conduction-band nonparabolicity and Coulomb-induced intersubband coupling," *IEEE Journal of Quantum Electronics*, vol. 35, no. 12, pp. 1878–1886, 1999.

[57] C. Bückers, E. Kühn, C. Schlichenmaier, S. Imhof, A. Thränhardt, J. Hader, J. V. Moloney, O. Rubel, W. Zhang, T. Ackemann, and S. W. Koch, "Quantum modeling of semiconductor gain materials and vertical-external-cavity surface-emitting laser systems," *physica status solidi (b)*, vol. 247, no. 4, pp. 789–808, 2010.

[58] H. C. Casey Jr. and M. B. Panish, *Heterostructure Lasers*. Academic, New York, 1978.

[59] J. Feldmann, G. Peter, E. O. Göbel, P. Dawson, K. Moore, C. Foxon, and R. J. Elliott, "Linewidth dependence of radiative exciton lifetimes in quantum wells," *Physical Review Letters*, vol. 59, pp. 2337–2340, Nov. 1987.

[60] D. Chemla, D. Miller, P. Smith, A. Gossard, and W. Wiegmann, "Room temperature excitonic nonlinear absorption and refraction in GaAs/AlGaAs multiple quantum well structures," *IEEE Journal of Quantum Electronics*, vol. 20, no. 3, pp. 265–275, 1984.

[61] I. Vurgaftman, J. R. Meyer, and L. R. Ram-Mohan, "Band parameters for III–V compound semiconductors and their alloys," *Journal of Applied Physics*, vol. 89, pp. 5815–5875, June 2001.

[62] S. Adachi, "GaAs, AlAs, and $Al_xGa_{1-x}As$: Material parameters for use in research and device applications," *Journal of Applied Physics*, vol. 58, pp. R1–R29, Aug. 1985.

[63] S. Adachi, "Material parameters of $In_{1-x}Ga_xAs_yP_{1-y}$ and related binaries," *Journal of Applied Physics*, vol. 53, pp. 8775–8792, Dec. 1982.

[64] E. D. Jones, S. K. Lyo, I. J. Fritz, J. F. Klem, J. E. Schirber, C. P. Tigges, and T. J. Drummond, "Determination of energy-band dispersion curves in strained-layer structures," *Applied Physics Letters*, vol. 54, pp. 2227–2229, May 1989.

[65] P. Y. Yu and M. Cardona, *Fundamentals of Semiconductors: Physics and Materials Properties*. Springer-Verlag, Heidelberg, Berlin, 3rd ed., 2005.

[66] T. Amand, X. Marie, B. Dareys, J. Barrau, M. Brousseau, D. J. Dunstan, J. Y. Emery, and L. Goldstein, "Well-width dependence of the excitonic lifetime in strained III-V quantum wells," *Journal of Applied Physics*, vol. 72, pp. 2077–2079, Sept. 1992.

[67] L. Chen, K. Rajkumar, A. Madhukar, W. Chen, S. Guha, and K. Kaviani, "Realization of sharp excitonic features in highly strained GaAs/$In_xGa_{1-x}As$ multiple quantum wells grown on GaAs(100) substrates," *Journal of Crystal Growth*, vol. 111, pp. 424–428, May 1991.

[68] Y. Hirayama, W.-Y. Choi, L. H. Peng, and C. G. Fonstad, "Absorption spectroscopy on room temperature excitonic transitions in strained layer InGaAs/InGaAlAs multiquantum-well structures," *Journal of Applied Physics*, vol. 74, pp. 570–578, July 1993.

[69] R. Wilson, *Fatilary calculus*. PhD thesis, Chalmers University of Technology, 1956.

[70] J. Piprek, *Semiconductor optoelectronic devices*. Academic Press, 2003.

[71] J. Geske, K.-G. Gan, Y. Okuno, J. Piprek, and J. Bowers, "Vertical-cavity surface-emitting laser active regions for enhanced performance with optical pumping," *IEEE Journal of Quantum Electronics*, vol. 40, pp. 1155–1162, Sept. 2004.

[72] A. Clawson, "Guide to references on III–V semiconductor chemical etching," *Materials Science and Engineering: R: Reports*, vol. 31, pp. 1–438, Jan. 2001.

[73] Y. Uenishi, H. Tanaka, and H. Ukita, "Characterization of AlGaAs microstructure fabricated by AlGaAs/GaAs micromachining," *IEEE Transactions on Electron Devices*, vol. 41, no. 10, pp. 1778–1783, 1994.

[74] J. J. LePore, "An improved technique for selective etching of GaAs and $Ga_{1-x}Al_xAs$," *Journal of Applied Physics*, vol. 51, pp. 6441–6442, Dec. 1980.

[75] P. D. Moran, D. M. Hansen, R. J. Matyi, J. M. Redwing, and T. F. Kuech, "Realization and characterization of ultrathin GaAs-on-insulator structures," *Journal of the Electrochemical Society*, vol. 146, pp. 3506–3509, Sept. 1999.

[76] J.-H. Kim, D. H. Lim, and G. M. Yang, "Selective etching of AlGaAs/GaAs structures using the solutions of citric acid/H_2O_2 and deionized H_2O/buffered oxide etch," *Journal of Vacuum Science and Technology B*, vol. 16, pp. 558–560, Mar. 1998.

[77] K. Pierscinski, D. Pierscinska, M. Bugajski, C. Manz, and M. Rattunde, "Investigation of thermal management in optically pumped, antimonide VECSELs," *Microelectronics Journal*, vol. 40, pp. 558–561, Mar. 2009.

[78] Z. L. Liau, "Semiconductor wafer bonding via liquid capillarity," *Applied Physics Letters*, vol. 77, pp. 651–653, July 2000.

[79] V.-M. Korpijärvi, T. Leinonen, J. Puustinen, A. Härkönen, and M. D. Guina, "11 W single gain-chip dilute nitride disk laser emitting around 1180 nm," *Optics Express*, vol. 18, pp. 25633–25641, Dec. 2010.

[80] M. Butkus, J. Rautiainen, O. G. Okhotnikov, C. J. Hamilton, G. G. Malcolm, S. S. Mikhrin, I. L. Krestnikov, D. D. Livshits, and E. U. Rafailov, "Quantum dot based semiconductor disk lasers for 1–1.3 μm," *IEEE Journal of Selected Topics in Quantum Electronics*, vol. 17, pp. 1763–1771, Nov. 2011.

[81] B. E. A. Saleh and M. C. Teich, *Fundamentals of photonics*. Wiley, USA, 2nd ed., 2007.

[82] T. Johnston Jr., "Beam propagation (M^2) measurement made as easy as it gets: The four-cuts method," *Applied Optics*, vol. 37, no. 21, pp. 4840–4850, 1998.

[83] W. J. Bates, "A wavefront shearing interferometer," *Proceedings of the Physical Society*, vol. 59, pp. 940–952, Nov. 1947.

[84] R. V. Shack and B. C. Platt, "Production and use of a lenticular Hartmann screen," *Journal of the Optical Society of America*, vol. 61, no. 5, p. 656, 1971.

[85] R. Ng, *Digital light field photography*. PhD thesis, Stanford University, July 2006.

[86] R. A. Gonsalves, "Phase retrieval and diversity in adaptive optics," *Optical Engineering*, vol. 21, pp. 829–832, 1982.

[87] F. Roddier and C. Roddier, "Phase closure with rotational shear interferometers," *Optics Communications*, vol. 60, pp. 350–352, Dec. 1986.

[88] R. H. Hudgin, "Wave-front reconstruction for compensated imaging," *Journal of the Optical Society of America*, vol. 67, pp. 375–378, Mar. 1977.

[89] R. Gerchberg and W. Saxton, "Practical algorithm for the determination of phase from image and diffraction plane pictures," *Optik (Stuttgart)*, vol. 35, no. 2, pp. 237–250, 1972.

[90] C. Rydberg and J. Bengtsson, "Efficient numerical representation of the optical field for the propagation of partially coherent radiation with a specified spatial and temporal coherence function," *Journal of the Optical Society of America A*, vol. 23, pp. 1616–1625, July 2006.

[91] A. E. Siegman, G. Nemes, and J. Serna, "How to (maybe) measure laser beam quality," in *OSA Trends in Optics and Photonics*, vol. 17, pp. 184–199, Optical Society of America, Jan. 1998.

[92] F. Demaria, *Schicht- und Resonatordesign von Halbleiterscheiblasern*. PhD thesis, Universität Ulm, Germany, 2008.

[93] S. Bigo, O. Leclerc, and E. Desurvire, "All-optical fiber signal processing and regeneration for soliton communications," *IEEE Journal of Selected Topics in Quantum Electronics*, vol. 3, no. 5, pp. 1208–1223, 1997.

[94] C. J. Saraceno, O. H. Heckl, C. R. E. Baer, M. Golling, T. Südmeyer, K. Beil, C. Kränkel, K. Petermann, G. Huber, and U. Keller, "SESAMs for high-power femtosecond modelocking: power scaling of an Yb:$LuScO_3$ thin disk laser to 23 W and 235 fs," *Optics Express*, vol. 19, pp. 20288–20300, Oct. 2011.

[95] C. R. E. Baer, C. Kränkel, C. J. Saraceno, O. H. Heckl, M. Golling, R. Peters, K. Petermann, T. Südmeyer, G. Huber, and U. Keller, "Femtosecond thin-disk laser with 141 W of average power," *Optics Letters*, vol. 35, pp. 2302–2304, July 2010.

[96] J. Buckley, A. Chong, S. Zhou, W. Renninger, and F. W. Wise, "Stabilization of high-energy femtosecond ytterbium fiber lasers by use of a frequency filter," *Journal of the Optical Society of America B: Optical Physics*, vol. 24, pp. 1803–1806, Aug. 2007.

[97] M. Hoffmann, O. D. Sieber, V. J. Wittwer, I. L. Krestnikov, D. A. Livshits, Y. Barbarin, T. Südmeyer, and U. Keller, "Femtosecond high-power quantum dot vertical external cavity surface emitting laser," *Optics Express*, vol. 19, pp. 8108–8116, Apr. 2011.

[98] R. Paschotta, R. Häring, A. Garnache, S. Hoogland, A. Tropper, and U. Keller, "Soliton-like pulse-shaping mechanism in passively mode-locked surface-emitting semiconductor lasers," *Applied Physics B: Lasers and Optics*, vol. 75, no. 4, pp. 445–451, 2002.

[99] M. Hoffmann, O. D. Sieber, D. J. H. C. Maas, V. J. Wittwer, M. Golling, T. Südmeyer, and U. Keller, "Experimental verification of soliton-like pulse-shaping mechanisms in passively mode-locked VECSELs," *Optics Express*, vol. 18, pp. 10143–10153, May 2010.

[100] A. Garnache, S. Hoogland, A. C. Tropper, I. Sagnes, G. Saint-Girons, and J. S. Roberts, "Sub-500-fs soliton-like pulse in a passively mode-locked broadband surface-emitting laser with 100 mW average power," *Applied Physics Letters*, vol. 80, pp. 3892–3894, May 2002.